

Université du Québec
Institut National de la Recherche Scientifique
Centre Énergie, Matériaux et Télécommunications

**BIMETALLIC NANOPARTICLES SYNTHETIZED BY PULSED
LASER ABLATION IN LIQUIDS AS A CONTRAST AGENT FOR
DUAL IMAGING BY CT AND MRI**

By
Teresa Simão

Thesis to obtain the Doctor of Philosophy Degree in
Sciences of Energy and Materials

Jury Members

President of the jury and Internal examiner	Marc André Gauthier INRS-EMT
External examiner	Hai-Ling Margaret Cheng University of Toronto
External examiner	Teodor Veres IMI-CNRC
Supervisor	Daniel Guay INRS-EMT
Co-supervisor	Marc-André Fortin Laval University

ACKNOWLEDGEMENTS

The work here presented was part of a long journey, during which I learned so much, not only at the scientific level, but also personally. Definitely, to pursue this path and to reach its conclusion I had the support of many people to whom I am grateful.

I am very grateful to Prof. Daniel Guay for taking the challenge of guiding me in a field partially out of his main expertise, for trusting in my capabilities to succeed in this multidisciplinary work, as well as for always supporting me along the way. I'm also sincerely grateful to Prof. Marc-André Fortin for becoming my co-supervisor, and for his time as well as advices during so many fruitful discussions. To both my supervisors, thank you so much for persisting in the ideas and supporting me on taking the studies to the final application, especially at those moments when I could not believe it would be possible. *Merci beaucoup!*

Thank you to Prof. Barcikowski for receiving me in his group, sharing his knowledge and guiding me throughout the experiments in his laboratory.

I would like also to thank the research assistants and post-doctoral researchers that kindly shared their knowledge and experience, and who also helped me realizing several experiments: Andy Ng, Sébastien Garbarino, Gregory Goupil, Julie Guadet, Jean Lagueux, Pascale Chevallier, Marie-France Côté, Andrée-Anne Guay-Bégin, Dianne Djoumessi, Lilit Aboshyan Sorgho, Rodica Plesu, Jurij Jakobi, Christoph Rehbock, Christophe Chabanier, Antonio Benayas, Marta Quintanilla, Eva Hemmer, Denis Ferachou, Jianming Zhang, Jean-Phillipe Masse and Étienne Charette.

Thank you to my friends and colleagues, who supported me, shared their knowledge, provided valuable experimental advices, and whose presence turned many long days, working at the laboratories in different universities, much more enjoyable: Erwan, Esen, Bruno, Maria, Jules, Fanny, Meryem, Mathieu, Myriam, Ina, Galina, Marcus, Sven, Carmen, Réne, Sandra, Lisa, Mernoosh and Ivan.

I also would like to thank to Daniel Chevrier and Prof. Zhang for the XAFS analysis, as well as Dr. Mathieu Bugnet, Dr. Andreas Korinek and Dr. Bottom for the high resolution STEM and EELS analysis. Their valuable advices during manuscript preparation are also gratefully acknowledged.

I am also very grateful to the Technical Coordinator (Maria Helena Boeiro), the Director of the Radiology Department (currently Dr. Francisco Aleixo, and previously Dr. Jorge Pereira), the Clinical Director and the Chairman of the Board of Directors of the Algarve Hospital Center E.P.E. for granting me a leave to pursue my Ph.D. studies.

At last but not the least, I'm deeply grateful to my parents, José and Maria, to my sister, Rita, and to Erwan for their constant support, love and patience during the highs and lows of this journey.

ABSTRACT

Prostate and breast tumours have been the cancers with the highest incidence in Canada during the last decades. CT and MRI examinations are both crucial to establish the diagnosis, to plan the treatment and to follow up the response of these cancers to the therapy. However, multiple injections of intravenous contrast agents (CAs), made of different chemical compounds, are required during this period. Thus, a dual-modality CA with extended blood half-life would be beneficial to avoid multiple administrations of CA. Nanoparticles (NPs) are an advantageous template for the design of multimodal CAs. However, the synthesis of NPs for multimodal imaging can be a complex process, and requires often the utilization of several chemicals. Therefore, the utilization of simpler and aqueous-based procedures would be beneficial to produce purer NPs. Pulsed laser ablation in liquid (PLAL) offers these advantages, as composite nanostructures can be synthetized in a single-step using aqueous solutions. Hence, the objective of this thesis is to explore the potential of PLAL to produce Au-Gd and Au-Mn NPs, and to study their application as a dual imaging CA for CT and MRI.

Pulsed laser ablation of a Au-Gd target in aqueous solutions containing various concentrations of NaOH, or using different fluences, and in the presence of polyethylene glycol, resulted in the production of a Gd_2O_3 net connecting small Au NPs. Thus, the shape of this structure was not suitable for application as a CA. On the other hand, pulsed laser ablation of a Au-Mn target in a solution at pH 11 (adjusted with NaOH) resulted in the synthesis of $\text{Au}-\text{MnO}_x$ NPs, in which a small gold core (4.8 nm) was partially surrounded by a thin MnO_x layer (0.3 to 1.3 nm), as demonstrated by HAADF HR-STEM and XPS. This coating showed a local structure similar to that of Mn_2O_3 and MnO_2 references, as determined by XAFS analysis. Although the $\text{Au}-\text{MnO}_x$ NPs had an interesting structure and were stable in solution without the addition of any stabilizing ligands, the high oxidation state of the Mn layer precluded the application of this material as a CA for MRI. Therefore, another strategy, based on the functionalization of Au NPs produced by PLAL with Mn^{2+} -chelates, was pursued. In this study, pure Au NPs were first produced by PLAL in an alkaline solution, and sterically stabilized afterwards, using minimal excess of PEG. At last, DMSA-DTPA complexes were added to the Au NPs@PEG, and Mn^{2+} ions were chelated by DTPA to produce a dual-modality CA. The functionalization procedure was monitored by DLS and UV-visible spectroscopy to confirm colloidal stability of the compound throughout the procedure. The Au NPs@PEG- Mn^{2+} had a final hydrodynamic diameter of 36.5 nm and a polydispersity of 0.2. Further characterization of the NPs at diverse stages of functionalization by TEM, XPS, FTIR and ^1H NMR evidenced the pristine Au surfaces and the progressive addition of different molecules. Finally, the Au NPs@PEG- Mn^{2+} were used to enhance the image contrast by both CT and MRI *in vitro* and *in vivo*, using a chicken embryo tumour model. In addition, intravenous administration of Au NPs@PEG- Mn^{2+} in mouse models showed blood retention of the CA for at least 90 minutes, which was in agreement with the formation of a stealth coating around the PLAL-synthetized Au NPs.

Hence, during this work, the potential of using PLAL to produce pure Au NPs in water, which can be beneficially used as CAs for CT, was evidenced. Regarding the production of a CT/MRI CA, we demonstrated that the easiest strategy to control the oxidation state of Mn, which is a determinant parameter to enhance MR image contrast, is to functionalize the Au NPs' surface with Mn^{2+} -chelates, instead of incorporating this element in the target to use for PLAL.

RÉSUMÉ

Les tumeurs de la prostate et du sein ont l'incidence la plus élevée parmi les cancers au Canada. Dans les deux cas, les examens par TDM et IRM sont essentiels pour établir le diagnostic, pour planifier le traitement et pour le suivi de la réponse de ces cancers à la thérapie. Cependant, plusieurs d'injections d'agents de contraste (AC) intraveineux, constitués d'éléments distincts, sont nécessaires au cours de ces examens. Par conséquent, un AC pour l'imagerie bimodale serait avantageux pour diminuer la fréquence d'injection des différents ACs. Les nanoparticules (NPs) sont des matériaux prometteurs pour la conception de ces AC multimodaux. Toutefois, la synthèse de NPs pour l'imagerie multimodale peut être un processus complexe et implique l'utilisation de nombreux produits chimiques difficiles à éliminer. Par conséquent, l'emploi de procédés plus simples et à base de solutions aqueuses a un potentiel pour augmenter la pureté des NPs. L'ablation laser en milieu liquide offre ces avantages, car elle permet la production de NPs bimétalliques en une seule étape en utilisant des solutions aqueuses. Par conséquent, cette thèse est dévouée à explorer le potentiel de l'ablation laser en milieu liquide pour produire des NPs d'Au-Gd et d'Au-Mn ainsi qu'à étudier le potentiel de ces matériaux pour des applications comme AC pour la TDM et l'IRM.

L'ablation laser d'une cible d'Au-Gd dans des solutions aqueuses contenant des concentrations variées d'hydroxyde de sodium, avec différentes fluences, ou en présence de polyéthylène glycol, a produit un réseau de Gd_2O_3 contenant des petites NPs d'or. Toutefois, la forme de cette structure n'est pas adaptée pour un AC pour l'imagerie *in vivo*. Par contre, l'ablation d'une cible d'Au-Mn dans une solution contenant de d'hydroxyde de sodium ($\text{pH}=11$), a permis la synthèse de NPs d' $\text{Au}-\text{MnO}_x$, dans lesquelles de petites NPs d'or (4,8 nm) ont été partiellement entourées par une couche mince d'oxyde de Mn (0,3 à 1,3 nm), tel que démontré par HAADF HR-STEM et XPS. Ce revêtement a démontré une similitude chimique avec les oxydes de référence Mn_2O_3 et MnO_2 , tel que déterminé par XAFS. Bien que les NPs d' $\text{Au}-\text{MnO}_x$ ont une structure intéressante et ont été stables en solution sans l'ajout de ligands de stabilisation, l'état d'oxydation de la couche de manganèse est trop élevé pour permettre l'application de ce matériau comme AC pour l'IRM. Par conséquent, une autre stratégie basée sur la fonctionnalisation des NPs d'or produites par ablation laser dans l'eau avec des chélates de manganèse a été poursuivie. Dans cette étude, les NPs d'or ont été produites par ablation laser dans une solution alcaline, et stériquement stabilisées en utilisant un petit excès de PEG. Enfin, les complexes DMSA-DTPA ont été ajoutés aux NPs d'or recouvertes avec du PEG, et ensuite les ions de manganèse ont été ajoutés à ces NPs pour produire un AC bimodal. La procédure de fonctionnalisation a été suivie par spectroscopie d'absorption par UV-visible et DLS pour confirmer la stabilité colloïdale des NPs tout au long de toute la procédure. Les Au@PEG-Mn²⁺ NPs ont un diamètre hydrodynamique final de 36,5 nm et une dispersion de taille de 0,2. Une caractérisation plus poussée des Au@PEG-Mn²⁺ NPs et des NPs d'or par TEM, XPS, FTIR et ¹H RMN a mis en évidence la pureté des surfaces des NPs d'or et l'addition progressive des différentes molécules. Enfin, les Au NPs@PEG-Mn²⁺ ont été utilisées pour améliorer le contraste de l'image à la fois par TDM et par IRM, *in vitro* et *in vivo*, en utilisant un modèle de tumeur créé dans des embryons de poulet. En outre, l'injection intraveineuse des Au NPs@PEG-Mn²⁺ dans des souris a montré la rétention des NPs dans la circulation sanguine pendant 90 minutes, en accord avec la formation d'un revêtement polymérique autour des NPs d'or.

Pour conclure, au cours de ce travail, nous avons démontré le potentiel de l'ablation laser en milieu liquide pour produire des NPs d'or sans surfactants, qui peuvent être avantageusement utilisées comme ACs pour la TDM. Concernant la production d'un AC bimodale, nous avons conclu que la stratégie la plus pratique pour contrôler l'oxydation du manganèse est de fonctionnaliser la surface des NPs d'or avec des chélates de manganèse.

SOMMAIRE RÉCAPITULATIF

INTRODUCTION

Le cancer est la principale cause de décès au Canada. Les cancers de la prostate et du sein ont l'incidence la plus élevée pour les hommes et les femmes, respectivement.^{1, 2} Pour cette raison, et aussi à cause de nombreux diagnostics trop tardifs, le cancer du sein représente la deuxième cause de décès par cancer chez les femmes, alors que le cancer de la prostate est la troisième cause pour les hommes. Malheureusement, les prévisions indiquent que le nombre de ces cancers continuera d'augmenter au Canada à cause de la population croissante et vieillissante.² Par conséquent, la prévention, le diagnostic et des traitements plus efficaces seront nécessaires pour réduire l'impact de ces maladies sur la population canadienne et le système de santé.

Les techniques d'imagerie médicale ont un rôle important pour le dépistage, le diagnostic, la stadiification, la thérapie, le suivi du traitement et pour détecter des signes éventuels de récurrence du cancer.³⁻⁵ Pour ce faire, l'imagerie par résonance magnétique (IRM) et la tomodensitométrie (TDM) sont fréquemment utilisées.⁶⁻¹¹

Les protocoles d'imagerie, soit pour l'IRM ou pour le TDM, nécessitent l'administration d'agents de contraste intraveineux (AC) afin d'améliorer la localisation de la tumeur, d'acquérir des informations cinétiques nécessaires pour la caractérisation des lésions et pour évaluer la réponse au traitement.^{4, 6, 9} Les études dynamiques après injection de produit de contraste en IRM utilisent des chélates de gadolinium (Gd), alors que les études en TDM exigent un agent de contraste à base d'iode. Après l'injection intraveineuse, les deux types d'AC sont distribués dans tous les tissus vascularisés et diffusés aux espaces interstitiels. Ces procédés fournissent une bonne sensibilité et spécificité, notamment pour la détection du cancer de la prostate, mais malheureusement le rehaussement du contraste par la tumeur est non spécifique.^{7, 9} Un autre désavantage a trait au fait que les AC sont rapidement éliminés de la tumeur et de la circulation sanguine par les reins, ce qui limite le temps pour acquérir des images avec une bonne valeur diagnostique. Ceci est une limitation importante pour la thérapie guidée par imagerie, dans lesquelles plusieurs d'injections d'AC sont nécessaires.^{3-4, 12-13}

Compte tenu de la fréquence à laquelle l'IRM et les études en TDM doivent être effectuées pour le diagnostic et pendant le traitement des cancers de la prostate et du sein, le

développement d'un AC multimodal avec une demi-vie dans le sang plus longue aurait le potentiel de réduire la fréquence des injections d'AC et de fournir plus de temps pour l'acquisition d'images.

En conséquence, différentes stratégies ont été employées pour produire ces types d'AC.¹⁴⁻²⁴ À cet égard, les nanoparticules (NPs) montrent un grand potentiel parce que (1) une seule particule peut transporter des centaines, voire même des milliers de molécules de signalisation, qui fournissent donc un signal localisé et plus intense lors de la détection par l'instrument;²⁵ (2) les NPs peuvent être modifiées avec des biomarqueurs spécifiques à la maladie, ce qui augmente la spécificité de l'imagerie;²⁶ (3) la composition et la surface des NPs peuvent être ajustées pour accueillir différents types d'AC et de médicaments;²⁷ (4) la taille, la forme et le revêtement des NPs peuvent être facilement modifiés, ce qui permet d'ajuster la demi-vie et la biodistribution des particules;²⁸ et (5) les NPs ont des dimensions similaires à celles des molécules biologiques, donc elles peuvent interagir avec les récepteurs cellulaires et conséquemment avoir des propriétés pharmacocinétiques différentes des AC moléculaires.²⁹⁻³⁰

Par contre, les NPs multifonctionnelles, qui sont nécessaires pour l'imagerie multimodale, sont complexes à synthétiser et ce processus peut impliquer de nombreux réactifs nécessitant des procédures de purification complexes.^{18, 20-21} Malgré ces longues étapes de purification, la surface des NPs peut rester contaminée avec plusieurs des produits chimiques utilisés lors de la synthèse (ex. citrate de sodium).³¹ En fait, pour que les NPs reçoivent l'approbation pour une utilisation en milieu clinique, leur synthèse doit être simple et surtout leur surface doit être aussi propre que possible.³² Actuellement, de nouvelles techniques permettant la synthèse en une seule étape de NPs multifonctionnels, dont la surface est exempte de composés chimiques, sont nécessaires pour atteindre cet objectif.

Un exemple d'un tel procédé est l'ablation laser en milieu liquide. Cette technique permet la synthèse, en une seule étape, de NPs mono- et bimétalliques stabilisées électrostatiquement dans l'eau sans addition d'agents réducteurs ou de stabilisation.³³⁻³⁶ Par conséquent, la surface des NPs est très pure et peut être facilement modifiée avec des molécules biocompatibles. Le fait que la surface de ces NPs est exempte de contaminants ou d'agents de stabilisation permet également, en comparaison avec des NPs synthétisées par voie chimique, d'obtenir un meilleur recouvrement de leur surface avec les molécules biocompatibles désirées.³⁷ Globalement, les NPs synthétisés par l'ablation laser en milieu liquide pourraient (1) améliorer la biocompatibilité des nanomatériaux pour des applications biomédicales, (2) réduire l'excès de ligands nécessaires pour le greffage de la surface, et (3) permettent de diminuer le nombre d'étapes de purification et d'échange de ligands.

Par conséquent, l'objectif principal de cette thèse est d'utiliser l'ablation laser en milieu liquide pour produire des NPs constituées d'or (nécessaire pour améliorer le contraste en TDM) et d'un matériau paramagnétique, tel que le manganèse (Mn^{2+}) ou le gadolinium (Gd^{3+}) (requis pour l'augmentation du contraste en IRM), afin d'étudier le potentiel de ces nouveaux matériaux pour l'imagerie multimodale par TDM et IRM. Plus spécifiquement, les objectifs seront (1) de synthétiser et de caractériser des NPs d'or-gadolinium par ablation laser dans l'eau, et aussi (2) de synthétiser les NPs d'or-manganèse par la même voie ainsi que de faire une caractérisation physicochimique détaillée de ces systèmes. Pour ce dernier système, nous allons aussi démontrer la possibilité de synthétiser des NPs d'or par ablation laser dans l'eau et de modifier la surface de ces particules avec des chélates de manganèse. Ces particules seront désignées comme Au NPs@PEG-Mn²⁺, puis caractérisées et testées comme AC pour l'imagerie par TDM et IRM.

MÉTHODES EXPÉRIMENTALES

Préparation des cibles pour ablation laser

Les cibles d'or-gadolinium (Au-Gd) et d'or-manganèse (Au-Mn) ont été préparées en mélangeant mécaniquement des poudres métalliques d'or et de gadolinium ou d'or et de manganèse, puis en les comprimant avec une presse hydraulique. Pour le système Au-Gd, les poudres ont été mélangées dans un rapport atomique de 50% Au / 50% de Gd, tandis que pour le système Au-Mn un mélange de 64% Au avec 36% Mn a été utilisé. Le ratio des éléments dans la cible a été basé sur les alliages riches en or qui pouvaient être formés selon le diagramme de phase binaire de chaque mélange (ex. Au-Gd et Au-Mn).³⁸ Les alliages riches en Au ont été préférés pour l'application de ces matériaux comme agent de contraste pour TDM et IRM, car en TDM il est nécessaire d'utiliser des concentrations plus élevées d'or (ex. l'ordre de dizaines de mM) par rapport aux concentrations de Gd^{3+} ou Mn^{2+} (ex. de l'ordre de quelques mM) pour obtenir une augmentation de contraste significative.

Synthèse de nanoparticules par ablation en milieu liquide avec un laser nanoseconde ayant une longueur d'onde de 248 nm

Pour la synthèse en une seule étape de nanoparticules d'Au-Gd, d'Au-Mn et Au pur, les cibles métalliques respectives (ex. Au₅₀Gd₅₀, Au₆₄Mn₃₆ ou Au₁₀₀) ont été fixées sur le fond d'un bécher et le laser a été focalisé sur la surface de la cible. Par la suite, le récipient a été rempli avec 4 mL d'eau dé-ionisée avec des concentrations spécifiques d'hydroxyde de sodium (NaOH), d'acide chlorhydrique (HCl) ou de polyéthylène glycol (PEG) (3 kDa) en fonction du but de l'expérience. La cible métallique a été soumise à une ablation en utilisant un laser à fluorure de krypton (KrF) (longueur d'onde : 248 nm, largeur de pulse: 20 ns). Avant la caractérisation physicochimique, les colloïdes ont été centrifugés pour éliminer les possibles fragments de la cible et les particules plus larges.

Synthèse de nanoparticules par ablation en milieu liquide avec un laser nanoseconde ayant une longueur d'onde de 1064 nm

Afin de synthétiser les NPs d'or requises pour la production de Au NPs@PEG-Mn²⁺, une plaque d'or a été fixée à l'intérieur d'une chambre d'ablation avec une capacité de 30 mL. Dans cette configuration, le faisceau laser (Nd: YAG laser nanoseconde, longueur d'onde: 1064 nm, largeur de pulse: 8 ns) a été dirigé horizontalement à la surface de la cible et a été balayé sur la surface de la cible lors de l'ablation. La synthèse a été effectuée en utilisant une solution aqueuse contenant 3,3 mM de NaOH (pH 11). Après la synthèse, les colloïdes d'or ont été centrifugés pour éliminer la plupart des fragments de la cible et les plus grandes NPs qui sont inévitablement formées lors de l'ablation laser en milieu liquide.³³

Fonctionnalisation des nanoparticules d'or synthétisées avec le laser nanoseconde de 1064 nm

Ensuite, les NPs d'or ont été fonctionnalisées avec du PEG hétéro-fonctionnel (NH₂-PEG-SH, 5 KDa) pour leur conférer une stabilisation stérique. Pour cela, les molécules de PEG ont été dissoutes dans de l'eau dé-ionisée et ajoutées à la solution alcaline contenant les NPs d'or. Le rapport des molécules de PEG et des NPs d'or est de 1000: 1. L'incubation du PEG avec les NPs a été effectuée durant la nuit afin de maximiser le recouvrement et la géométrie d'adsorption des molécules de PEG à la surface des NPs.³⁹ Le colloïde résultant a été dialysé pour éliminer l'excès de PEG et de NaOH. Par la suite, les NPs d'or couvertes avec du PEG ont été mélangées avec

du DMSA conjugué avec du DTPA. Le DTPA est un agent chélateur utilisé couramment dans les AC dans la pratique clinique, et il forme un complexe relativement stable avec Mn²⁺.⁴⁰ Le Mn²⁺ a été ajouté suite une dialyse pour éliminer l'excès de DMSA-DTPA.

Caractérisation physicochimique des nanoparticules

Tous les colloïdes (ex. Au-Gd, Au-Mn, Au et Au NPs@PEG-Mn²⁺) ont été analysés par la spectroscopie d'absorption dans l'UV-visible, afin d'observer la position et l'intensité de la bande de résonance du plasmon de surface (SPR). Ce plasmon se produit lorsque la longueur d'onde d'illumination correspond à la fréquence naturelle d'oscillation des électrons de surface.⁴¹ Cette fréquence de résonance dépend de la taille des NPs, de l'indice de réfraction du milieu entourant les NPs et de la composition des NPs. Par conséquent, cette méthode a été utilisée pour estimer la formation de structures composites contenant l'or, pour suivre les modifications de la surface des NPs d'or et pour d'estimer la taille des NPs.⁴²⁻⁴³ Enfin, cette méthode a été utilisée pour estimer la concentration des NPs d'or (basée sur l'absorption à 380 nm, qui est dû à la transition interbande des atomes d'or)⁴⁴ et pour évaluer la dispersion ou la présence d'agrégats et d'agglomérats. Cette évaluation est fondée sur le ratio entre l'absorption à 380 nm et celle à 800 nm (dénommé l'indice de dispersion des particules, IPP),⁴⁵⁻⁴⁶ car l'augmentation de l'absorption de la lumière à 800 nm suggère la présence de particules volumineuses ou des agrégats qui peuvent provoquer la diffusion de la lumière.⁴⁷

Les NPs d'Au-Gd, d'Au-Mn et d'Au ainsi que d'Au NPs@PEG-Mn²⁺ ont été également observées par MET, et dans certains cas leur composition a été étudiée en utilisant l'EDS.⁴⁸ De plus, les NPs d'Au-Mn ont été aussi observées en haute résolution avec un détecteur champ sombre annulaire grand angle (HAADF) permettant d'obtenir des images en contraste Z.⁴⁹ Ces échantillons ont été également analysés par spectrométrie de perte d'énergie des électrons (EELS), une méthode d'analyse qui fournit une information identique à celle recueillie par EDS, mais à partir de l'énergie perdue par les électrons transmis.⁴⁸

Les techniques suivantes ont également été employées pour la caractérisation des nanoparticules préparées dans cette thèse:

- la diffraction des rayons X (XRD) a été effectuée pour caractériser la structure cristalline des NPs et pour le calcul de la taille des cristallites des échantillons produits à l'aide du laser nanoseconde de 248 nm;⁵⁰
- la spectroscopie des photoélectrons (XPS) a été utilisée pour étudier la composition chimique de la surface des NPs d'Au-Mn et pour suivre les modifications moléculaires effectuées au cours de la synthèse de Au NPs@PEG-Mn²⁺;⁵¹
- la spectroscopie d'absorption X (XAS) a été aussi réalisée pour déterminer l'environnement local et l'oxydation du manganèse dans les NPs d'Au-Mn;⁵²
- la spectroscopie infrarouge à transformée de Fourier et à réflexion totale atténuée (ATR-FTIR) a été utilisé pour étudier la présence de liaisons spécifiques, caractéristiques des différentes molécules organiques utilisées pour produire des Au NPs@PEG-Mn²⁺;⁵³
- la diffusion dynamique de la lumière (DLS) a été utilisée pour mesurer les diamètres hydrodynamiques (HD) des NPs. Cette méthode est particulièrement utile pour confirmer la stabilité colloïdale des Au NPs@PEG-Mn²⁺ et pour étudier la stabilité de ces particules dans différents milieux pendant plusieurs jours;⁵⁴
- le potentiel zéta a été mesuré pour évaluer la charge totale de la surface des Au NPs@PEG-Mn²⁺, ainsi que pour confirmer la modification de la surface au cours de la fonctionnalisation.⁵⁴

Pour évaluer la capacité des Au NPs@PEG-Mn²⁺ à diminuer les temps de relaxation (T_1 et T_2) des protons à proximité des AC (généralement les protons des molécules d'eau), la spectroscopie RMN du proton (¹H-RMN) a été utilisée. Après avoir mesuré les temps de relaxation pour différentes concentrations de Mn²⁺, les relaxivités (r_1 , r_2) ont été extraites à partir de la pente de la courbe de régression linéaire obtenue après la représentation graphique des taux de relaxation ($1/T_1$, $1/T_2$) en fonction de la concentration en manganèse dans chaque échantillon de Au NPs@PEG-Mn²⁺.

Finalement, l'analyse élémentaire des NPs d'Au-Mn a été réalisée par activation neutronique (NAA), tandis que les Au NPs@PEG-Mn²⁺ et Au NPs@PEG ont été analysées par spectroscopie de masse à plasma à couplage inductif (ICP-MS) ou spectroscopie d'émission atomique à plasma micro-onde (MP-AES).

Études de cytotoxicité et études d'imagerie *in vitro* et *in vivo* avec les Au NPs@PEG-Mn²⁺

Pour évaluer la viabilité des cellules après exposition à des concentrations variées de Au NPs@PEG-Mn²⁺ ou Au NPs@PEG, le test à la résazurine a été effectué. En utilisant cette méthode, nous avons évalué la cytotoxicité en fonction de la réduction de la résazurine (un colorant non fluorescent) en un colorant fluorescent rose, la résorufine. Ainsi, une faible production de résorufine, en comparaison avec des cellules de contrôle, indique que le métabolisme cellulaire et la prolifération sont diminués.⁵⁵

L'imagerie par TDM a été effectuée *in vitro* pour caractériser l'amélioration du contraste d'image avec plusieurs concentrations des Au NPs@PEG-Mn²⁺, et *in vivo* avec un modèle du cancer de la prostate dans la membrane chorioallantoïque (CAM) du poulet. L'imagerie par TDM a aussi été utilisée pour effectuer des études dynamiques après injection des Au NPs@PEG-Mn²⁺ en utilisant des modèles animaux.

Finalement, des études d'IRM ont également été réalisées pour caractériser l'amélioration du contraste fourni par Au NPs@PEG-Mn²⁺ *in vitro* et *in vivo*.

RÉSULTATS ET DISCUSSION

Nanostructures d'or-gadolinium synthétisées par ablation laser en milieu liquide

Compte tenu des avantages du Gd³⁺ comme AC pour l'IRM, la première étape de ce travail était d'essayer la synthèse de NPs d'Au-Gd par ablation laser en milieu liquide. L'ablation de la cible Au₅₀Gd₅₀ a été réalisée à plusieurs pH (7-11) et avec différentes fluences. L'effet de la fluence sur l'ablation de la cible a été étudié à pH 11, car cette concentration de NaOH permet le taux d'ablation le plus élevé pour une fluence fixe.

Les colloïdes obtenus après l'ablation de la cible présentaient un spectre d'absorption similaire pour l'ensemble des pH et des fluences testés. Cependant, les spectres étaient différents du spectre caractéristique des NPs d'or, ce qui suggère la formation d'une structure composite.

L'analyse de la structure cristalline des colloïdes Au-Gd synthétisés à différents pH et fluences a montré que tous les échantillons contenaient de l'or et du Gd₂O₃, car la structure cristalline cubique caractéristique de Au (paramètre de maille de 4,078 Å) et de la phase monoclinique de Gd₂O₃ (paramètre de maille : a = 14,095 nm, b = 3,576 nm et c = 8,769 nm) ont été identifiées. Il n'y avait pas de changement dans le paramètre de maille des deux éléments, ce qui suggère qu'un alliage d'Au-Gd n'a pas été formé.

La stabilité des colloïdes d'Au-Gd₂O₃ était aussi très limitée. En effet tous les échantillons ont précipité en l'espace d'environ une heure après la synthèse. Par conséquent, la cible métallique Au₅₀Gd₅₀ a également été soumise à une ablation dans une solution aqueuse contenant 0,1 g L⁻¹ de PEG, puisque ce polymère est utilisé souvent pour améliorer la stabilité colloïdale des NPs. Ces colloïdes présentent un spectre UV-vis semblable à celles préparées sans PEG et sont restés en suspension jusqu'à un jour après la synthèse.

Un échantillon a été observé par MET pour étudier la structure du composite Au-Gd₂O₃ formé par ablation laser. La composition élémentaire de cet échantillon a aussi été confirmée par EDS. Sur la figure 1 on a observé que les colloïdes d'Au-Gd₂O₃ sont composés de très petites NPs d'or reliées par un réseau de Gd₂O₃.

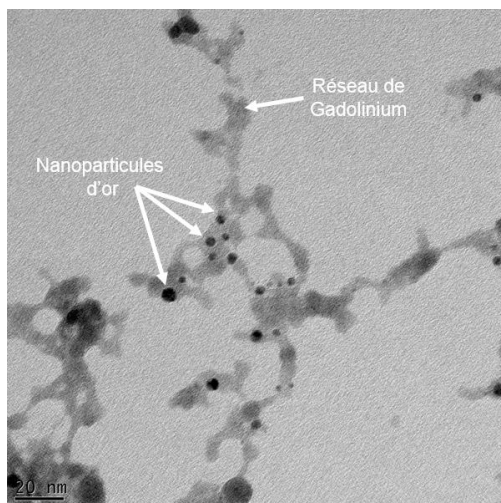


Figure 1. Image de MET des nano-composites d'Au-Gd₂O₃ produits par ablation laser d'une cible de Au-Gd dans une solution de 0,1 g L⁻¹ de PEG (3 kDa).

Tarasenko et ses collègues ont produit des NPs de Gd₂O₃ bien dispersées après l'ablation d'une plaque métallique de Gd dans l'eau distillée avec un laser ayant une longueur d'onde de 1064 nm.⁵⁶ Par conséquent, le réseau de Gd₂O₃ formé avec la méthode décrite ci-dessus est probablement lié à une forte autoabsorption d'énergie provenant du laser UV par les NPs de Gd₂O₃ formées ou éjectées hors de la cible pendant l'ablation laser.⁵⁷ La structure du colloïde d'Au-Gd₂O₃ obtenu ne convient pas pour une application *in vivo*. Par conséquent, une autre synthèse a été étudiée en utilisant une cible métallique d'Au-Mn.

Nanoparticules d'Au-Mn synthétisé par ablation laser en milieu liquide

L'ablation de la cible $\text{Au}_{64}\text{Mn}_{36}$ a été réalisée dans des solutions aqueuses à divers pH (7-11). L'analyse des spectres UV-visible de ces échantillons a démontré que le spectre est légèrement modifié avec des concentrations croissantes de NaOH. Ainsi, contrairement à ce qui a été observé dans le système Au-Gd₂O₃, il a été conclu que le pH avait une influence sur la structure formée. En outre, nous avons aussi constaté que ce paramètre affecte la stabilité des colloïdes. En effet, les colloïdes obtenus à un pH de 7 et 8 ont précipité quelques heures après l'ablation, tandis que les particules obtenues à un pH de 9 et 10 ont été stables pendant plusieurs jours. Les échantillons produits en utilisant un pH 11, quant à eux, peuvent être stables pendant des mois sans ajout d'agent stabilisant. Étant donné que la stabilité colloïdale est une exigence pour la production d'AC à base des NPs, le colloïde produit à pH 11 a été choisi pour une caractérisation plus détaillée.

En comparant le spectre des NPs d'Au-Mn synthétisées à pH 11 avec celui des NPs d'or préparées dans les mêmes conditions, un décalage vers le rouge et une forte atténuation de la bande de SPR ont été observés. La fréquence de résonance, nécessaire pour créer l'effet de SPR, peut varier avec la taille, la forme, la composition, l'état d'agrégation des NPs et avec la constante diélectrique du milieu autour des NPs.⁵⁸⁻⁵⁹ Cependant, l'atténuation de la bande SPR est généralement une conséquence de la formation d'un alliage, ou pourrait être causée par le greffage de molécules qui acceptent des électrons à la surface des NPs d'or.⁶⁰⁻⁶¹ Par conséquent, il a été conclu qu'un noyau-enveloppe ou des structures d'alliage ont pu être formés.

Afin de déterminer la structure des NPs d'Au-Mn, des mesures de diffraction des rayons X et une cartographie EELS ont été réalisées. Le diffractogramme révèle une structure cristalline cubique avec un paramètre de maille de 4,0786 Å, attribué à l'or. Par conséquent, les NPs d'Au-Mn ne sont pas constituées d'un alliage. Ces résultats sont en accord avec la cartographie EELS, qui a révélé que les NPs avaient une structure noyau-enveloppe, dans laquelle des petites NPs d'or ont été partiellement ou complètement couvertes d'une couche très mince de manganèse.

Des observations à haute résolution ont également mis en évidence une structure noyau-enveloppe (figure 2). Les images acquises ont révélé la structure cristalline des petites NPs d'or (figure 2 (A)) et ont permis de différencier des zones amorphes (figure 2 (B), indiqué par des étoiles) et des régions cristallines (figure 2 (B), indiqué par des flèches) dans la couche mince (0,3 à 1,3 nm) de Mn. Des observations complémentaires effectuées par MET ont permis de mesurer la taille moyenne des NPs d'or, qui était d'environ 4,8 nm.

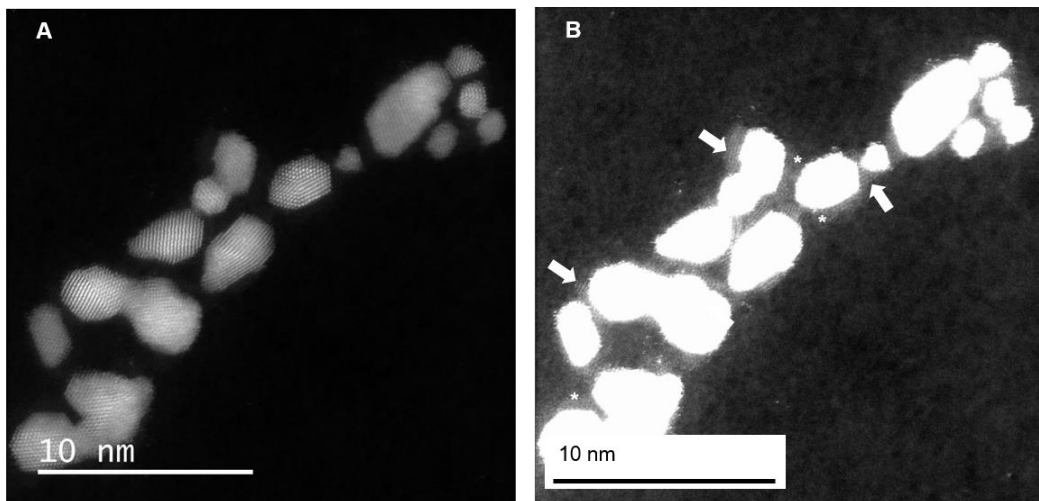


Figure 2. Micrographies en haute résolution et HAADF montrant les petites nanoparticules d'or (A) couvertes par une couche mince de manganèse (B). La couche contient des régions cristallines (indiquées par des flèches) et des régions amorphes (indiquées par des étoiles). Le contraste a été accentué en B afin de mettre en évidence la coquille de Mn.

L'analyse élémentaire réalisée par XPS, EDS et NAA a démontré que la fraction de manganèse (27 à 29%) contenue dans les NPs Au-Mn a été maintenue relativement constante, même après le rinçage de l'échantillon avec de l'eau dé-ionisée. Cela suggère que tout le manganèse était présent sous la forme solide et donc associé aux petites NPs d'or. Si le manganèse avait été dissous (ex. Mn^{2+} / Mn^{3+}), le lavage des NPs d'Au-Mn aurait causé une diminution significative de la teneur en manganèse dans l'échantillon.

Mn^{2+} est très intéressant comme AC pour l'IRM parce qu'il y a cinq électrons non appariés dans l'orbitale électronique 3d.⁶² Mais, quand l'état d'oxydation augmente, le nombre d'électrons non appariés diminue, ce qui réduit la capacité du manganèse à affecter les temps de relaxation des protons dans les molécules d'eau. Par conséquent, il est important de déterminer l'état d'oxydation de la couche de Mn pour évaluer le potentiel de ce matériau comme AC pour l'IRM.

L'analyse par XPS des NPs d'Au-Mn effectuée à cette fin révèle un pic centré à 529,7 eV, ce qui a confirmé la présence d'oxyde de manganèse sur la surface des NPs. Aussi, un autre pic centré à 531,7 eV suggère la présence de carbonate et des espèces d'hydroxydes.

De façon complémentaire, l'échantillon a été analysé par XAS pour confirmer l'état d'oxydation du manganèse. Les données d'EXAFS ont révélé que les distances de liaison Mn-O et Mn-Mn étaient 1,90 Å et 2,92 Å, respectivement. La comparaison de ces valeurs avec celles obtenues avec des structures référencées d'oxyde de manganèse (ex. MnO , Mn_2O_3 , MnO_2)

suggère que cette couche présente une structure qui ressemble à celle du MnO₂. L'évaluation qualitative des données obtenues par XANES sur les NPs d'Au-Mn et des références d'oxydes de Mn a démontré une similitude chimique avec les oxydes de référence Mn₂O₃ et MnO₂, en particulier en ce qui concerne l'énergie du bord d'absorption et les caractéristiques de la structure quasi-bord.

En accord avec l'oxydation élevée de la couche de Mn, les analyses préliminaires de relaxométrie par ¹H NMR de les NPs d'Au-Mn ont démontré que ces NPs n'ont pas affecté de façon significative les temps de relaxation des molécules d'eau, ce qui suggère que l'état d'oxydation du manganèse est élevé. Par conséquent, une autre stratégie, basée sur la fonctionnalisation des NPs d'or avec chélates de Mn²⁺, a été utilisée pour produire un AC pour l'imagerie multimodale basée sur des NPs synthétisées par ablation laser en milieu liquide.

Fonctionnalisation des nanoparticules d'or synthétisées par ablation laser en milieu liquide avec des chélates de Mn²⁺

Paramètres d'ablation laser pour synthèse de particules d'or ultra-petites

La première étape de cette approche a été de déterminer les paramètres d'ablation laser qui permettent de synthétiser des NPs d'or avec la plus petite taille, la plus basse dispersion de taille et la plus haute stabilité. La petite taille est nécessaire pour faciliter l'élimination des NPs, spécialement pour la voie rénale, et la faible dispersion est importante pour assurer que toutes les particules suivent la même pharmacocinétique.³⁰ La haute stabilité est requise pour éviter la formation d'agglomérats/agrégats avant la stabilisation stérique. En effet, la teneur ionique de la solution d'ablation est un paramètre dans la synthèse par ablation laser en milieu liquide qui peut influencer de manière significative les propriétés des NPs.⁴⁵⁻⁴⁶ Par conséquent, nous avons étudié la concentration de OH⁻ et de Cl⁻ qui a fourni le meilleur compromis entre la taille, la dispersion de taille et la stabilité colloïdale, en effectuant l'ablation laser d'une cible d'or immergée dans des solutions aqueuses à plusieurs pH (4-12) (ajusté avec différentes concentrations de NaOH ou de HCl), avec le laser ns de 248 nm.

Les spectres UV-visible des différents échantillons ont été utilisés pour estimer indirectement la taille, la stabilité colloïdale ainsi que la dispersion de taille, à partir de la position de la bande SPR et du rapport entre l'absorption à 380 nm et 800 nm (IPP). La position de la bande SPR des NPs d'or produites à pH 11, a suggéré que ces NPs eurent le plus petit diamètre (figure 3 (A)). Les données du IPP indiquent quant à elles que cet échantillon n'a pas la plus

grande stabilité colloïdale ni la dispersion de taille la plus réduite, mais l'IPP obtenu est encore considéré comme très bon (figure 3 (B)). Cet échantillon a également été observé par MET, confirmant l'existence de NPs de petite taille (6,6 nm) (figure 3 (C)).

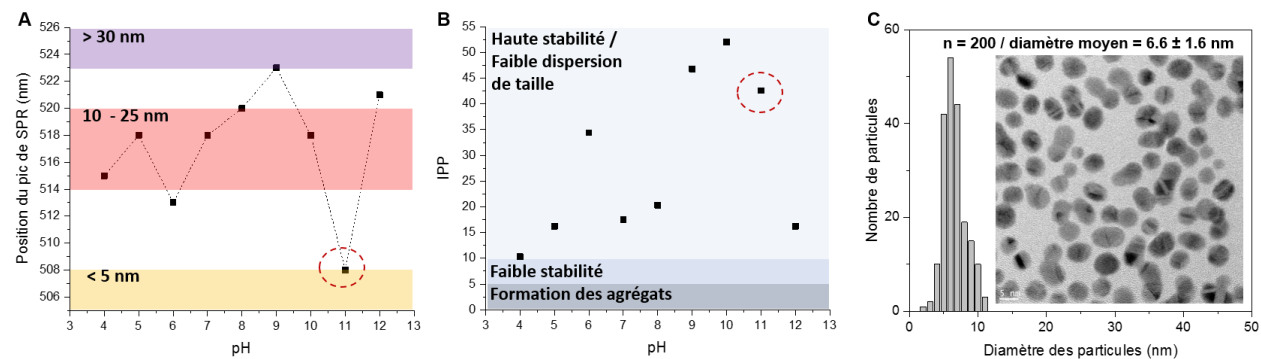


Figure 3. (A) Position du pic de SPR en fonction du pH de la solution utilisée lors de l'ablation laser de la cible d'or avec un laser nanoseconde ayant une longueur d'onde de 248 nm. (B) IPP en fonction du pH de la solution d'ablation. (C) Image de MET et la distribution de taille des NPs d'or obtenues en utilisant une solution de pH 11 (échelle: 5 nm).

Les NPs d'or synthétisées par PLAL sont stabilisées électrostatiquement par des espèces Au-OH et Au-O⁻ formés lors de la ablation.⁶³ Ainsi, le contrôle de la taille et la meilleure stabilité obtenus à pH 11 sont peut être liés à la déprotonation des espèces hydroxydes adsorbées sur la surface des NPs en milieu alcalin. Cela augmenterait la charge négative de la surface des NPs par la formation de groupes Au-O⁻. Par conséquent, la forte densité de charge à la surface des NPs augmente la répulsion entre elles, ce qui améliore la stabilité colloïdale et minimisera la coalescence.^{33, 64}

Un autre facteur à considérer pour l'application des NPs comme AC est le taux de production de matériel. Ceci est particulièrement important pour les NPs qui vont être utilisées comme AC en TDM, parce que des concentrations relativement élevées de NPs doivent être utilisées pour produire une amélioration significative de contraste.⁶⁵ Malgré les bons résultats obtenus en utilisant un laser UV, l'efficacité de la production avec ce laser est limitée en raison de l'autoabsorption de l'énergie du laser par les NPs qui absorbent fortement dans la région UV du spectre.⁵⁷ Étant donné que la concentration des NPs en solution augmente au cours de l'ablation, ce phénomène diminue progressivement l'énergie disponible pour l'ablation de la cible. Plusieurs auteurs ont démontré que la production de NPs d'or peut être améliorée en utilisant des lasers avec longueurs d'onde dans la région infrarouge, parce que l'absorption des NPs est plus

faible dans ce régime.^{33, 57} Par conséquent, afin de produire les quantités de NPs d'or nécessaires pour les études d'imagerie *in vitro* et *in vivo*, un laser nanoseconde avec une longueur d'onde de 1064 nm a été utilisé conjointement avec une chambre d'ablation optimisée pour la production de larges quantités de NPs. Ces NPs d'or ont été produites à pH 11 en raison des résultats prometteurs obtenus dans les expériences précédentes.

Les mesures de distribution de la taille effectuées par MET (figure 4 (A)) ont démontré que la taille (8 nm) était légèrement supérieure à celles obtenues avec le laser UV. Ce résultat était attendu, car l'absorption de la lumière a diminué, en minimisant de fait la fragmentation des NPs durant l'ablation.^{57, 66} Cependant, la stabilité colloïdale, la taille et la dispersion de la taille ont été encore appropriées pour les applications biomédicales de ces NPs.

Stabilisation stérique des nanoparticules d'or avec polyéthylène glycol et fonctionnalisation avec des chélates de manganèse

La première étape dans la production de Au NPs@PEG-Mn²⁺ a été de greffer les NPs d'or avec du PEG. Par la suite, ces NPs ont été fonctionnalisées avec des molécules de DMSA-DTPA et des ions de Mn²⁺. Afin de confirmer que la surface des NPs était couverte avec les différentes molécules, et ce sans affecter la stabilité colloïdale, la spectroscopie d'absorption UV-visible ainsi que des mesures DLS ont été réalisées pendant la procédure de fonctionnalisation.

Les spectres UV-visible ont démontré un léger décalage de la position de la bande de SPR (2-3 nm) à chaque étape de la procédure de fonctionnalisation, alors que simultanément l'absorption dans l'infrarouge demeure minimale. Les échantillons ont donc conservé leur stabilité colloïdale au cours du processus, et la surface a bien été modifiée à chaque étape de réaction. Les mesures de DLS ont montré des pics relativement étroits durant toute la procédure et l'absence d'agrégats de NPs, en accord avec les résultats obtenus par la spectroscopie d'absorption UV-visible. Ces mesures ont également démontré une augmentation significative du diamètre hydrodynamique après l'addition de PEG sur les NPs d'or (17,5 nm à 40,9 nm). Par contre, les modifications effectuées après (addition de DMSA-DTPA et de Mn²⁺) n'ont pas provoqué de changements significatifs du diamètre hydrodynamique (34,1 nm après DMSA-DTPA et 36,5 nm après la chélation de Mn²⁺). Par conséquent, la variation du diamètre hydrodynamique a été attribuée au greffage de molécules de PEG à la surface des NPs, à cause du poids moléculaire relativement élevé de ce polymère.

Caractérisation de taille et physico-chimique des nanoparticules fonctionnalisées

L'observation par MET des NPs fonctionnalisées (Au NPs@PEG-Mn²⁺) a montré une distribution de taille moyenne de 7,2 nm (figure 4 (B)), qui est semblable aux résultats obtenus sur les NPs d'or (figure 4 (A)). Par conséquent, les NPs d'or ne souffrent pas d'agrégation significative au cours du processus de fonctionnalisation. Enfin, il a été observé qu'après séchage pour l'observation par MET, les NPs sont régulièrement espacées (de 8,6 nm environ). Il s'agit là aussi d'une indication que les NPs d'or ont été modifiées avec une couche de PEG, parce que l'espacement entre les particules est similaire à la longueur estimée des molécules de PEG avec un poids moléculaire de 5 kDa.⁶⁷

Afin de confirmer la présence de PEG, du DMSA-DTPA et de Mn²⁺ sur la surface des NPs d'or, des analyses par XPS, ATR-FTIR, potentiel zéta et ¹H RMN ont été effectuées. La déconvolution du spectre de haute résolution C1s de XPS a clairement démontré les modifications produites sur la surface des NPs d'or. Dans le spectre des NP d'or, il a été possible d'observer la contamination de carbone atmosphérique, qui se caractérise par des liaisons C-C/H, et un faible pourcentage de groupes carboxyls et carbonyles.⁶⁸ La présence de hautes teneurs de carbone est une conséquence fréquente de l'exposition de l'échantillon à l'atmosphère ambiante pendant le séchage des NPs sur les substrats d'observation. Aussi, des groupes fonctionnels carbonates ont été observées, provenant probablement du carbonate de sodium, ce qui est cohérent avec l'utilisation de NaOH pendant la synthèse des NPs.⁶⁹ Après l'addition de PEG, les pics attribués au carbonate de sodium ont disparu et le signal de XPS le plus intense a été attribué à la présence de carbone dans une liaison C-O-C, caractéristique de la présence de PEG.⁶⁸ Par la suite, la fonctionnalisation avec le DTPA-DMSA conduit à une augmentation du pourcentage relatif des groupes carboxylés et éventuellement des groupes O=C-N, qui sont présents dans ces molécules. La forte présence de liaisons C-O-C a aussi été maintenue. La chélation du Mn²⁺ n'a pas modifié la composition moléculaire détectée à la surface des NPs d'or. Cependant, il y a eu un léger changement dans le pourcentage relatif des pics attribués à O-C=O / O=C-N et C-O-C, ce qui suggère qu'un excès de DTPA-DMSA a été retiré au cours des étapes de chélation et de dialyse subséquentes.

En accord avec les analyses par XPS, les mesures ATR-FTIR ont indiqué des résultats en accord avec les signatures observées en XPS. Le spectre des NPs d'or a révélé des modes de vibration en relation avec la présence de ligands contenant des groupes carbonyles (à 1668 et 1741 cm⁻¹), carboxylates (dans la zone entre 1338 et 1396 cm⁻¹ et à 1568 cm⁻¹) et méthylènes (à 2852 et 2924 cm⁻¹).⁷⁰ La présence de groupes de méthylène est probablement une

conséquence de traces de méthanol, puisque ce solvant a été utilisé pour nettoyer le cristal avant la déposition des NPs pour l'analyse. Après l'ajout de PEG à la surface des NPs d'or, les principaux modes de vibration observés dans le spectre de cet échantillon ont été attribués à la chaîne du squelette de PEG (ex. bande de C-O-C à 1113 cm^{-1}).⁷¹ Ce résultat a confirmé que la plupart des molécules de carbonate ont été retirées après le greffage du PEG. La présence des molécules de DMSA et de DTPA a été mise en évidence par l'apparition des bandes correspondant aux groupes carboxylés (1705 cm^{-1}) et carboxylates (1599 et 1406 cm^{-1}).⁷² Enfin, le seul changement observé après la chélation du Mn^{2+} fut un décalage du mode de vibration asymétrique du groupement carboxylate 1631 à 1599 cm^{-1} . Des études antérieures ont attribué ce changement à la coordination des ions métalliques par les groupes carboxylates.⁷³ Par conséquent, dans le présent ouvrage, ceci a suggéré la chélation de Mn^{2+} par DTPA.

La charge de la surface des NPs a également été utilisée pour suivre les changements de surface qui se sont produits à chaque étape de la procédure de fonctionnalisation. Les NPs d'or ont montré une forte charge négative (-28,5 mV) à pH 10, ce qui est en accord avec la stabilité colloïdale à long terme du produit. Au contraire, après greffage du PEG, la charge de la surface est devenue fortement positive (22,3 mV) dans de l'eau dé-ionisée. Ce changement a été attribué à la présence des amines dans les molécules de PEG, qui sont positivement chargées (i.e. protonées) dans l'eau. Ensuite, l'ajout de DMSA-DTPA a induit une diminution de la charge nette ($-3,9 \pm 1,8\text{ mV}$), en raison de la charge négative des groupes carboxylate. Cependant, la charge positive des ions Mn^{2+} a augmenté la charge de surface et conduit à un potentiel zéta final de +5,8 mV.

Caractérisation des propriétés de relaxivité, de stabilité colloïdale, et de cytotoxicité

Enfin, la présence de Mn^{2+} a été confirmée par ^1H RMN. De fait, les Au NPs@PEG- Mn^{2+} diminuent efficacement les temps de relaxation T_1 et T_2 de l'eau. Donc, ces complexes ont un r_1 de $4,8\text{ mM}^{-1}\text{ s}^{-1}$ et un rapport relaxométrique (r_2/r_1) de 3,6, qui est caractéristique des AC IRM positifs. La valeur de r_1 a aussi suggéré que Mn^{2+} a été incorporé dans la couche de PEG et chélatisé par le DTPA, puisque cette valeur est inférieure à celle des ions Mn^{2+} dissous, mais supérieure à celle de chélates de Mn^{2+} en solution.⁷⁴

Pour les études biologiques avec des NPs, il faut tester la stabilité des particules dans une solution saline et dans une autre solution riche en protéines. Donc, la stabilité colloïdale des

Au NPs@PEG-Mn²⁺ a été mesurée jusqu'à sept jours dans de l'eau dé-ionisée, dans une solution contenant 154 mM de NaCl et dans un milieu de culture cellulaire complet.

Ces études ont démontré que les NPs sont stables pendant la durée de l'expérience dans l'eau sans formation d'agglomérats. Les Au NPs@PEG-Mn²⁺ ont également démontré une excellente stabilité en solution saline, si bien qu'après sept jours, seule une quantité minimale (~ 1%) d'agglomérats a été détectée dans les mesures de DLS pondérées en intensité. La formation de ces agglomérats pourrait être liée à l'existence des NPs d'or qui ne sont pas fortement recouvertes de PEG. Ainsi, lorsque dispersées dans une solution fortement ionique, ces particules peuvent s'agglomérer, car la protection stérique n'est pas suffisamment dense pour surmonter l'attraction électrostatique créée par les forces de van der Walls.⁶⁴ Ces résultats ont néanmoins démontré que les Au NPs@PEG-Mn²⁺ peuvent être dispersées dans la solution saline nécessaire à l'injection et être conservées à température ambiante sur une période de trois jours sans formation d'agglomérats. En outre, la concentration minimale d'agglomérats formés lors d'un stockage de sept jours dans le milieu salin peut être facilement éliminée par centrifugation avant l'injection des NPs.

Les Au NPs@PEG-Mn²⁺ ont également été mises en suspension dans un milieu de culture cellulaire complet (avec sérum fétal bovin = protéines). Immédiatement après la dispersion des NPs dans le milieu de culture cellulaire, une distribution de taille bimodale dans les mesures de DLS pondérée en intensité a été observée. Le pic associé à la majorité des NPs dans l'échantillon montre un diamètre hydrodynamique légèrement plus élevé (35,9 nm) que celui observé dans l'eau (32,8 nm) ou dans la solution de NaCl (31,6 nm). L'autre pic, centré à ~ 700 nm, représente seulement 5% de l'intensité de la lumière diffusée. Cette distribution de taille bimodale demeure inchangée pendant trois jours. La petite fraction d'agglomérats détectés a pu être formée en raison de l'adsorption et/ou de réticulation des particules en présence d'une forte concentration de protéines, qui contiennent des domaines chargés ou hydrophobes qui peuvent interagir avec la surface des NPs.⁷⁵ La présence de ces agglomérats n'est pas idéale pour les applications *in vivo*, mais le diamètre hydrodynamique de ces agglomérats n'est pas suffisamment large pour provoquer une occlusion vasculaire.⁷⁶ Par conséquent, les Au NPs@PEG-Mn²⁺ peuvent encore être utilisé pour les injections intraveineuses.

Quand la stabilité colloïdale est assurée, il est aussi nécessaire d'évaluer l'effet des NPs sur la toxicité cellulaire. Dans ces études, des temps d'incubation longs, ainsi que des concentrations élevées des NPs ont été utilisés pour démontrer clairement le potentiel de toxicité pour les cellules du cancer de la prostate (PC3). Bien que la viabilité cellulaire n'a pas été affectée

de manière significative jusqu'à 48 h d'incubation avec une concentration de 0,77 mM d'or, des concentrations plus élevées de Au NPs@PEG-Mn²⁺ ont affecté de façon significative la viabilité des PC3 à partir de 48 h d'incubation. Afin d'étudier si la cause de la toxicité cellulaire est liée à la nanostructure ou aux chélates de Mn²⁺, une étude comparative en utilisant seulement des NPs d'or couvertes de PEG a été réalisée. De manière surprenante, cette étude a démontré que les cellules PC3 peuvent tolérer jusqu'à 7 mM pendant 72 h. Par conséquent, ces études ont conduit à la conclusion que les complexes DMSA-DTPA-Mn²⁺ semblent être la cause de la cytotoxicité lorsque les concentrations modérées et élevées de Au NPs@PEG-Mn²⁺ sont utilisées. Ainsi, la concentration des complexes de DMSA-DTPA-Mn²⁺ devra être diminuée dans les études futures. Par contre, le fait que le métabolisme des cellules cancéreuses PC3 n'a pas été affecté par des concentrations relativement élevées des NPs d'or couvert par PEG est un résultat prometteur, parce que la plupart des études sur le développement d'AC à base des NPs d'or pour TDM se sont limitées à des études de viabilité cellulaire utilisant concentrations plus basses d'or.⁷⁷⁻⁷⁸ Cependant, des essais complémentaires doivent être effectués pour assurer que ces concentrations n'affectent pas les voies de signalisation et l'expression des gènes dans les cellules.

Performance des Au@PEG-Mn²⁺ NPS en IRM et en TDM

Finalement, la possibilité d'amélioration du contraste en IRM et en TDM avec les Au NPs@ PEG-Mn²⁺ a été évaluée *in vitro* et *in vivo* par des injections intratumorales sur un modèle de cancer de la prostate. Les études *in vitro* démontrent que les Au NPs@PEG-Mn²⁺ produisent une amélioration du contraste en TDM et en IRM à différentes concentrations. Comme prévu, une concentration-type de Mn²⁺ (ex. 0,2 mM) a été nécessaire pour produire l'augmentation du contraste en IRM. D'autre part, la concentration en éléments métalliques (Au) nécessaire pour produire un contraste efficace en TDM, est proportionnellement plus élevée que pour l'IRM (ex. 44,3 mM).

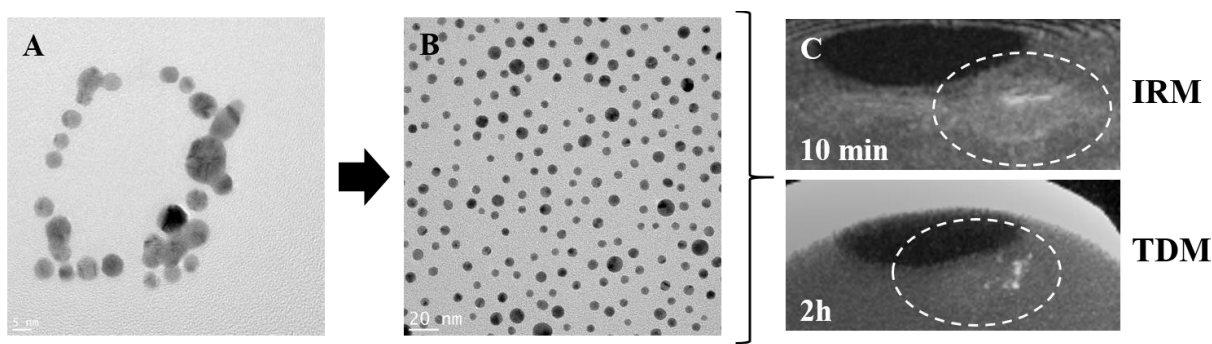


Figure 4. Image de MET des NPs d'or produites par ablation laser dans une solution contenant de 3,3 mM de NaOH, en utilisant un laser nanoseconde de 1064 nm (échelle: 5 nm) (A). En (B), image par MET des Au NPs@PEG-Mn²⁺ (échelle: 20 nm). En (c), images de RM et de TDM acquises après l'injection de Au NPs@PEG-Mn²⁺ dans un modèle CAM du cancer de la prostate (C).

L'injection des Au NPs@PEG-Mn²⁺ dans le modèle CAM développé avec cellules PC3 a généré une amélioration du contraste par IRM (à 10 min) et par TDM (à 2 heures) (figure 4 (C)). Le suivi des NPs injectées en utilisant les deux techniques, a démontré la diffusion des NPs dans la matrice de la tumeur, en particulier par TDM. En fait, le signal IRM décline significativement à 18 heures en raison de la diffusion de l'AC, qui a peut-être causé la réduction de la concentration de Mn²⁺ en dessous des limites de détection par IRM. Donc, cette expérience a démontré la possibilité d'effectuer de l'imagerie bimodale par TDM et IRM. Elle a également mis en évidence la stabilité des NPs en milieu biologique, car les NPs ont facilement diffusé à partir du site d'injection pendant plusieurs heures.

Enfin, les Au NPs@PEG-Mn²⁺ ont été injectées dans des souris ($n = 3$) pour évaluer leur performance en tant qu'AC vasculaire par TDM. À la concentration administrée, qui était semblable à celles rapportées pour les études vasculaires utilisant des NPs d'or, les Au NPs@PEG-Mn²⁺ ont fourni un rehaussement de contraste suffisant pour observer clairement le cœur et les vaisseaux sanguins majeurs jusqu'à 90 minutes après l'injection. En outre, d'autres organes (ex. les reins, le foie et la rate) ont montré une légère amélioration du contraste, ce qui était probablement lié à la riche vascularisation de ces tissus. L'amélioration générale du contraste est restée stable tout au long de l'étude à partir de 15 min après l'injection des NPs, même dans la rate et le foie (figure 5). Cette observation suggère une forte rétention des NPs dans le sang pendant une période appropriée pour les procédures angiographiques.

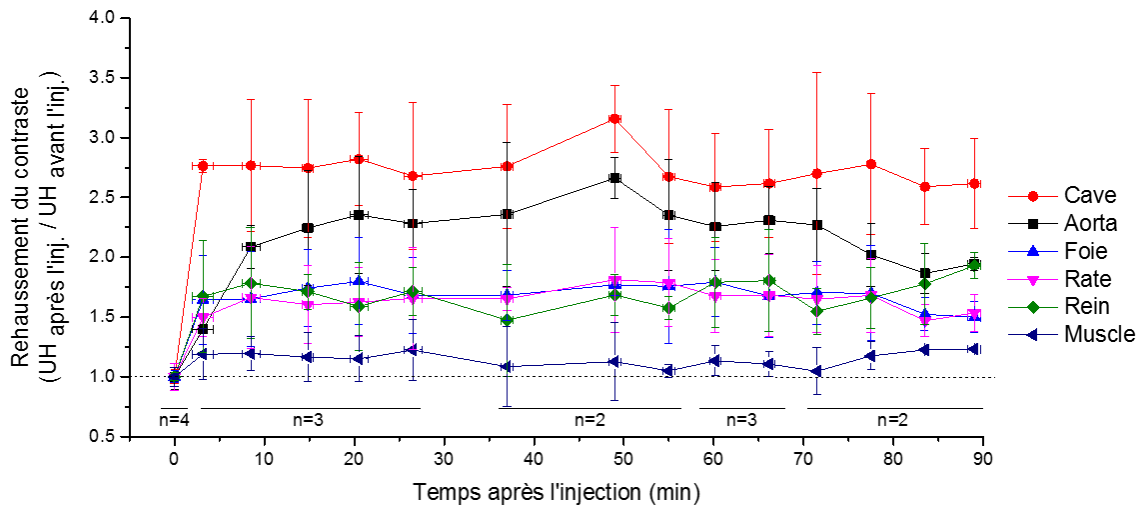


Figure 5. Études du rehaussement dynamique du contraste effectuées pendant 90 minutes après l'injection intraveineuse des Au NPs@PEG-Mn²⁺ dans des souris.

Cela ne serait sans doute pas possible si le revêtement des NPs était reconnu par les protéines opsonines, car cela conduirait à l'élimination rapide des NPs par les organes du système phagocytaire mononucléaire (ex. le foie et la rate). Ce ne serait pas non plus possible si les particules formaient de gros agglomérats, car cela déclenche également l'élimination des particules du sang.³⁰ De plus, les animaux ne montrent pas de signes de réactions indésirables au cours de l'expérience. Ces données indiquent la réalisation d'un revêtement polymère furtif sur la surface des NPs d'or synthétisées par ablation laser dans l'eau.

CONCLUSIONS

Les NPs d'or-gadolinium ou d'or-manganèse pourraient être avantageuses pour le diagnostic du cancer et pour la planification de la radiothérapie par TDM et l'IRM. Pour cette raison, la première partie de cette thèse a été consacrée à l'évaluation du potentiel de l'ablation laser en milieu liquide pour produire ces NPs pures en une seule étape. L'ablation laser de la cible de Au-Gd a mené à la formation d'un réseau de Gd₂O₃ contenant de petites NPs d'or. Bien que la formation de cette structure soit intéressante sur le plan fondamental, ce matériau composite ne convient pas pour l'application à titre de AC pour l'imagerie *in vivo* en raison de sa forme et de l'absence de stabilité en solution aqueuse. Nous avons ensuite testé l'ablation laser d'une cible de Au-Mn. Cette stratégie a permis la synthèse de petites NPs d'or (4,8 nm) couvertes

partiellement avec une couche mince (0,3 à 1,3 nm) d'oxyde de manganèse. Ces NPs contiennent environ 29% de Mn et 71% d'or (at. %). Ces NPs d'Au-MnO_x avaient la stabilité et la taille appropriée pour les applications d'imagerie biomédicale, mais l'état d'oxydation de la couche de manganèse était trop élevé pour permettre l'application de cette nanostructure comme un AC efficace pour l'IRM.

La dernière approche a consisté à fonctionnaliser les NPs d'or produites par ablation laser dans l'eau et à en modifier leur surface avec du PEG et des chélates de Mn²⁺. Bien que cette stratégie nécessite plusieurs étapes, elle a permis de produire un AC à base de NPs pour TDM et IRM. En effet, les NPs d'or produites par ablation laser en milieu liquide ont une surface libre de ligands et forment une suspension colloïdale dans l'eau. Par conséquent, les étapes de fonctionnalisation peuvent être effectuées dans des solutions aqueuses contenant un excès minimal de ligands. Le produit final a été caractérisé en détail afin d'étudier son potentiel pour l'imagerie biomédicale. Au cours de ces études, il a été possible de démontrer (1) que la stabilité colloïdale des NPs d'or est maintenue tout au long du processus de fonctionnalisation, en solution saline et en milieu de culture cellulaire; (2) que la taille ainsi que la biocompatibilité des NPs sont appropriées pour l'injection *in vivo*; et (3) que le colloïde final est bien adapté pour l'imagerie par TDM et IRM.

Ces résultats démontrent que l'ablation laser en milieu liquide s'avère être avantageuse pour la synthèse de NPs d'or en milieu liquide, particulièrement pour une application comme AC en imagerie médicale. La fonctionnalisation des NPs d'or au moyen d'un agent paramagnétique (ex. Gd³⁺ ou Mn²⁺) devrait être réalisée par post-greffage, au lieu d'introduire ces éléments dans la cible, pour contrôler l'état d'oxydation de l'agent paramagnétique.

TABLE OF CONTENTS

ACKNOWLEDGEMENTS.....	III
ABSTRACT	V
RÉSUMÉ.....	VII
SOMMAIRE RÉCAPITULATIF.....	IX
TABLE OF CONTENTS	XXIX
LIST OF TABLES.....	XXXIII
LIST OF FIGURES	XXXV
LIST OF EQUATIONS.....	XXXIX
LIST OF ABBREVIATIONS.....	XLI
PART I: SYNOPSIS	XLIII
1. INTRODUCTION	44
1.1 Hypothesis and general objectives of the research work	47
2. THEORETICAL BASIS AND LITERATURE REVIEW	48
2.1 Contrast Agents in MRI	48
2.2 Contrast Agents in CT	50
2.3 Dual CT/ MRI contrast agents	54
2.4 Pulsed Laser Ablation in Liquids	55
3. METHODOLOGY.....	59
3.1 Metal targets preparation	59
3.2 Nanoparticles synthesis by PLAL	60

3.2.1	Synthesis of Au-Gd, Au-Mn and Au NPs using KrF excimer laser.....	60
3.2.2	Synthesis of pure Au NPs using Nd-YAG laser.....	61
3.3	Functionalization of Au NPs with PEG and Mn²⁺-chelates	62
3.4	Physico-Chemical Characterization of Nanoparticles	63
3.4.1	UV-visible spectroscopy	63
3.4.2	TEM and EDS	64
3.4.3	HAADF HR-STEM and EELS.....	66
3.4.4	XRD	67
3.4.5	XPS.....	68
3.4.6	XAFS.....	69
3.4.7	ATR - FTIR	69
3.4.8	DLS and Zeta potential	70
3.4.9	Elemental analysis.....	72
3.4.10	CT imaging studies	73
3.4.11	MRI imaging studies	74
3.4.12	¹ H NMR	77
3.4.13	Cell toxicity Assay	77
4.	RESULTS AND DISCUSSION	79
4.1	Au-Gd nanocomposites synthetized by PLAL	79
4.2	Au-Mn NPs synthetized by PLAL	82
4.3	Au NPs synthetized by PLAL.....	87
4.4	Functionalization of Au NPs produced by PLAL with Mn²⁺-chelates	90
4.4.1	Colloidal stability and cytotoxicity of Au NPs@PEG-Mn ²⁺	96
4.4.2	CT/MRI dual imaging with Au NPs@PEG-Mn ²⁺ : a proof of concept.....	99
4.4.3	Preliminary biodistribution studies of Au NPs@PEG-Mn ²⁺	100
5.	CONCLUSIONS	102
5.1	Perspectives	105
PART II: ARTICLES	CVII	

ARTICLE 1: GOLD-MANGANESE OXIDE CORE-SHELL NANOPARTICLES PRODUCED BY PULSED LASER ABLATION IN WATER	108
ARTICLE 2: LASER-SYNTHESIZED LIGAND-FREE AU NANOPARTICLES FOR CONTRAST AGENT APPLICATIONS IN COMPUTED TOMOGRAPHY AND MAGNETIC RESONANCE IMAGING	135
6. REFERENCES	169
ANNEXE	184

LIST OF TABLES

Table 1.1 Clinical indications for the realization of MRI and CT for the diagnosis, treatment and surveillance of prostate and breast cancers recurrence, as well as recommended imaging protocols. ⁶⁻¹¹	45
Table 4.1 Relative percentage of Mn and Au atoms on Au-Mn NPs. The relative percentages were calculated based on elemental quantification obtained by XPS, EDS and NAA.....	85
Table 4.2 Zeta potential values (surface net charge) of Au NPs at the end of each functionalization step.....	94
Table 5.1 Longitudinal relaxivities (r_1) of nanoparticle-based “positive” MRI/CT contrast agents	104

LIST OF FIGURES

Figure 2.1 X-ray mass attenuation coefficient of gold, iodine, calcium and carbon within the X-ray energy range used for CT imaging. ¹⁰³	52
Figure 2.2 Illustration of the processes that lead to the synthesis of nanoparticles by laser ablation in liquids. Illustration produced based on references 37 and 39.	56
Figure 3.1 Schematic of the set-up used for the synthesis of Au-Gd, Au-Mn and Au NPs using a ns-laser with a wavelength of 248 nm.	60
Figure 3.2 Schematic of the set-up used for the synthesis of Au NPs using a ns-laser with a wavelength of 1064 nm.	61
Figure 3.3 Schematic of Au NPs before and after functionalization with PEG, DMSA-DTPA and Mn ²⁺ (Au NPs@PEG-Mn ²⁺). Enlarged sections display the chemical structure of DMSA-DTPSA-Mn ²⁺ complex and PEG.....	62
Figure 3.4 Possible signals emitted due to interaction of the incident electron beam with the thin specimen under analysis in TEM. ⁴⁸	65
Figure 3.5 Illustration of the electrical double layer formed at the surface of a negatively charged particle, when it is suspended in a liquid.	71
Figure 3.6 Illustration of the influence of an external magnetic field (B_0) on the rotational axes of the ¹ H protons.	74
Figure 3.7 Illustration of the effect of energy transfer from the radiofrequency (RF) pulse to the macroscopic magnetization vector (M). The energy delivered by the RF pulse to the ¹ H protons changes the position of the rotational axis to anti-parallel to B_0 , and induces precession in phase (A). Consequently, a magnetization vector perpendicular to B_0 is created (purple vector) (B). ..	75
Figure 3.8 Illustration of the loss of transversal magnetization (purple vector) and simultaneous recovery of the longitudinal magnetization or macroscopic magnetization vector (M) (red vector), and the time constants (T_1 and T_2) that characterize each process.	76
Figure 4.1 UV-visible absorption spectra of Au-Gd colloids obtained after pulsed laser ablation of Au-Gd target. (A) The target was immersed in solutions with different pH value and the spectra of the final colloids was compared to the spectrum of Au NPs produced at pH 11. (B) The target was ablated with different fluences at pH 11.....	79

Figure 4.2 X-ray diffractograms of Au-Gd colloids obtained by pulsed laser ablation of Au-Gd target in solutions at different pH value (A) or fluence (B).	80
Figure 4.3 TEM image of Au-Gd ₂ O ₃ colloid produced by pulsed laser ablation of Au-Gd target in a solution containing 0.1 g L ⁻¹ of PEG (scale bar: 20 nm) (A), EDS spectrum acquired on region 1 of TEM image, demonstrating the presence of only Gd (B), and EDS spectrum obtained from region 2 of the same image, evidencing spectra lines of both Au and Gd (C).....	81
Figure 4.4 UV-visible absorption spectra of Au-Mn NPs obtained after pulsed laser ablation of Au-Mn target in solutions at different pH values (A). Comparison of the UV-visible absorption spectrum of Au-Mn NPs produced in a solution at pH 11 with the spectrum of Au NPs produced after the ablation of Au target at pH 11 (B).....	82
Figure 4.5 X-ray diffractogram of Au-Mn NPs obtained after the ablation of Au-Mn target at pH 11 (A). EELS mapping of Au-Mn NPs produced under the same conditions (B). In this image, manganese is marked in red, whereas Au is represented in green.	83
Figure 4.6 HAADF HR-STEM micrographs evidencing the manganese shell (A) surrounding the Au core (B). On image (A), the arrows point to crystalline regions of the manganese layer, while the stars indicate amorphous areas.	84
Figure 4.7 TEM image and size distribution of the Au core in the Au-Mn NPs obtained after the ablation of Au-Mn target in a solution at pH 11 (scale bar: 10 nm).	84
Figure 4.8 High resolution XPS spectrum of O 1s core level from Au-Mn NPs.	86
Figure 4.9 SPR peak position of Au NPs in function of the ablation solution's pH (synthesis with a 248 nm ns-laser). The estimated Au NP diameters displayed in the colored regions were obtained from reference ¹⁵⁰ (A). PPI value in function of the ablation solution's pH. The relation between the PPI value and the degree of stability/ polydispersity of the Au NPs sample was obtained from references ⁴⁵⁻⁴⁶	88
Figure 4.10 TEM image and respective size distribution of Au NPs produced by pulsed laser ablation of a Au target immersed in a solution at pH 11, using a 248 nm (A) and 1064 nm (B) ns-lasers (scale bar: 5 nm).....	89
Figure 4.11 UV-visible absorption spectra (A and B) and DLS measurements (C) of the Au NPs produced with the 1064 nm ns-laser, at the end of each functionalization step. TEM image and size distribution of the Au NPs@PEG-Mn ²⁺ (scale bar: 20 nm) (D).....	91

Figure 4.12 High resolution XPS spectra of C 1s core level acquired at the end of each functionalization step.....	92
Figure 4.13 ART-FTIR spectra of Au NPs at the different steps of the functionalization procedure.	93
Figure 4.14 ^1H relaxation rates in function of the concentration of Mn in Au NPs@PEG-Mn $^{2+}$ at 37° C in 1.41 T.....	95
Figure 4.15 Hydrodynamic diameters of Au NPs@PEG-Mn $^{2+}$ suspended in water (A) and 154 mM NaCl (B). The measurements were performed during seven days after suspending the NPs in the different solutions.....	96
Figure 4.16 Hydrodynamic diameters of Au NPs@PEG-Mn $^{2+}$ suspended in complete cell medium. The measurements were performed during three days after suspending the NPs in this medium.	97
Figure 4.17 Cell toxicity studies of Au NPs@PEG-Mn $^{2+}$ (A) and Au NPs@PEG (B) on PC3 cancer cells.	98
Figure 4.18 <i>In vitro</i> CT (40 kVp) / MRI (1.0 T) imaging of Au NPs@PEG-Mn $^{2+}$ (A), and <i>in vivo</i> CT (40 kVp) / MRI (1.0 T) studies after injection of Au NPs@PEG-Mn $^{2+}$ in a PC3 CAM tumour model (B). The dashed white circle outlines the tumour area. The CT and MRI images were acquired after the intratumoural injection of Au NPs@PEG-Mn $^{2+}$ at different time points. The MR images, for both the <i>in vitro</i> and <i>in vivo</i> studies, were acquired using T_1 -weighted eco sequences.	99
Figure 4.19 DCE-CT (40 kVp_ studies performed during 90 minutes after intravenous injection of Au NPs@PEG-Mn $^{2+}$ in mouse models. Images show coronal sections the abdominal region in a representative mouse injected with Au NPs@PEG-Mn $^{2+}$. The graph displays the contrast enhancement before (0 min), and at different time points following the injection.	101

LIST OF EQUATIONS

Equation 3.1 Bragg's Law	67
Equation 3.2 Scherrer equation.....	67
Equation 3.3 Relation between binding and kinetic energies of the ejected photoelectron	68
Equation 3.4 Stokes-Einstein's equation	70
Equation 3.5 Henry's equation	72

LIST OF ABBREVIATIONS

ATR-FTIR: attenuated total reflectance fourier transform infrared spectroscopy / *spectroscopie infrarouge à transformée de Fourier et à réflexion totale atténuée*

CA: contrast agent / *AC: agent de contraste*

CAM: chorioallantoic membrane / *membrane chorioallantoïque*

CT: computed tomography / *TDM: tomodensitométrie*

CTAB: hexadecyltrimethylammonium bromide

DCE: dynamic contrast enhancement

DLS: dynamic light scattering / *diffusion dynamique de la lumière*

DMSA: 2,3-meso-dimercaptosuccinic acid

DOTA: 1, 4, 7, 10 - tetraazacyclododecane - 1, 4, 7, 10 - tetraacetic acid

DTPA: diethylenetriaminepentaacetic acid

EDS: X-ray energy-dispersive spectrometry / *analyse dispersive en énergie*

EELS: electron energy loss spectroscopy / *spectrométrie de perte d'énergie des électrons*

EXAFS: extended X-ray absorption fine structure spectroscopy /

HAADF: high angle annular dark field/ *champ sombre annulaire grand angle*

HCl: hydrochloric acid / *acide chlorhydrique*

HD: hydrodynamic diameter / *diamètre hydrodynamiques*

HR-STEM: high resolution scanning transmission electron microscopy / *microscope électronique à balayage par transmission en haute résolution*

ICP-MS: inductively coupled plasma mass spectrometry / *spectroscopie de masse à plasma à couplage inductif*

JCPDS: Joint Committee on Powder Diffraction Standards

KrF: krypton fluoride / *fluorure de krypton*

MP-AES: microwave plasma-atomic emission spectrometer / *spectroscopie d'émission atomique à plasma micro-onde*

MRI: magnetic resonance imaging / *IRM: imagerie par résonance magnétique*

MTT: 3-(4,5-dimethylthiazol-2-yl)-2,5-diphenyl tetrazolium bromide

NAA: neutron activation analysis / *analyse par activation neutronique*

NaBH₄: sodium borohydride

NaOH: sodium hydroxide / *hydroxyde de sodium*

Nd-YAG: neodymium-doped yttrium aluminium garnet

¹H-NMR: proton nuclear magnetic resonance spectroscopy / ¹H-RMN: *spectroscopie de résonance magnétique nucléaire du proton*

NPs: nanoparticles / *n nanoparticules*

PD: proton density

PEG: polyethylene glycol / *polyéthylène glycol*

PLAL: pulsed laser ablation in liquid

PPI: primary particle-index / IPP: *indice de dispersion des particules*

RF: radiofrequency

SPR: surface plasmon resonance / *résonance du plasmon de surface*

TEM: transmission electron microscopy / MET: *microscopie électronique en transmission*

TOAB: tetraoctylammonium bromide

XAFS: X-ray absorption fine structure / XAS: *spectroscopie d'absorption X*

XANES: X-ray absorption near-edge spectroscopy

XPS: X-ray photoelectron spectroscopy / *spectroscopie des photoélectrons*

XRD: X-ray diffraction/ *diffraction des rayons X*

PART I: SYNOPSIS

1. INTRODUCTION

Cancer is the leading cause of death in Canada. Prostate and breast cancers have shown the highest incidence since early nineties for men and women, respectively.¹⁻² In 2015, 24% of all new cancer cases in men were expected to be from prostate, whereas in women 26% of the new cases were estimated to be related to breast cancer. Due to the high incidence and, in some cases to late diagnosis, breast cancer represents the second cause of cancer death amongst women, while prostate cancer is the third for men. Unfortunately, predictions estimate that the incidence of these types of cancer will continue to rise in Canada, due to the growing and aging population.² Therefore, prevention, more efficient diagnosis and treatment tools are necessary to minimize the future burden that these diseases may bring to the Canadian population and the healthcare system.

Medical imaging techniques have a center role not only for the screening and diagnosis of cancer, but also for staging, therapy planning, image guided surgeries, treatment follow-up and surveillance of cancer recurrence.³⁻⁵ Magnetic resonance imaging (MRI) and computed tomography (CT) are commonly used for these investigations, especially after the diagnosis (Table 1.1).⁶⁻¹⁰

Current imaging protocols, for either MRI or CT, require the administration of an intravenous contrast agent (CA) to improve localization of the tumour, to acquire kinetic information for tumour characterization and to assess therapy response.^{4, 6, 9} Dynamic contrast enhancement (DCE) MRI studies use gadolinium chelates, whereas DCE-CT require iodine-based contrast medium. Both types of CA molecules distribute throughout all vascularized tissues and diffuse to the interstitial spaces after intravenous injection.⁴ In MRI, the most common analysis is qualitative, and relies on the fact that most prostate tumours show a faster contrast enhancement and CA washout, comparing with normal tissues.⁶⁻⁷ DCE-CT relies also on contrast enhancement by the tumour and quantitative analysis of this process.⁹ Although these methods provide good sensitivity and specificity, especially for the detection of prostate cancer, contrast enhancement by the tumour is non-specific.^{7, 9} In addition, these CAs are rapidly eliminated from the tumour and removed from the blood flow mainly by the kidneys, which restricts the time-window to acquire useful images.^{3-4, 12-13} This is a significant limitation for image guided procedures, in which repeated CA injections are necessary.³

Table 1.1 Clinical indications for the realization of MRI and CT for the diagnosis, treatment and surveillance of prostate and breast cancers recurrence, as well as recommended imaging protocols.⁶⁻¹¹

		Diagnosis	Staging	Therapy Planning/ Image guided surgery	Treatment follow-up/ Surveillance
Breast Cancer	MRI	Performed for detection and characterization: -High-risk patients; -Equivocal findings; -Contralateral cancer; -Occult primary tumour; -Recurrence, -Augmentation or reconstruction.	-Assess local extension of the disease.	-Tumour delineation and relationship with surrounding critical tissues; -Guidance for biopsy.	-Evaluation of treatment response (chemotherapy); -Assess the extent of residual disease (before surgical treatment).
		Imaging protocol: T_2 – weighted images; STIR/SPIR, DCE			
	CT	-	-Detect distant metastasis.	-Treatment simulation and dose calculation.	-
		Imaging protocol: acquisition before CA injection, DCE			
Prostate Cancer	MRI	Performed for detection and characterization: -PSA, DRE and TRUS guided biopsy are not conclusive.	-Assess local extension of the disease; -Detect distant metastasis.	-Tumour delineation and relationship with surrounding critical tissues;	-Post-therapy patients with PSA increase; -Radiotherapy recurrences.
		Imaging protocol: T_2 – weighted images, Diffusion weighted images, DCE			
	CT	-	-Detect distant metastasis.	-Treatment simulation and dose calculation.	-
		Imaging protocol: acquisition before CA injection, DCE			

DCE – Dynamic Contrast Enhancement; STIR – Short Tau Inversion Recovery ; SPIR – Spectral Presaturation with Inversion Recovery ; PSA – serum Prostate Specific Antigen ; DRE – Digital Rectal Examination; TRUS – Trans-Rectal Ultrasound.

Considering the frequency at which MRI and CT scans have to be performed for the diagnosis and during the treatment of prostate and breast cancers, the development of a dual-modality CA with extended blood half-life would have the potential to minimize frequent injections of different CAs and to provide longer time-windows for image acquisition.

Accordingly, different strategies have been taken to produce such multimodal CAs.¹⁴⁻²⁴ In that respect, nanoparticles (NPs) show great potential because (1) a single particle can carry hundreds to thousands of signalling molecules (or “functional” or “contrasting” atoms), which provides a localized and stronger signal for detection by the imaging equipment;²⁵ (2) NPs can be targeted to specific disease biomarkers, which increases imaging specificity;²⁶ (3) the core composition and surface of NPs can be designed to accommodate different types of CAs and drugs;²⁷ (4) the size, shape and coating of the NPs can be modified, which allows to tune the blood half-life and biodistribution;²⁸ and (5) NPs have a dimension scale similar to cells and in some cases to biological molecules, hence they can interact with cell receptors and to have pharmacokinetic properties different than molecular CAs or drugs.²⁹⁻³⁰

Nevertheless, multifunctional NPs, which are required for multimodal imaging, are complex to synthesize and this process can involve several chemicals. Extensive washing procedures are also often required.^{18, 20-21} Despite those long purification steps, the surface of the NPs may remain contaminated with chemical traces and reaction by-products.³¹ In fact, for NPs to receive the approval for use in clinical settings, their composition should be as simple and reproducible as possible.³² Thus, new techniques that allow single step synthesis of purer multifunctional NPs are necessary.

An example of such method is pulsed laser ablation in liquid (PLAL). This technique enables single-step synthesis of highly pure and electrostatically stabilized mono- and bimetallic NPs in aqueous solutions without the addition of reducing agents or stabilizing ligands.³³⁻³⁶ Consequently, the surface of the NPs is free of ligands and can be easily modified with other biocompatible molecules. The fact that the surface of these NPs is free from any ligands also permits higher surface coverage with the desired biocompatible molecules compared with chemically synthesised NPs.³⁷ Overall, NPs synthesised by PLAL could (1) improve the biocompatibility of nanomaterials for biomedical applications, (2) minimize excess of ligands necessary for surface functionalization, and (3) allow to significantly reduce the number of purification and ligand exchange steps.

1.1 Hypothesis and general objectives of the research work

Provided the benefits of using a dual CT/MRI CA in clinical practice, and the potential of PLAL to simplify the synthesis of multifunctional NPs as well as to improve their biocompatibility, the main objective of this thesis is to use PLAL to produce composite NPs that could be applied as a dual CT/MRI CA. These NPs would be made of gold (Au) and a paramagnetic material, such as manganese (Mn^{2+}) or gadolinium (Gd^{3+}). The first element, Au, is necessary for contrast enhancement in CT, whereas Gd^{3+} or Mn^{2+} are required to improve the image contrast in MRI.

Therefore, the specific objectives of this work are:

- synthesis and characterization of Au-Gd NPs produced by PLAL;
- synthesis of Au-Mn NPs by PLAL. This will be achieved following two different avenues. In the first one, Au-Mn NPs will be produced in one step using a mixed Au-Mn target and thoroughly characterized. In the second one, Au NPs will be initially prepared by PLAL and then modified with Mn^{2+} -chelates. These particles will be denoted as Au NPs@PEG- Mn^{2+} and will be characterized and used as CA for dual CT/MR imaging.

2. THEORETICAL BASIS AND LITERATURE REVIEW

2.1 Contrast Agents in MRI

The MR image is based on electromagnetic signals emitted from hydrogen (^1H) protons present in biological tissues. To achieve this, the ^1H protons are excited by a radiofrequency (RF) pulse emitted from a transmitter coil. After this signal is switched off, a receiver coil collects the signals generated during the relaxation of the ^1H protons.^{79 80} The main advantages of MRI are the outstanding soft tissue contrast resolution, the possibility to perform physiological studies and the absence of ionizing radiation (therefore no damage to the DNA).⁸⁰ MRI is strongly recommended for imaging of small tumours in abdominal and pelvic organs, brain and breast; to differentiate necrosis from edema; for joint injuries and cardiovascular studies.⁸¹ In the context of pre-clinical studies, MRI is also used for cell tracking studies.^{82 12}

In MRI, CAs change the image contrast indirectly by facilitating the relaxation of nearby ^1H proton-containing molecules. More specifically, MRI CAs act by shortening the relaxation times (T_1 and T_2) of tissues (these parameters are presented in more detail in the experimental section). For this, it is necessary to introduce paramagnetic ions or superparamagnetic NPs in the biological tissues.^{79, 83}

The paramagnetic elements affect the relaxation times through inner-sphere and outer-sphere interactions with the water molecules, which are the most common ^1H proton-containing molecules in biological tissues.⁸⁴ The first process is characterized by direct coordination between the unpaired electrons of the paramagnetic ion and the ^1H protons of the surrounding water molecules. The second process, the outer-sphere interaction, includes two types of interaction: (1) the ^1H protons form a hydrogen bond with the molecule chelating the metal ion and relax through dipole-dipole interaction, or (2) the magnetic moment of the metal ion causes inhomogeneity in the local magnetic field, which facilitates the relaxation of ^1H protons of water molecules diffusing nearby.⁸³ The most commonly used paramagnetic elements are Gd^{3+} and Mn^{2+} . The first metal ion has seven unpaired electrons, whereas the second has only five, so it has a weaker magnetic moment. In addition, both ions have symmetrical ground states, which induces a relatively slow electronic relaxation rates, thus facilitating the interaction with the ^1H protons of the surrounding molecules.⁶² Paramagnetic CAs produce a bright contrast, which

permits quantitative studies. In both cases, the free metal ions are toxic, so they have to be chelated (e.g. DTPA or DOTA) before biological administration.^{79, 85}

Unlike paramagnetic materials, the superparamagnetic CAs affect the relaxation of the surrounding water molecules mainly through outer-sphere interactions. These CAs are composed of iron oxide NPs (Fe_2O_3 , Fe_3O_4) surrounded by an organic coating.⁷⁹ Therefore, the magnetic moment generated by each NP is much stronger than the one of the individual paramagnetic metal ions, as it results from the sum of several Fe^{2+} or Fe^{3+} ions in the crystalline structure of a single NP. As a result, lower concentration of these materials are required to generate an appreciable change of the image contrast. However, this type of CAs produces a “negative” contrast (i.e. dark region in the image), can induce magnetic susceptibility image artifacts, and does not allow to perform quantitative studies.^{79, 85}

The US Food and Drug Administration (FDA) have approved gadolinium chelates for clinical applications, thus these are the most commonly used MRI CAs. These compounds are also quickly eliminated through the kidneys and are non-specific.⁸³ Therefore, several NP- or macromolecule- based formulations have been developed as blood-pool and tissue specific (e.g. liver and lymph nodes) CAs.^{62, 83, 85} For MRI, some iron oxide NPs formulations are clinically approved because iron can be metabolized in the lysosomes.³² On the other hand, paramagnetic NPs, made of Mn^{2+} , Mn^{3+} or Gd^{3+} are restricted to pre-clinical studies because the particles may leach toxic metal ions. Nevertheless, research studies continue to improve the design of these NPs (e.g. size, coating resistance, charge) in order to improve the relaxivity, the targeting ability and to minimize the residence time in the biological system.^{79, 83, 86}

2.2 Contrast Agents in CT

CT imaging is based on the differential absorption of a X-ray beam by the body, due to distinct tissue composition.⁸⁴ CT is therefore a method useful to study bone pathologies and trauma, calcification of tissues and lung diseases.¹² In addition, the short acquisition times make this technique useful for cardiac and vascular studies.⁸⁷⁻⁸⁸ CT systems are widely available and are relatively low cost compared to other imaging technique like MRI for example. In the pre-clinical field, microCT permits to obtain higher spatial resolutions (<50 µm) than clinical CT, and it also provides faster acquisition time than pre-clinical MRI. Therefore, microCT is also extremely useful in many research fields involving the development and treatment of small-animals disease models.^{12, 82}

In order to enhance the contrast of vascularised tissues, it is possible to inject a CA composed by an element that strongly attenuates X-ray radiation. For efficient attenuation, these molecules should absorb the X-ray photons mainly by photoelectric absorption.⁸⁴ The probability of an X-ray photon to interact with a given element varies as $(Z/E)^3$ (where Z is the atomic number and E is the photon energy), except for energies just above the binding energy of core electrons, at which the chance of absorption is significantly higher.^{84, 89} Therefore, any element with a high atomic number (Z) is a good X-ray absorber and can be used as a CT CA, given that it is not too toxic for biological applications.⁹⁰

The most commonly used and FDA approved formulations contain monomeric or dimeric water soluble tri-iodinated derivates of benzoic acid.^{13, 91} After intravenous injection, these small molecules diffuse to all vascularized tissues through the fenestrations of blood vessels. Then, they remain in the extracellular fluid, because of their high hydrophilicity, until they are removed by the blood and eliminated mostly through the kidneys.¹³ As these CAs have a short recirculation time (e.g. 15 - 40 seconds), the images should be acquired quickly after the injection. This is a significant limitation for pre-clinical studies, as the acquisition times of micro-CT are on the order of several minutes.⁸² Similar to image-guided procedures, in these situations the small animals often receive multiple or continuous injection of the CA.^{3, 82} At last, these poly-iodinated CAs are non-specific, which restricts their use for cellular/ molecular imaging research.^{13, 91}

These limitations were overcame by developing blood-pool CAs, which cannot cross through the gaps between endothelial cells of normal vessels, neither be quickly eliminated

through glomerular filtration, as their hydrodynamic diameter is usually larger than the pore size of the glomerular wall.⁹²⁻⁹³ The extended blood half-life of these molecules is also a result of delayed recognition by the cells of the mononuclear phagocyte system (MPS).⁹⁴

Different methods and materials have been used to produce these blood-pool CAs. Therefore, one can find commercially available different formulations of these materials for pre-clinical research.^{13, 82, 91} These blood-pool CAs can be made of macromolecules (e.g. dysprosium-DTPA-dextran), oil emulsions containing iodine modified lipids, micelles or liposomes with encapsulated iodine complexes, and inorganic NPs made of bismuth-sulfide, barium, gold or alkaline-earth metals.^{82, 90} Research studies dedicated to the development of new CAs demonstrated also the possibility of using other materials such as ruthenium/silicon oxide/Gd³⁺ labeled NPs, tantalum oxide NPs and iron/platinum alloy NPs.^{21, 90, 95} Polymeric nanoparticles (e.g. micelles and dendrimers) labelled with iodine molecules and Au NPs have also been studied.⁹⁶⁻⁹⁸ At last, NPs made of high-density lipoprotein^{22, 99} and low-density lipoprotein¹⁰⁰ containing Au NPs also showed promising results.

Among the previously described materials, those based on Au are the most explored because this element shows good biocompatibility and has higher X-ray attenuation coefficients than iodine within the energy ranges used in CT and microCT.¹⁰¹⁻¹⁰² Indeed, Au has a K-edge absorption at 80.7 KeV, hence when peak voltages ranging from 100 to 140 kVp are used for image acquisition, the mass attenuation of Au can be as high as 8.9 cm² g⁻¹.¹⁰¹⁻¹⁰² In comparison, the mass attenuations of C, Ca and I in the same energy range are 0.161, 0.366 and 3.51 cm² g⁻¹, respectively.¹⁰³ This suggests a X-ray attenuation approximately 55 times higher than C (present in soft tissues), 24 larger than calcium (present in bones) and 2.5 times larger than iodine (figure 2.1). As a consequence, in this range of energies, Au NPs can be administered at lower metal concentrations than the iodine-based CAs, and generate a similar level of contrast enhancement.^{101, 104}

As mentioned before, Au has also a great potential to be used as a CA, at least for pre-clinical applications, because it is chemically inert in biological media.¹⁰⁵ In addition, the size and shape of Au NPs are relatively easy to control, and ligands can be readily attached to their surface.¹⁰⁶ At last, Au NPs can also be used as radiosensitising agents for brachytherapy of different tumours.¹⁰⁷⁻¹⁰⁸

Hainfeld and colleagues were the first using Au NPs as CAs for vascular imaging in 2006.⁶⁵ Since then, several Au NPs-based formulations have been developed and used in pre-clinical

studies. As expected, these materials have shown long blood half-lives and no adverse reactions in mice.^{65, 104, 109}

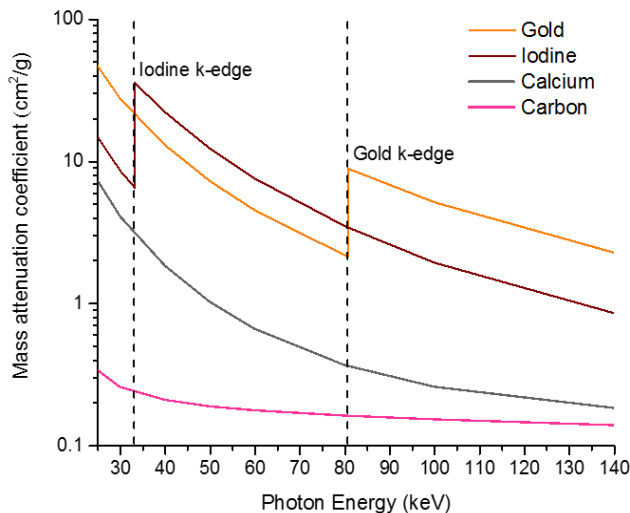


Figure 2.1 X-ray mass attenuation coefficient of gold, iodine, calcium and carbon within the X-ray energy range used for CT imaging.¹⁰³

The size, shape and surface properties of the Au NPs are determinant factors for their successful application as CAs.^{25, 30, 92-93, 110} Therefore, the design, synthesis method and functionalization procedure should be adjusted according to the aim of the final application. The majority of Au NPs used for CT imaging were synthesized either by the Turkevich¹¹¹, Brust-Schiffrin⁹⁹ or seed-mediated growth¹¹² methods. In the first technique, Au NPs are formed by citrate reduction of Au^{3+} ions in water.¹⁰⁶ Using this method, the size of the Au NPs can be tuned between 10 to 40 nm.¹¹³ The Brust-Schiffrin technique is used to produce very small Au NPs, usually with average sizes ranging from 1.5 to 5 nm. This is a two-phase synthesis strategy, in which Au salts are dispersed in toluene using tetraoctylammonium bromide (TOAB), and then reduced by sodium borohydride (NaBH_4). After reduction, the small clusters are stabilized with alkanethiols.¹¹⁴ At last, the seed-mediated synthesis is usually preferred to produce NPs with a specific shape, and also offers very good control over the particle size. In more detail, small Au NPs (seeds), formed through reduction of Au^{3+} ions by NaBH_4 , are used as templates for the growth of larger particles. Specific shapes are possible due to preferential adsorption on certain crystallographic facets of mildly reduced Au salts.¹⁰⁶ As a consequence of these distinct synthetic approaches, citrate molecules are used to stabilize the Au NPs obtained by the Turkevich method,

alkanethiols are adsorbed at the surface of the NPs in the Brust-Schiffrin synthesis,¹¹⁴ while hexadecyltrimethylammonium bromide (CTAB) are commonly used as stabilizers for NPs formed through the seed-mediated growth technique.¹⁰⁶

For the Au NPs to be used as a CAs for *in vivo* studies, the particles should meet the following criteria: (1) be water soluble; (2) form a stable colloid in biological media (significant ionic strengths and protein rich); (3) do not induce cytotoxicity; (4) do not adsorb proteins on their surfaces to avoid uptake by the MPS cells; and (5) be easily conjugated with specific ligands for targeting studies.^{25, 32, 92} Therefore, the Au NPs produced by the previous techniques should undergo ligand-exchange processes for their surface to be coated with different types of biocompatible, antifouling and/or biologically active molecules.^{39, 114}

The surface of Au NPs can be functionalized using molecules containing thiols, amines, carboxylic acids and phosphines.¹¹⁵ However, for *in vivo* applications, the anchoring group with higher affinity to Au is better to form more resistant coatings. Therefore, thiol modification is usually preferred, as the sulphur atoms form a coordinate covalent bond with the metal surface.³⁹ The surface of Au NPs stabilized with citrate or CTAB can be easily functionalized by exchanging these molecules with thiol containing ligands.¹¹⁴ The initial stabilizing agent is quickly replaced during the adsorption of sulphur atoms, followed by a slower reorganization and packing of the incoming molecules.^{39, 106} The surface of Au NPs stabilized by alkanethiols can be modified by thiol-thiol exchange.¹¹⁴ This process requires higher molar excess of the incoming ligands.³⁹ In addition, this method can also be used to produce mixed organic monolayers containing different types of ligands at specific ratios.¹¹⁴

Polyethylene Glycol (PEG) is a very successful and commonly used antibiofouling ligand for Au NPs used as CAs.¹⁰⁶ This advantage stems from the high hydrophilicity of this polymer, which permits to block electrostatic interactions with the NP surface, thus minimizing protein adsorption. Hence, PEG increases the circulation time of the Au NPs, providing long time-window for vascular imaging and boosting the probability for the NPs to accumulate in their targets.¹¹⁶ In addition, when specific binding to cell receptors or antigens is desirable, bifunctional thiolated PEG molecules can be used to coat the Au NPs. Then, targeting ligands (e.g. antibodies, peptides, aptamers, etc.) can be conjugated to the Au NPs surface using standard bioconjugation reactions.^{28, 106}

2.3 Dual CT/ MRI contrast agents

As summarised in Table 1.1, a combination of information from CT and MRI is often required for the diagnosis, staging and treatment planning of prostate and breast cancers.⁶⁻¹⁰ In addition, the utilization of both methods can be also beneficial image-guided surgeries as well as for cell tracking studies.^{14, 117} The first composite NPs designed for dual imaging by CT and MRI were reported in 2006. These formulations consisted in liposomes containing commercially available Gd³⁺-chelates and iodinated CAs,¹⁴⁻¹⁵ or very small Au NPs coated with Gd³⁺-chelates.¹⁶⁻¹⁷ In the following years, other formulations were suggested, such as the combination of Au with silica coated NaY/GdF₄: Yb, Er, Tm NPs,¹⁸ dendrimers conjugated to Au NPs and Gd³⁺-chelates,¹⁹ poly(acrylic acid) bridged Gd metal framework combined with Au NPs,²⁰ iron-platinum alloy NPs,²¹ Gd³⁺-chelates labelled HDL particles containing Au NPs,²² and different constructs combining iron oxide with Au NPs.²³⁻²⁴

Despite the possibility for dual imaging provided by these systems, some of them have relatively large hydrodynamic diameters, and the synthesis procedures are quite complex and involve several steps and purification procedures.^{18, 20-21} In fact, most of the synthesis methods reported require working at high temperatures, under inert atmosphere and employ several types of reducing and stabilizing agents as well as different organic solvents.^{17-18, 20-21} This can, unfortunately, compromise the purity of the nanomaterials, which is very important for biomedical applications. Therefore, researchers started to search for simpler and greener methods to produce such type of complex materials.

Narayanan *et al.* suggested the synthesis of Fe₃O₄/Au NPs using a phytochemical (e.g. proanthocyanidin) as reducing and stabilizing agent together with glutathione peptides. The synthesis procedures were also all carried in aqueous based solutions.¹¹⁸ In another work, Amendola *et al.* synthesized Au-Fe alloy NPs by PLAL and demonstrated for the first time the potential of using this method to produce to synthesize a multimodal CA.²³ However, as mentioned in the section about MRI CAs, superparamagnetic NPs create a “negative” image contrast and can induce image artifacts due to their large magnetic susceptibility.⁷⁹ These two characteristics make more difficult to observe image contrast changes (e.g. due to the presence of iron oxide NPs) in hypointense areas (i.e. darker regions in the MR image), and can accentuate spatial distortion in MR images, which is already a limitation when using this technique for radiotherapy planning.¹¹⁹⁻¹²⁰ On the other hand, paramagnetic materials enhance the image contrast (i.e.

“positive” CA), which is easier to perceive within hypointense regions, and it allows to perform quantitative studies.^{4, 117, 119, 121-122} Considering the advantages of paramagnetic elements as CAs for MRI, PLAL was used in the present work to produce dual CT/MRI CAs made of Au and paramagnetic materials.

2.4 Pulsed Laser Ablation in Liquids

PLAL started to be developed early in the nineties by two different research groups. Both groups used this method for the synthesis of various NPs types such as Au, Ag, Cu, Pd, Pt and Ni.¹²³⁻¹²⁴ Cotton also demonstrated the advantages of these materials for SERS applications compared with chemically synthetized NPs.¹²³ Therefore, these groups established from the very beginning the cornerstones of PLAL: simplicity, versatility and absence of organic contaminants.¹²³⁻¹²⁴

Afterwards, PLAL was investigated for the synthesis of NPs through the ablation of different materials, in different formats (e.g metal target, micropowders, colloids, metal salt) and solvents (e.g. water, acetone).³³ During this intensive research, Poondi and Singh revealed the possibility of synthetizing metastable alloy nanoparticles, which could not be obtained by conventional methods.¹²⁵ In fact, PLAL offers a unique reactive environment for the synthesis of composite NPs and metastable materials because of the extreme pressure and temperature attained in the plasma and cavitation bubble (due to liquid confinement) as well as the sudden cooling of the plasma plume.^{33, 126-127}

The most basic set-up for the synthesis of NPs by PLAL consists in immersing a metal target in a liquid, followed by irradiation of the target surface with a pulsed laser during a defined time.³³ Due to some limitations in time resolution, and sensitivity of techniques (used to study the laser ablation process and NPs formation) as well as the complexity of the multiple physical processes involved, the understanding of the laser ablation process and consequent NPs' formation is not yet complete.^{33, 128}

In short, and simplifying some complex physical concepts, the process leading to NP formation begins after absorption of the laser light by the target, which causes heating and photoionization of the irradiated metallic surface (figure 2.2 (1)). As a consequence, material is released from the surface of the target.^{33, 129} In fact, the extreme heating can induce boiling and explosion of the target material, while photoionization produces vaporization. As a result of these

phenomena, liquid drops and target fragments can be emitted from the target in addition to the vaporized reactive species.^{33, 129-130} The emission of vaporized material leads to the formation of a plasma, which contains very high concentrations of ionized species. Therefore, the plasma begins to expand at high speed, and this enlargement is accompanied by a shock wave (figure 2.2 (2)).¹³¹

During the expansion, the plasma loses energy quickly to the surrounding liquid (i.e. plasma cooling), which leads to the appearance of a thin layer of vaporized liquid all over the plasma-liquid interface (figure 2.2 (3)). The formation of a primary set of NPs seems to occur at this stage, as the loss of energy induces reduction of ions into neutral elements and subsequent nucleation and growth of the NPs.^{127, 131} Studies have demonstrated that the temperature in the core of the plasma remains relatively constant (despite the progressive cooling), therefore the NPs are formed under steady thermo-dynamic environments.¹³¹

Throughout plasma cooling, a cavitation bubble originates from the vaporized liquid layer (figure 2.2 (4)). The vapor layer/early cavitation bubble starts to expand in all directions due to the high temperature and pressure inside this cavity. During the expansion of the bubble, the NPs formed inside the plasma are pulled out to the cavitation bubble and diffuse inside. The primary set of NPs, may also coalesce, aggregate or continue to grow inside the cavitation bubble.^{128, 131} After reaching its maximum expansion (figure 2.2 (5)), the cavitation bubble begins to contract until it collapses. During the retraction process the NPs are strongly compressed into a small bubble, therefore they start to diffuse out of the cavitation bubble even before the collapse (figure 2.2 (6)). Finally, when the bubble collapses all the NPs are released into the surrounding liquid (figure 2.2 (7)).¹³¹

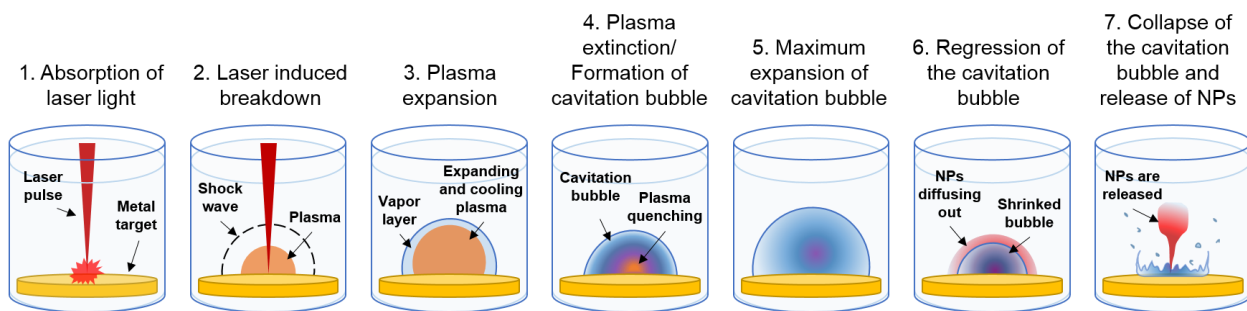


Figure 2.2 Illustration of the processes that lead to the synthesis of nanoparticles by laser ablation in liquids.
Illustration produced based on references 37 and 39.

The thermodynamic conditions that govern NPs formation, and that determine the final composition and morphology are dependent on the laser parameters and surrounding liquid.¹³²^{35, 127} Therefore for laser-based synthesis of NPs in liquids it is important to consider the influence of parameters such as the laser wavelength, pulse width, laser fluence, repetition rate, ablation time, and composition of liquid solution.^{33, 45} Generally, all the laser wavelengths are suitable for the synthesis of NPs, as long as the fluence delivered on the surface of the target is high enough to produce ablation of the material. However, in order to optimize the ablation rate and to avoid fragmentation or melting of NPs formed due to ablation of the target, the laser wavelength should not be strongly absorbed by the liquid medium, neither by the NPs.^{57, 66}

The pulse width influences the NPs formation in the plasma plume and the ablation process. Thus, ultra-short pulses (e.g. fs) only cause material ejection from the irradiated area, whereas longer pulses (e.g. ps and ns), which are long enough to permit heat conduction, cause material detachment from an area larger than the irradiation zone.¹³⁰ Regarding the NP formation, ns pulses can be absorbed by the plasma plume, which increased photoionization of the material inside the plasma, but it decreases the ablation rate. On the other hand, ps or fs pulse widths, which cease before the plasma plume is formed, permit an increase of the ablation rate because all the energy of the laser pulse is transmitted to the target.³³

The laser fluence is the energy absorbed by the target by unit of area. Therefore it needs to be high enough to ablate a quantity of material that produces a concentration of metal ions inside the plasma plume suitable for NPs formation.³³ After overcoming the ablation threshold energy, increasing fluence can also have an impact on the amount and size of the NPs ejected.⁵⁷ Similarly to the fluence, the repetition rate and the ablation time also influence the energy absorbed by the target, thus these parameters have an important impact on the production rate of NPs.^{33, 130}

At last, the liquid medium can be used to control the NPs size, polydispersity and to improve the long-term stability of the colloids by adding limited concentrations of different anions, anionic surfactants or thiol terminated molecules.^{37, 45-46} As mentioned earlier, PLAL also permits the synthesis of NPs in organic solvents.³³ However, for *in vivo* applications, aqueous solutions provide higher surface purity.

The main advantage of PLAL over conventional colloidal chemistry methods, especially for the biomedical field, is the possibility to produce NPs in water without using reducing or stabilizing chemicals, as mentioned in the introduction.⁴⁵ As a result, the surface of the NPs is

free of ligands and readily available for the conjugation with other molecules.⁴⁵ Moreover, many reducing chemicals used in colloidal synthesis may be toxic, especially when the NPs have to be administered at relatively high concentrations, such as in the case of CT imaging with Au NPs. Additionally, the ligand-free surface allows to avoid extensive purification processes, aggregation associated with ligand exchange procedures and product losses during these extra steps.¹³³ Therefore, in this thesis, all the NPs were produced by pulsed laser ablation in de-ionized water. In addition, the colloidal stability and the size distribution were improved by adding NaOH to the ablation solution, as described in more detail in the following chapter.

3. METHODOLOGY

3.1 Metal targets preparation

The metal targets used for NPs synthesis by PLAL were prepared by mechanically mixing metallic micro-powders of Au and Gd or Mn, and by compressing them with a hydraulic press. In brief, Au micropowder (0.432 g, <10 µm) and Mn metal micropowder (0.068 g, <10 µm,) or Gd metal micropowder (0.222 g, <44 µm) and Au micropowder (0.278 g, <44 µm) were thoroughly mixed at an atomic ratio of 64% Au/ 36% Mn and at 50% Au/ 50% Gd, and poured into an steel die. The mixture was compressed with a hydraulic press for 10 minutes under a pressure of 10 T. Metallic disks, 0.9 mm thick and 8.0 mm in diameter, were obtained and used for laser ablation in liquid. The main factors considered for the manufacture of these targets were (1) the size of the micro-powder (i.e. the smallest size commercially available was used), and (2) the average size of the mixed powders (i.e. Au and Gd or Au and Mn) was the closest possible. These two factors were important to maximize homogeneous distribution of both elements in the target.

The atomic ratio of the elements mixed in the target was based on the Au-rich alloys that could be formed according to the binary phase diagram of each mixture (e.g. Au-Gd and Au-Mn).³⁸ In more detail, for the Au-Gd system, most of the possible Au-rich alloys occur under 50% (at.) of Gd, while in the Au-Mn system, most of the solutions happen at Mn atomic percentages lower than 36% of Mn. Au-rich alloys were preferred for the application of these materials as dual CT/MRI CAs, because CT requires higher concentrations of Au (e.g. on the order of tens of mM), comparing with the concentrations of Gd³⁺ or Mn²⁺ (e.g. on the order of few mM) to achieve significant contrast enhancement. Therefore, the synthesis of Au-Gd NPs was performed using a Au₅₀Gd₅₀ (at. %) metal target, whereas a Au₆₄Mn₃₆ target was used to produce Au-Mn NPs. For the synthesis of Au NPs, high purity Au metal targets were used (Au₁₀₀).

3.2 Nanoparticles synthesis by PLAL

3.2.1 Synthesis of Au-Gd, Au-Mn and Au NPs using KrF excimer laser

The synthesis of NPs using a krypton fluoride (KrF) excimer laser (wavelength: 248 nm, pulse width: 20 ns) was performed using the set-up represented in figure 3.1.

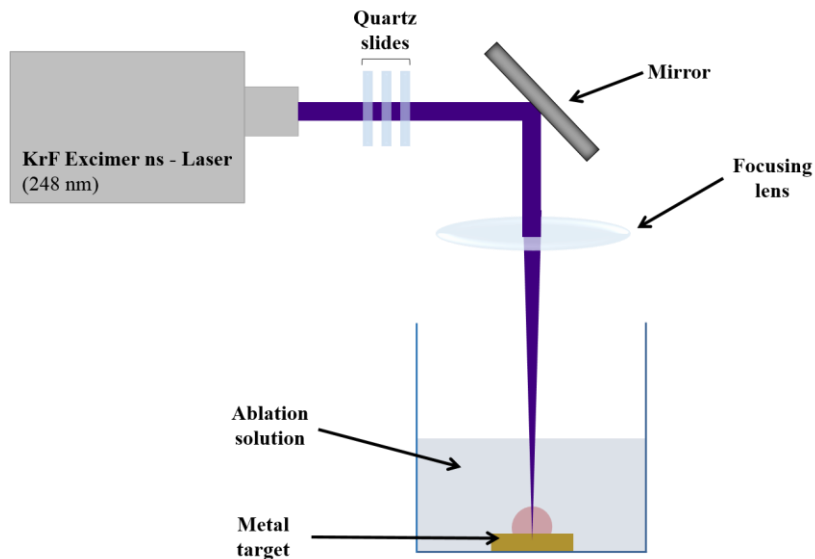


Figure 3.1 Schematic of the set-up used for the synthesis of Au-Gd, Au-Mn and Au NPs using a ns-laser with a wavelength of 248 nm.

As exemplified in the previous scheme, the metal target was fixed on the bottom of a 10 mL beaker, and the laser was focused on the surface of the target. Afterwards, the beaker was filled with 4 mL of de-ionized water supplemented with sodium hydroxide (NaOH), hydrochloric acid (HCl) or 0.1 g L⁻¹ of PEG (3 kDa), depending on the aim of the experiment as it will be discussed later in the results section. The height of liquid above the target (8.5 mm), the repetition rate (20 Hz) and the ablation time (2 minutes) were kept constant for all the experiments. For the synthesis of Au-Gd NPs, the Au₅₀Gd₅₀ metal target was ablated using a fluence of 250 J.cm⁻² to study the influence of the ablation solution pH, or varied to study the effect of fluence. This parameter was varied using quartz slides to attenuate the laser beam. For the ablation of the Au₅₀Gd₅₀ target using the solution containing PEG, a fluence of 10.9 J cm⁻² was used. On the other hand, Au-Mn NPs and pure Au NPs were produced through the ablation of a Au₆₄Mn₃₆ and

a Au_{100} metal target, respectively, using a fluence of 66.7 J.cm^{-2} . Before physico-chemical characterization, the colloids were centrifuged to remove possible target fragments and larger particles.

3.2.2 Synthesis of pure Au NPs using Nd-YAG laser

The synthesis of Au NPs with a Nd-YAG ns-laser (wavelength: 1064 nm, pulse width: 8 ns) was performed using the set-up represented on figure 3.2.

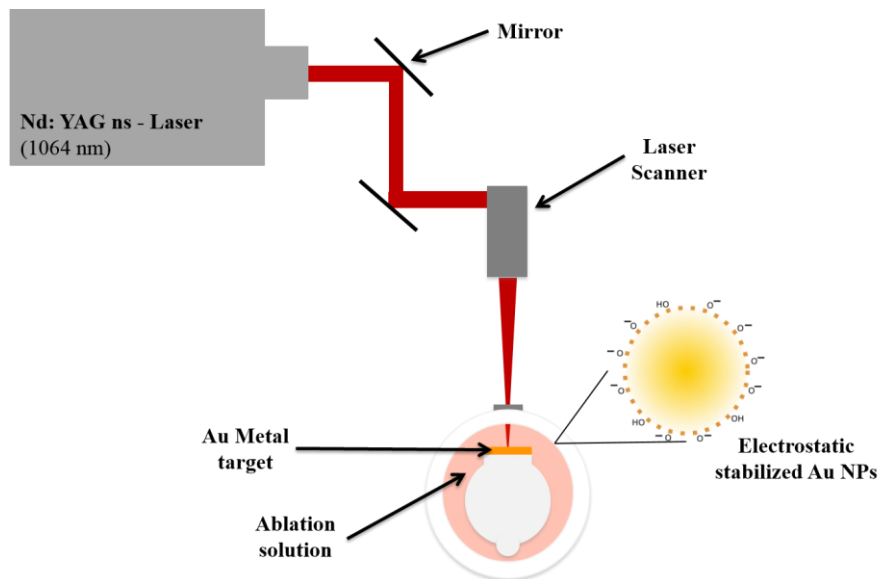


Figure 3.2 Schematic of the set-up used for the synthesis of Au NPs using a ns-laser with a wavelength of 1064 nm.

In this set-up, the metal target was fixed inside a custom made ablation chamber, which includes a motorized stirrer to avoid NPs accumulation close to the ablation region, and had a 30 mL capacity.¹³⁴ In addition, the laser beam was horizontally directed to the target surface and was scanned on the target surface during ablation. The synthesis was performed using an aqueous solution containing 3.3 mM of NaOH (pH 11). The liquid layer crossed by the laser before reaching the target surface was 3 mm-thick, and the target was irradiated during 5 minutes using a laser energy of 367 μJ per pulse and a repetition rate of 15 kHz. After the synthesis, the Au colloids were centrifuged to eliminate most of the target fragments and large NPs that were inevitably formed due to the mechanisms involved in the formation of NPs synthesized by PLAL.³³ The infra-

red (IR) wavelength laser was used in order to increase the production rate of Au NPs, because these particles have a weaker light absorption in this regime.³³

3.3 Functionalization of Au NPs with PEG and Mn²⁺-chelates

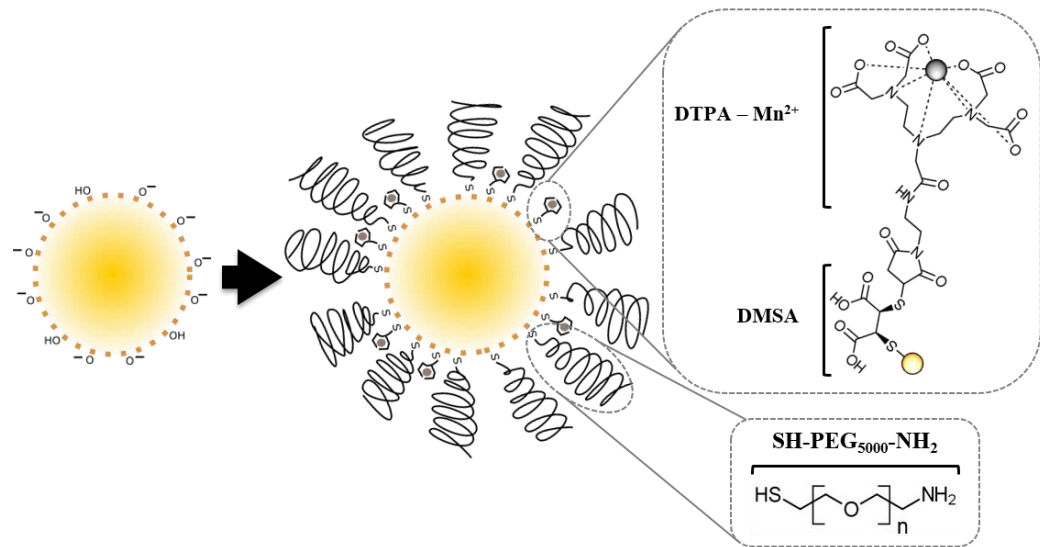


Figure 3.3 Schematic of Au NPs before and after functionalization with PEG, DMSA-DTPA and Mn²⁺ (Au NPs@PEG-Mn²⁺). Enlarged sections display the chemical structure of DMSA-DTPA- Mn²⁺ complex and PEG.

The Au NPs synthesized with the PLAL set-up described in the previous section were functionalized with PEG and Mn²⁺-chelates to produce a composite structure similar to the represented in figure 3.3. For this, the Au NPs were first coated with heterofunctional PEG (NH₂-PEG-SH, MW 5 kDa) to be sterically stabilized. The thiolated (-SH) end of the PEG molecules was grafted to the Au NPs surface, while the amine function (-NH₂) at the opposite extremity could be used for later modification of the NPs with targeting ligands. A 5 kDa polymer was chosen because this molecular weight provided a good compromise between final hydrodynamic diameter (HD), extended blood half-life, and a viscosity suitable for *in vivo* administration of Au NPs with concentrations on the order of tens of mg mL⁻¹.^{94, 135}

In order to functionalize the Au NPs' surface with PEG, these molecules were dissolved in de-ionized water and added to the alkaline solution containing the Au NPs. The ratio of PEG molecules to Au NPs was 1000:1. Considering that the expected number of binding sites available on the surface of a 8 nm Au NPs is approximately 503 (calculated assuming a perfect sphere

model and a molecule foot print of 0.4 nm^2),^{42, 67, 136} in this work it was used only a two times excess of ligands (e.g PEG molecules). The incubation of PEG with the NPs was performed overnight to maximize the packaging and ordering of the PEG molecules at the NPs' surface.³⁹ The resultant colloid was dialyzed to remove the excess of PEG and NaOH.

Afterwards, the Au NPs@PEG were mixed with DMSA (2,3-meso-dimercaptosuccinic acid) conjugated to maleimido-mono-amide-DTPA. These molecules were conjugated through the maleimide function of DTPA, which reacted with a sulfhydryl group from a DMSA molecule (figure 3.3). DMSA is a nontoxic molecule, hence it was used as a linker to bind DPTA to the surface of Au NPs.¹³⁷⁻¹³⁸ DTPA was chosen as a chelating agent, because it is commonly used in clinically approved CAs, and it forms a relatively stable complex with Mn^{2+} .⁴⁰ After incubating this mixture with the Au NPs for few hours, the colloids were again dialyzed to remove excess of DMSA-DTPA ligands. At last, the Mn^{2+} was added for chelation by the DTPA. In this work Mn^{2+} was chosen because this paramagnetic ion is less toxic than the commonly used Gd^{3+} .⁴⁰

3.4 Physico-Chemical Characterization of Nanoparticles

3.4.1 UV-visible spectroscopy

UV-visible absorption spectroscopy is a useful method to investigate optical properties of colloids. For this, the different colloidal suspensions were dispensed in a quartz cuvette, which was placed in the UV-visible equipment and then illuminated by different wavelengths. Afterwards, a detector records the transmitted light, and the equipment software provides a spectrum in which absorption values are displayed for each wavelength.⁴⁷ Especially when working with Au spherical NPs, UV-Visible spectroscopy is a quick method to estimate (1) the size of the NPs, (2) the polydispersity or the presence of aggregates/ agglomerates, (3) the concentration of the colloids, as well as (4) to monitor the extent of surface functionalization of the NPs with different molecules.

The size of the Au NPs was estimated based on the position of the surface plasmon resonance (SPR) band. This strong absorption peak occurs when the illuminating wavelength matches the natural frequency of the oscillating surface electrons.⁴¹ This resonant frequency also depends on the refractive index of the medium surrounding the NPs and composition of the NPs, therefore UV-Visible spectroscopy was also used to assess the formation of Au composite structures, and to follow surface modification of Au NPs.⁴²⁻⁴³

This method was used for preliminary assessment of colloidal stability and polydispersity, using the primary particle-index (PPI), which was calculated by performing the ratio between the absorption at 380 nm and at 800 nm (at this wavelength increased absorption indicated that light was scattered by large particles or aggregates).⁴⁷ Thus, a high PPI indicated that the samples contained a low percentage of aggregates/ large particles, which has been associated with lower polydispersity and higher colloidal stability.⁴⁵⁻⁴⁶ At last, the concentration of Au in the solution was calculated based on the absorption at 380 nm, which is due to inter-band transition of Au atoms.⁴⁴ For this, a correlation curve was obtained using Au NP standards of known concentration.

The UV-Visible absorption results described in this thesis were obtained using a Varian spectrometer (Cary-1E) at INRS-EMT or a UV-1600 spectrophotometer model from Shimadzu at the CR-CHUQ.

3.4.2 TEM and EDS

Transmission electron microscopy (TEM) was used to observe the morphology and to measure the diameter of the different types of NPs produced. TEM uses a narrow electron beam to produce high-resolution images. For this, a thin specimen is placed in a high vacuum column and irradiated with a beam of accelerated electrons, which can either be transmitted through the sample without losing energy (direct beam, figure 3.4), or interact with the atoms in the sample. The electrons that are transmitted through the sample are used to form a 2D transmission image of the specimen that can be observed on a fluorescent screen or recorded as a digital image. On the other hand, interaction of the electron beam with the sample can lead to electron energy loss, scattering, emission of secondary electrons or characteristic X-rays from the irradiated sample, as represented by the blue arrows in figure 3.4.⁴⁸

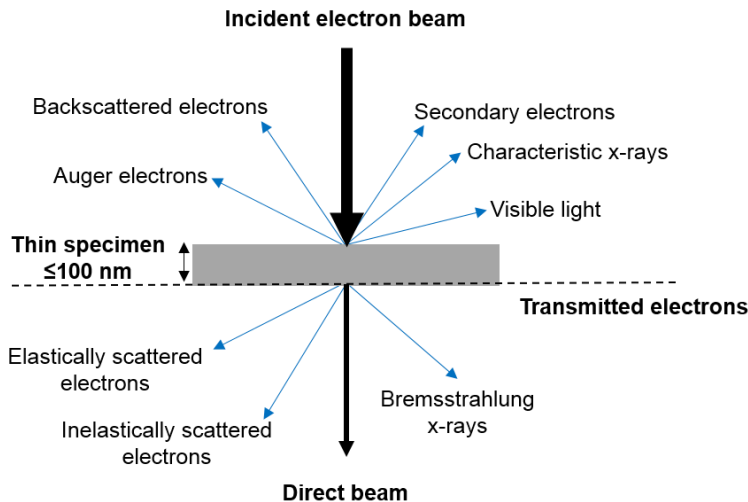


Figure 3.4 Possible signals emitted due to interaction of the incident electron beam with the thin specimen under analysis in TEM.⁴⁸

TEM is usually equipped with a x-ray detector to collect the characteristic X-rays emitted by the specimen upon interaction with the electron beam. This technique, X-ray energy-dispersive spectrometry (EDS) allowed to identify the elements of the sample as well as to perform relative quantification.⁴⁸

The TEM image acquisition and EDS analysis were performed using a JEM-2100F model (JEOL). This equipment is located at École Polytechnique de Montréal. The average size measurements were performed using ImageJ software.

3.4.3 HAADF HR-STEM and EELS

High angle annular dark field (HAADF) high resolution (HR) - scanning transmission electron microscopy (STEM) is a TEM variant in which different operation modes are combined to produce images with atomic resolution and Z-dependent contrast.⁴⁹ In more details, STEM is an operation mode in which the incident electron beam is convergent and it is used to scan the sample. This mode permits higher spatial resolution than parallel beam TEM (described in the previous section) and, when used alone (i.e. without combination with HAADF mode), this method allows the use of other analytical techniques such as electron energy loss spectroscopy (EELS). HR is another operation mode in which instrumental and lens improvements as well as numerical corrections permit to produce images with resolutions down to the lattice fringes and often the individual atoms aligned in those plans.⁴⁸ At last, HAADF is a common STEM imaging mode which allows to enhance the image contrast related with the thickness and the Z number of the elements. For this, an annular detector is used to collect the transmitted electrons scattered at high angles.⁴⁹

EELS provides a chemical analysis for elemental identification. This method provides an energy distribution of the transmitted electrons. Some of these electrons did not lose energy crossing the sample (elastically scattered electrons, figure 3.4), while others collided with electrons from the elements in the sample and lost specific amounts of energy (inelastically scattered electrons, figure 3.4). The last group of transmitted electrons is therefore useful for analysis of the chemical composition of the samples as well as providing information about the chemical environment and valence state of a specific element.⁴⁸

The Au-Mn NPs were observed using a FEI Titan 80-300 high base cubed microscope, which is located at McMaster University. The image acquisition and EELS analysis were performed by Dr. Andreas Korinek and Dr. Mathieu Bugnet (Dr. G. Botton's team).

3.4.4 XRD

X-ray diffraction (XRD) was performed to characterize the crystalline structure of the samples and for crystallite size calculation. In this method, a X-ray beam strikes a crystalline sample in a range of specific incident angles. Interaction of the X-ray beam with the atoms located in different crystallographic planes of the sample causes scattering of the incident beam. When the scattered waves meet the requirements of Bragg's Law (eq. 3.1), there is constructive interference, thus diffraction occurs and the diffracted beam can be detected.⁵⁰

$$n \lambda = 2 d \sin \theta$$

Equation 3.1 Bragg's Law

Where n is an integer number, λ is the X-ray wavelength, d is the spacing between the parallel crystal planes, and θ is the incident angle.

A plot of the intensity of diffracted x-rays in function of the diffraction angle (2θ) is obtained. Comparison of the sample's diffractogram with the diffraction patterns database provided by the Joint Committee on Powder Diffraction Standards (JCPDS) allowed the identification of the various crystalline phases.⁵⁰ At last, the crystallite size of the NPs was calculated using the Scherrer formula (eq. 3.2), which correlates the width of the diffraction peaks with the average crystal size.⁵⁰

$$t = \frac{0.9 \lambda}{B \cos \theta}$$

Equation 3.2 Scherrer equation

Where t is the mean crystal size, λ is the X-ray wavelength, B is the diffraction peak width at half maximum intensity, and θ is the incident angle.

For XRD experiments a Bruker D8 Advanced diffractometer (Cu K_α radiation at 1.5418 Å) was used at INRS-EMT. The analysis of the diffractograms were performed using the X'Pert High Score software.

3.4.5 XPS

X-ray Photoelectron Spectroscopy (XPS) was used to study the chemical composition of samples' surfaces. In this technique a sample is placed inside a vacuum chamber and irradiated with a monochromatic X-ray beam to excite and release inner-shell electrons from the atoms present in the sample. The photoelectrons are ejected from the atom with a specific kinetic energy (E_k), which can be measured and used to identify the element from which the photoelectron was removed. This identification is based on the electron binding energies (E_b), which have characteristic values for each element. Kinetic energy is related to binding energy through the following formula (eq. 3.3):⁵¹

$$E_b = h\nu - E_k - \Phi$$

Equation 3.3 Relation between binding and kinetic energies of the ejected photoelectron

Where, h is the Planck's constant, ν is the frequency of the incident x-ray photon, and Φ is the work function.

The final XPS spectrum usually displays measured photoelectron intensity in function of the binding energy. Binding energy shifts can also be used to determine the valence state of the atom or its participation in different chemical bonds, which can be used to identify specific molecules or functional groups present on the surface of the NPs. In addition, XPS allows the quantification of surface composition based on the photoelectric peak area (after background subtraction) and on the application of a sensitivity factor.⁵¹

In the present work, XPS measurements were performed with a VG Escalab 220i-XL using a monochromatic aluminium source (K_α 1486.6 eV) at INRS-EMT or a PHI 5600-ci spectrometer using a non-monochromatic aluminum X-ray source for survey spectra and a non-monochromatic magnesium source (K_α 1253.6 eV) for the acquisition of high resolution spectra. This equipment is located at CR-CHUQ and the spectra acquisitions were performed by Dr. Pascale Chevallier.

The deconvolution and analysis of the high resolution spectra was performed with CasaXPS software

3.4.6 XAFS

X-ray absorption fine structure (XAFS) was performed to analyze the local chemical environment and to determine the oxidation state of Mn on the Au-Mn NPs.

The information obtained by this method is based on X-ray absorption by the atoms at the energies near and above the binding energy of the core electrons. For data interpretation, the X-ray absorption spectrum is divided in two regions (1) X-ray absorption near-edge spectroscopy (XANES) and (2) extended X-ray absorption fine structure spectroscopy (EXAFS). The different regions are used to collect distinct information about the atoms studied. In brief, XANES spectrum provides useful information about the valence state and coordination chemistry, whereas the EXAFS spectrum is used to estimate bond distance, coordination number and to determine neighbor atoms.⁵²

XAFS data acquisition, analysis and interpretation were performed by Daniel M. Chevrier (Prof. P. Zhang's team) at Dalhousie University.

3.4.7 ATR - FTIR

Attenuated total reflectance Fourier transform infrared spectroscopy (ATR-FTIR) was used to investigate the presence of specific bonds, characteristic of the different organic molecules used for functionalization of Au NPs. In this method, infrared light is first altered by an interferometer and then the recombined beam is used to irradiate the sample deposited on the top of a silicon crystal. The organic molecules on the sample absorb infrared waves with the same frequency of their vibration modes. Then, the light reflected from the sample is collected by the FTIR detector, and Fourier transform is applied to convert the interferogram in an infrared spectrum, which displays absorbed light in function of the wave wavenumber.⁵³

For this analysis a Cary 660 FTIR model from Agilent Technologies was used at CR-CHUQ.

3.4.8 DLS and Zeta potential

Dynamic light scattering (DLS) was used to measure the hydrodynamic diameter (HD) of the NPs. The HD is defined as the diameter of a hard sphere which moves at the same speed as the solid particles under investigation. Therefore, this dimension depends on the core size of the particle (measured by TEM), on the ionic concentration of the solution as well as on NP surface coating. For the DLS measurement, the colloid is dispensed in a cuvette and illuminated by a laser. When the NPs are in suspension they undergo Brownian motion, and the speed of this movement can be calculated by the DLS software after detecting the intensity of the light scattered due to interaction of the photons with the electric field of the particles. The intensity of the scattered light fluctuates in time. Thus, these oscillations are analyzed using a correlation function that relates the average light intensity with the time at which the fluctuations were detected. The Brownian motion speed or translational diffusion coefficient (D) can be derived using the correlation function. At last, the HD is calculated by the software using the Stokes-Einstein equation (eq. 3.4).⁵⁴

$$HD = \frac{k T}{3 \pi \eta D}$$

Equation 3.4 Stokes-Einstein's equation

Where, k is the Boltzemann's constant, T is the absolute temperature, η is the viscosity, D is the diffusion coefficient.

The DLS measurements were performed using a Nano S Zetasizer system at CR-CHUQ.

Using an equipment similar to the one required for DLS measurements, one can also measure the zeta potential (surface net charge of the NPs). In more detail, when the particles are in solution, there is an electrical double layer surrounding them (figure 3.5).

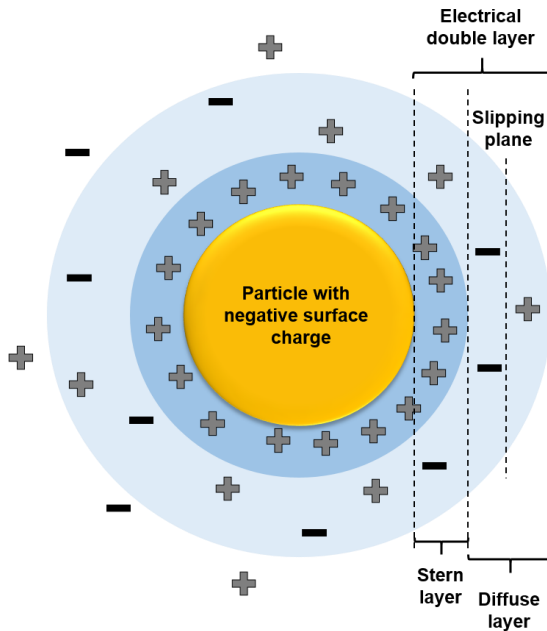


Figure 3.5 Illustration of the electrical double layer formed at the surface of a negatively charged particle, when it is suspended in a liquid.

This layer is formed because ions with opposite charge are attracted to the NP surface. As the name suggests, this layer is composed by two regions (1) the Stern layer, in which the counter ions are strongly adsorbed on the NP surface and the (2) diffuse region where the ions are loosely bound and their concentration is decreased. When the particles move in the liquid, some ions from this outer layer can accompanied the movement, while others located further away from the surface will not be dragged. The boundary separating these two behaviors is called slipping plane and the zeta potential measures the net charge at this interface. To measure the zeta potential, an electric field is applied to the solution containing the NPs, to drag the particles in the liquid. Again, the particles are illuminated with a laser beam and the scattered light detected and used to calculate the electrophoretic mobility based on the frequency shift of the scattered light, comparing with a reference laser beam. The zeta potential is finally derived using Henry's equation (eq. 3.5).⁵⁴

$$U_E = \frac{2 \varepsilon z F(k a)}{3 \eta}$$

Equation 3.5 Henry's equation

Where, U_E is the electrophoretic mobility, ε is the dielectric constant, z is the zeta potential, $F(k a)$ is the Henry's function, and η is the viscosity.

The zeta potential measurements were performed using a Nano zetasizer at Laval University.

3.4.9 Elemental analysis

Neutron Activation Analysis (NAA) was used for absolute quantification of Au and Mn in Au-Mn NPs. For NAA, the sample is irradiated with neutrons in a nuclear reactor to activate certain elements in their radioactive isotopes. The different elements are identified and quantified during the decay of the isotopes, as each one has a characteristic half-life and emits γ -radiation at specific energies. The quantification of the elements is based on the intensity of γ -rays emitted.¹³⁹

To confirm the content of Au and Mn in the Au NPs@PEG-Mn²⁺ or Au NPs@PEG for different experiments, the samples were digested in aqua regia and 30% H₂O₂ above 100 °C to completely dissolve both the inorganic and the organic components. Afterwards, the samples were analyzed either by inductively coupled plasma mass spectrometry (ICP-MS) or microwave plasma-atomic emission spectrometer (MP-AES). In the first method, the sample is ionized using inductively coupled plasma and a mass spectrometer is used to separate and quantify the different metals present in the sample. In the second method, the elements in the sample are excited through microwave induced plasma and the metals are identified based on atomic emission spectroscopy.¹⁴⁰

NAA was performed at École Polytechnique de Montreal by Dr. Cornelia Chilian, using a SLOWPOKE nuclear reactor. The ICP-MS as well as the MP-AES analysis were performed by Dr. Vicky Doddier at Laval University, using a Perkin Elmer Elan 6000 and an Agilent 4200 Microwave Plasma-Atomic Emission Spectrometer, respectively.

3.4.10 CT imaging studies

CT imaging was performed to characterize the contrast enhancement provided by Au NPs@PEG-Mn²⁺ *in vitro* at different concentrations, and *in vivo* using the PC3 chick embryo's chorioallantoic membrane (CAM) tumour model. The chick embryo's CAM system was used for *in vivo* dual imaging studies because (1) tumour induction in the CAM is faster than in immunodeficient mice; (2) the chick embryos are cheaper, and (3) easier to manipulate, especially for repetitive imaging studies.¹⁴¹⁻¹⁴² At last, CT was also used to performed DCE studies using mouse models.

As described in the introduction, the CT images are constructed based on X-ray attenuation maps created due to differential X-ray absorption by the body tissues, bones and air-filled structures. In more detail, the interaction of X-rays with matter can occur through three different processes: (1) photoelectric absorption, (2) Compton scattering, and (3) Rayleigh scattering. The probability of each process to happen is correlated with the composition of the tissues and the energy of the X-ray photons.⁸⁴ For CT/micro-CT image acquisition, the energy of the X-ray photons can vary from 25 to 140 keV. In this energy range, the photoelectric absorption and the Compton scattering are the predominant processes.^{82, 84, 101} Hence, these phenomena are responsible for the attenuation of the X-rays by biological tissues, which is the base of CT imaging. For image acquisition, an X-ray source rotates around a body section, and a detector located on the opposite side of the source collects the transmitted X-ray photons at different angles. While crossing the different tissues, some photons of the incident beam will be completely absorbed (by photoelectric absorption), whereas others will be scattered losing a fraction of their energy (by Compton scattering), and others will cross the body without interaction with the tissues. Based on the intensity of the initial and transmitted X-ray beams, numerical analysis are used to calculate the linear attenuation coefficient (μ) for each voxel and to generate images displaying the X-ray attenuation by the different tissues.⁸⁴ The linear attenuation coefficient, which is defined as the fraction of photons of a specific energy attenuated per unit of thickness of material, is tissue specific because of unique elemental composition and density. The differential X-ray attenuation is represented in the reconstructed image in Hounsfield units, which are obtained by normalizing the total μ measured in each voxel to the μ of water.^{87, 89}

The CT studies were performed using a eXplore Locus 80 preclinical CT from GE Healthcare Technologies at CR-CHUQ. The image acquisition and animal handling were

performed by Dr. Jean Lagueux (further experimental details are provided in article 2). The PC3 CAM tumour models used in the imaging studies were developed by Ms. Marie-France Côté also at CR-CHUQ (the experimental details are described in article 2).

3.4.11 MRI imaging studies

MRI was also performed to characterize the contrast enhancement provided by Au NPs@PEG-Mn²⁺ *in vitro* and *in vivo*.

The images in MRI are generated based on the electromagnetic signals emitted by the ¹H protons present in body tissues. In more detail, the rotational axes of the ¹H spins are randomly oriented, unless they are submitted to a strong external magnetic field (B_0) (for clinical applications, the field strength can vary from 0.5 T to 3 T). In this situation, the spins align with the direction of B_0 following a parallel or anti-parallel orientation. At equilibrium, there are slightly more protons aligned parallel to B_0 , this orientation also corresponds to a lower energy level. (Figure 3.6).^{80, 84}

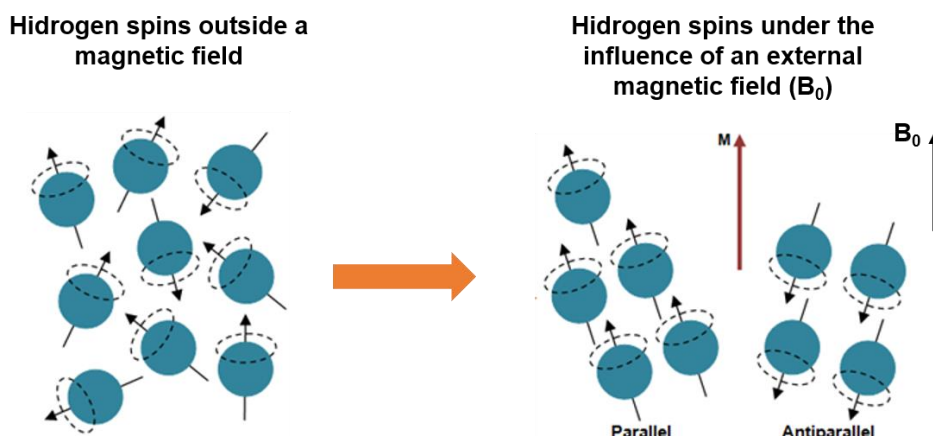


Figure 3.6 Illustration of the influence of an external magnetic field (B_0) on the rotational axes of the ¹H protons.

Also, under the influence of B_0 , the ¹H protons start to precess and the rate of the precession depends on the strength of B_0 and is called the Larmor frequency. Once in precession, all the individual magnetic moments of the ¹H protons add up, and a resulting macroscopic magnetization vector (\vec{M}_z) in the direction of B_0 can be defined.⁸⁰ In order to place \vec{M}_z

perpendicularly to B_0 , a radiofrequency (RF) pulse (at Larmor frequency) is emitted from an antenna to provide further energy to the system (Figure 3.7 (A)). As a consequence, (1) some spins shift to a higher energy level (anti-parallel to B_0), and (2) all the protons start to precess in phase.⁸⁰ Hence, \vec{M}_z becomes perpendicular to B_0 , and can be denominated as the transversal magnetization vector (\vec{M}_{xy}) (Figure 3.7 (B)). The precession of this vector around the z-axis creates a constantly oscillating magnetic field, which can be detected by a receiver coil and processed by computers to produce the MR image.⁸⁴

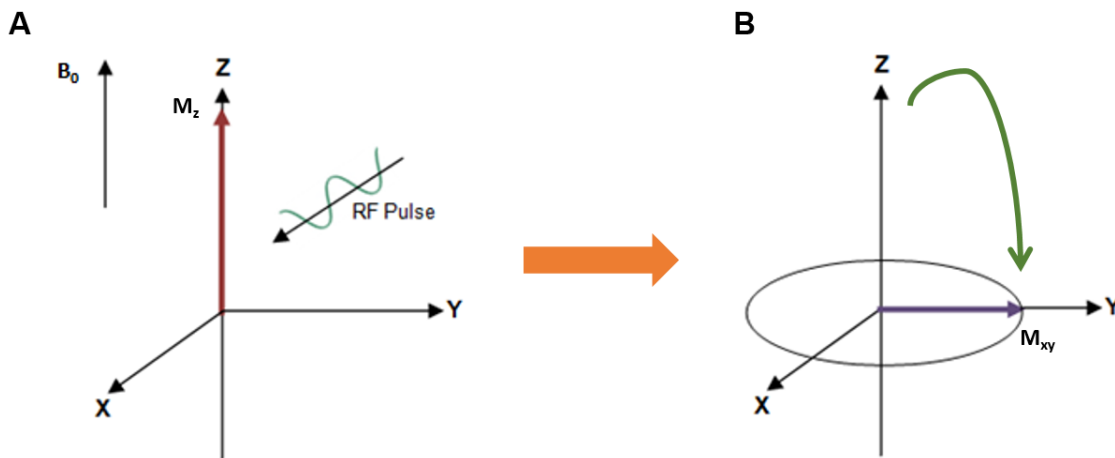


Figure 3.7 Illustration of the effect of energy transfer from the radiofrequency (RF) pulse to the macroscopic magnetization vector (\vec{M}). The energy delivered by the RF pulse to the ^1H protons changes the position of the rotational axis to anti-parallel to B_0 , and induces precession in phase (A). Consequently, a magnetization vector perpendicular to B_0 is created (purple vector) (B).

The image contrast in MRI depends on the differentiation of how fast the ^1H protons from different tissues return to their initial energy level. In order to perceive this difference, the RF pulse is turned off to allow proton spin relaxation. The relaxation is caused by (1) longitudinal or spin-lattice relaxation, which happens due to ^1H proton energy transfer to the environment, and (2) transversal or spin-spin relaxation, which is caused by B_0 inhomogeneity and the influence of the magnetic field of each ^1H proton on its neighbors. The relaxation process ultimately leads to the decrease of the transversal magnetization and simultaneous recovery of the longitudinal magnetization (figure 3.8). The relaxation process is described by two time constants, the longitudinal relaxation time (T_1), which is the time required for the longitudinal magnetization to

recover up to 63% of its initial magnitude; and the transversal relaxation time (T_2), which is the time necessary for the transversal magnetization to drop 37% of the initial value.⁸⁰

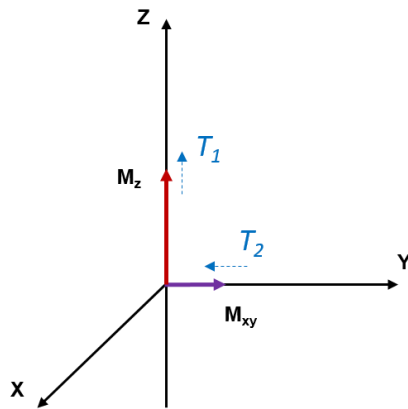


Figure 3.8 Illustration of the loss of transversal magnetization (purple vector) and simultaneous recovery of the longitudinal magnetization or macroscopic magnetization vector (M) (red vector), and the time constants (T_1 and T_2) that characterize each process.

The remarkable tissue contrast provided in the MR images results from differences in T_1 , T_2 , and ^1H proton density (PD) which are unique for each tissue. These differences can be created and magnified using diverse RF pulse sequences and by averaging of the emitted signal from a selected tissue volume. This allows generation of images with different types of contrast, the most basic examples are the T_1 -, T_2 - or PD -weighted images.⁸³

In the present work, only T_1 -weighted images were acquired because paramagnetic CAs are better observed in these conditions.⁸¹ In fact, T_2 -weighted images are also recommended for the differential diagnosis of breast and prostate cancers. These images provide detailed anatomic information of the lesions, and the signal intensity pattern is used to characterize the lesion. However, the data provided by T_2 -weighted images is not enough for unambiguous determination of cancer sub-type, thus functional techniques, such as DCE studies are also necessary to improve both the sensitivity and specificity of MRI.^{6, 8}

As for the CT studies, the animal handling and MR image acquisitions were performed by Dr. Jean Lagueux at CR-CHUQ using a 1.0 T MRI pre-clinical scanner (M2M) from Aspect Imaging (the experimental details and acquisition sequence parameters are described in article 2).

3.4.12 ^1H NMR

Proton NMR spectroscopy was used to measure the relaxation times T_1 and T_2 of the Au NPs@PEG-Mn²⁺. Similar to the method principle used for MR imaging (explained in the previous section, in this method an aqueous sample containing the CA is placed under the influence of an external magnetic field (in this work, equivalent to the ones used for clinical imaging: 1.4 T, 60 MHz). Afterwards, the water molecules in the sample are excited by a series of RF pulses at the Larmor frequency. The RF pulses are emitted in specific pulse sequences in order to measure T_1 or T_2 . When the RF pulses are switched off the equipment can measure the relaxation times and these values are provided.⁸³

The efficiency of CAs in reducing the relaxation times (T_1 and T_2) of nearby ^1H protons is assessed by their relaxivities (r_1 and r_2), which indicate how much a unit concentration (mM) of the metal ions can increase the relaxation rates (R_1 and R_2). The relaxation rates are the inverse of the relaxation times ($1/ T_1$ and $1/ T_2$).⁷⁹ Hence, after measuring the relaxation times for different concentrations of Mn²⁺, the relaxivities were extracted from the slope of a linear regression obtained by plotting the relaxation rates in function of the Mn concentration of each Au NPs@PEG-Mn²⁺ sample. At last, the relaxivity ratio (r_2/r_1) can be used to classify the MRI CAs as “positive” or “negative”. The first type of CAs have a ratio close to 1 and induce an increase of the signal, whereas the second usually show ratios higher than 5 and decreases the signal.⁷⁹

The ^1H NMR measurements were performed using a time-domain NMR (Bruker Minispec 60 mq) at CR-CHUQ.

3.4.13 Cell toxicity Assay

To assess cell viability after exposure to increasing concentrations of Au NPs@PEG-Mn²⁺ or Au NPs@PEG, the resazurin (Alamar blue) assay was performed. Using this method, cytotoxicity was assessed based on the reduction of resazurin (a non-fluorescent dye) into a pink fluorescent dye, resorufin. Resazurin reduction is suggested to occur in the cell medium, due to oxygen consumption during cell metabolism, or intracellularly because of enzyme reduction.⁵⁵ Independently of the reduction process, low production of resorufin, comparing with control cells, indicates that the cell metabolism and proliferation is impaired.¹⁴³

The resazurin assay was performed instead of cell membrane leakage assays, such as the trypan blue or the propidium iodine assays, because it allows to detect dying cells early in the apoptosis process (i.e. when the mitochondrial activity is already compromised, but before the cell membrane degrades).¹⁴⁴ The resazurin assay was also preferred to the MTT (3-(4,5-dimethylthiazol-2-yl)-2,5-diphenyl tetrazolium bromide) assay, which is as well a mitochondrial activity assay, because it offers higher sensitivity (as the measurement is based on fluorescence), and it is less affected by the presence of Au NPs, which strongly absorb light from 510-530 nm.⁵⁵

¹⁴⁵

The cell culture and cell handling necessary to perform the assay were performed by Ms. Marie-France Côté at CR-CHUQ (detailed description of methodology is provided in article 2).

4. RESULTS AND DISCUSSION

4.1 Au-Gd nanocomposites synthetized by PLAL

Considering the advantages of Gd^{3+} as a CA for MRI, the first step of this work was to attempt the synthesis of Au-Gd NPs using PLAL. For this, pulsed laser ablation of $\text{Au}_{50}\text{Gd}_{50}$ target was performed at several pH (7-11) and with different laser fluences. The effect of fluence on the target ablation was studied at pH 11, as this concentration of NaOH provided the higher ablation rate for a fixed fluence.

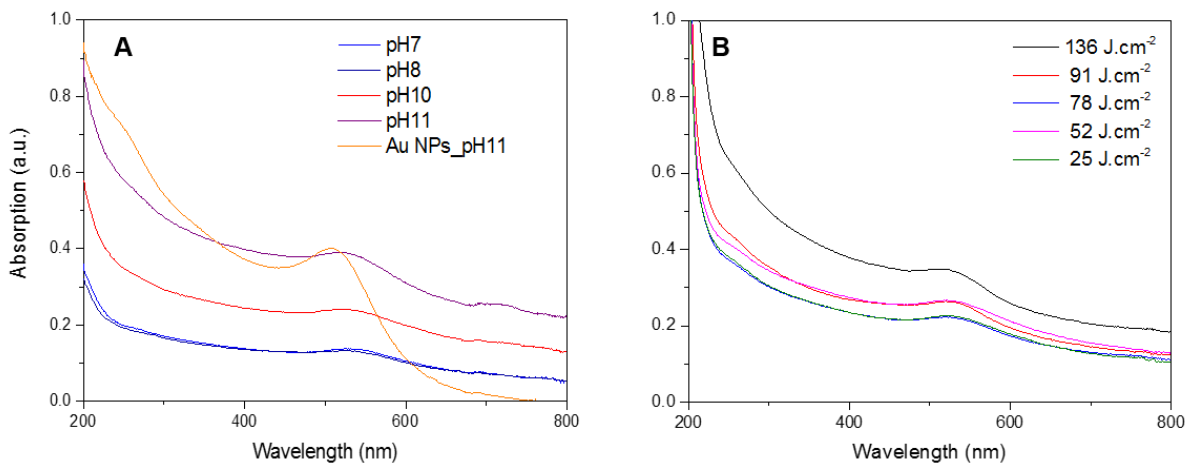


Figure 4.1 UV-visible absorption spectra of Au-Gd colloids obtained after pulsed laser ablation of Au-Gd target. (A) The target was immersed in solutions with different pH value and the spectra of the final colloids was compared to the spectrum of Au NPs produced at pH 11. (B) The target was ablated with different fluences at pH 11.

The colloids obtained after the ablation of $\text{Au}_{50}\text{Gd}_{50}$ target showed a similar absorption spectrum for all the pH and fluence tested (figure 4.1). However the spectra were different from the one characteristic of pure Au NPs (figure 4.1 (A)), which suggested the formation of a composite structure.

The crystalline structure and elemental composition of the Au-Gd colloids synthetized at different pH (figure 4.2 (A)) and fluence (figure 4.2 (B)) were also analyzed by XRD.

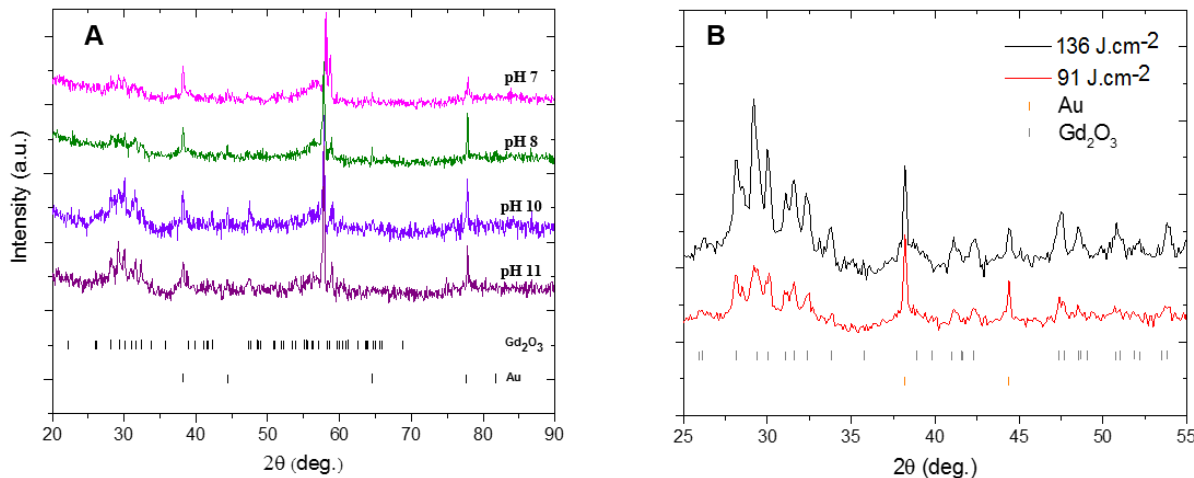


Figure 4.2 X-ray diffractograms of Au-Gd colloids obtained by pulsed laser ablation of Au-Gd target in solutions at different pH value (A) or fluence (B).

All the samples revealed the presence of Au and Gd₂O₃, as both the characteristic cubic crystal structure of Au (lattice parameter of 4.078 Å, JCPDS 03-065-2870) and the monoclinic phase of Gd₂O₃ (lattice constants a=14.095 Å, b=3.576 Å and c=8.769 Å, JCPDS 00-042-1465) were identified. There was no shift in the lattice parameter of both elements, suggesting that Au-Gd alloy was not formed.

The stability of the obtained colloids was limited since all the samples precipitated one hour after the synthesis. Another strategy to improve the colloidal stability of PLAL synthesized NPs is to add surfactants or polymers to the solution during the ablation. These molecules can adsorb on the surface of the NPs during nuclei growth through electrostatic interactions and hydrogen bonding and improve the stability of the colloids.^{33, 113} As described earlier, PEG is commonly used to improve colloidal stability of NPs, especially for *in vivo* applications. Therefore, an aqueous solution with 0.1 g L⁻¹ of PEG (3 kDa) was used during the ablation of Au₅₀Gd₅₀ target. The new colloids had a UV-vis spectrum similar to the ones shown on (Figure 4.1 (A)), however the particles stayed in suspension up to one day instead of precipitating almost immediately (one hour) after ablation.

This sample was observed by TEM to investigate the structure of the Au-Gd₂O₃ composite formed by PLAL, and the elemental composition was analyzed by EDS. On figure 4.3 (A) it was

observed that the Au-Gd₂O₃ colloid was composed by very small Au NPs connected by a network of Gd₂O₃ (figure 4.3 (B) and (C)).

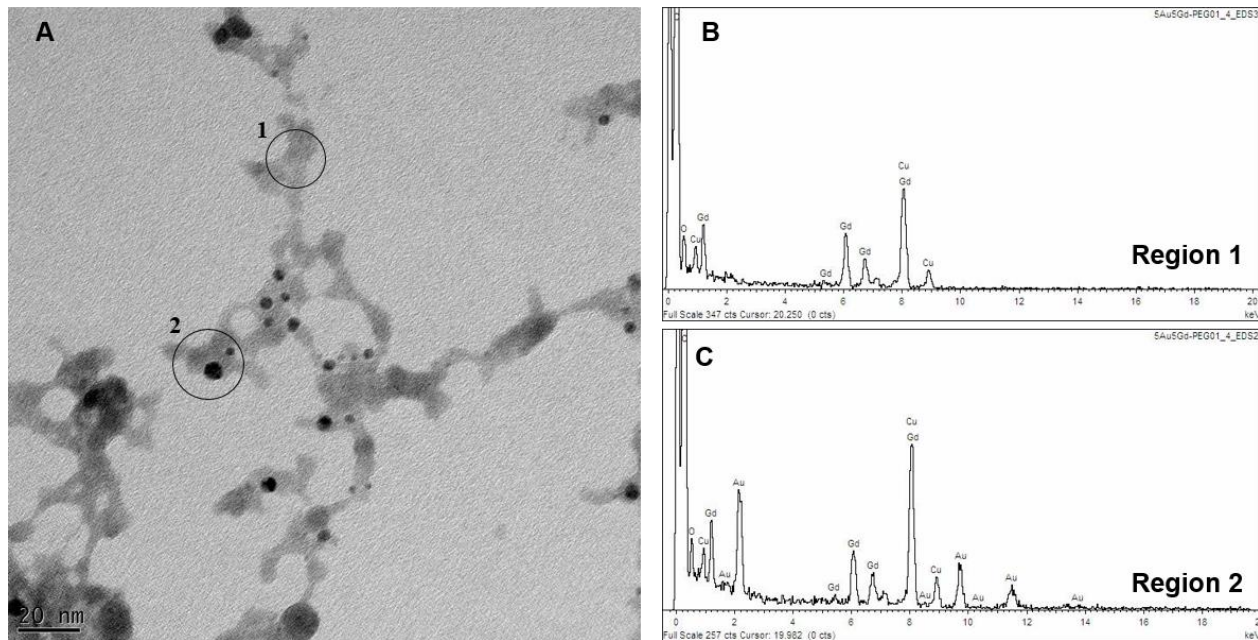


Figure 4.3 TEM image of Au-Gd₂O₃ colloid produced by pulsed laser ablation of Au-Gd target in a solution containing 0.1 g L⁻¹ of PEG (scale bar: 20 nm) (A), EDS spectrum acquired on region 1 of TEM image, demonstrating the presence of only Gd (B), and EDS spectrum obtained from region 2 of the same image, evidencing spectra lines of both Au and Gd (C).

Tarasenko and colleagues characterized Gd₂O₃ NPs obtained after the ablation of a Gd metal plate in distilled water with a 1064 nm wavelength laser.⁵⁶ They produced well dispersed Gd₂O₃ NPs with average diameters ranging from 10 to 12 nm. Therefore, the formation of the Gd₂O₃ network observed in the present work was probably related to the strong self-absorption of energy from the UV laser light by the Gd₂O₃ NPs formed or ejected from the target during the laser ablation.⁵⁷ Unfortunately, the structure of the obtained Au-Gd₂O₃ colloid was not suitable for *in vivo* application. Therefore PLAL synthesis using a Au-Mn metal target was investigated.

4.2 Au-Mn NPs synthetized by PLAL

The ablation of the $\text{Au}_{64}\text{Mn}_{36}$ target was performed in aqueous solutions with various pH (7 – 11). On figure 4.4 (A), which displays the UV-visible spectra of the colloids produced at different pHs, it was observed that the shape of the spectra slightly changed for increasing concentrations of NaOH. Thus, contrary to what was observed in the Au-Gd₂O₃ system, it was concluded that the pH had an influence in the structure formed. In addition, it was observed that this parameter also affect the stability of the colloids. Thus, colloids obtained at pH 7 and 8 precipitated few hours after the ablation, while the particles obtained at pH 9 and 10 where stable for several days and the colloids produced using pH 11 could be stable for months without the addition of any stabilizing agent. Because colloidal stability is a requirement for the production of NP-based CAs, the colloid produced at pH 11 was selected for more detailed characterization.

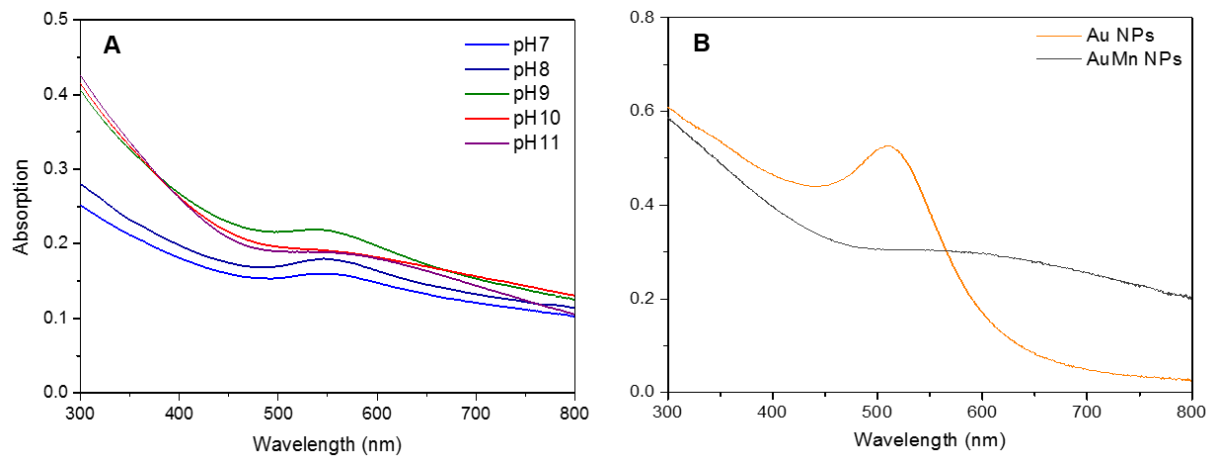


Figure 4.4 UV-visible absorption spectra of Au-Mn NPs obtained after pulsed laser ablation of Au-Mn target in solutions at different pH values (A). Comparison of the UV-visible absorption spectrum of Au-Mn NPs produced in a solution at pH 11 with the spectrum of Au NPs produced after the ablation of Au target at pH 11 (B).

On figure 4.4 (B) the spectrum of the Au-Mn NPs synthesized at pH 11 was compared with the one of pure Au NPs prepared at the same pH. The damping of the SPR band indicated, as in the Au-Gd₂O₃ system, that a composite structure was formed. The strong light absorption of pure Au NPs, which creates the SPR band, happens due to collective oscillation of the NP free electrons when excited at resonant wavelengths. The resonant frequency can vary with the size, shape, composition and aggregation state of the NPs, as well as with the dielectric constant of

the surrounding medium.⁵⁸⁻⁵⁹ In addition, damping of the SPR band can be a consequence of alloy formation, or could be due to grafting of electron acceptor molecules on the surface of the Au NPs.⁶⁰⁻⁶¹ Because the colloid obtained after the ablation of the Au-Mn target presented a significant red-shift and fading of the SPR band, it was concluded that a core-shell or alloyed structures could have been formed. The presence of heterodimer NPs was ruled out as this structure would allow the observation of the SPR band.¹⁴⁶

To determine the structure of the Au-Mn NPs, XRD and EELS mapping were performed. The X-ray diffraction pattern displayed on figure 4.5 (A) was characteristic of a cubic crystal structure with a lattice parameter equal to 4.0786 Å, which was attributed to Au. Therefore, the NPs were not composed by a Au-Mn alloy.

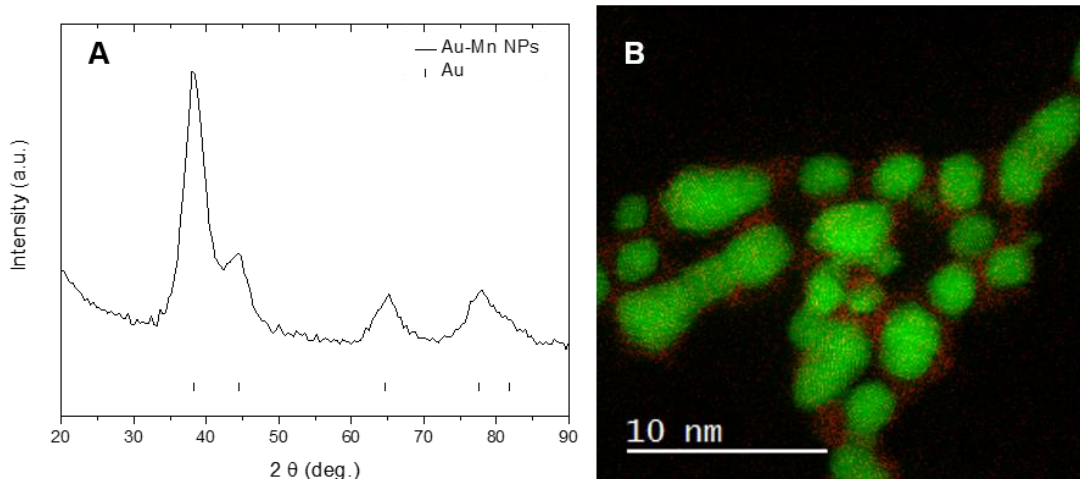


Figure 4.5 X-ray diffractogram of Au-Mn NPs obtained after the ablation of Au-Mn target at pH 11 (A). EELS mapping of Au-Mn NPs produced under the same conditions (B). In this image, manganese is marked in red, whereas Au is represented in green.

EELS mapping revealed a core-shell structure, in which a Au core (figure 4.5 (B), indicated in green) is partially or completely surrounded by a very thin Mn layer (figure 4.5 (B), indicated in red).

HAADF HR-STEM observations confirmed the formation of a core-shell structure, and permitted to differentiate amorphous areas (figure 4.6 (A), indicated by stars) as well as crystalline regions (figure 4.6 (B), indicated by arrows) in the very thin (0.3 to 1.3 nm) Mn layer. In agreement with the diffractogram, the Au core showed a highly crystalline structure (figure 4.6 (B)).

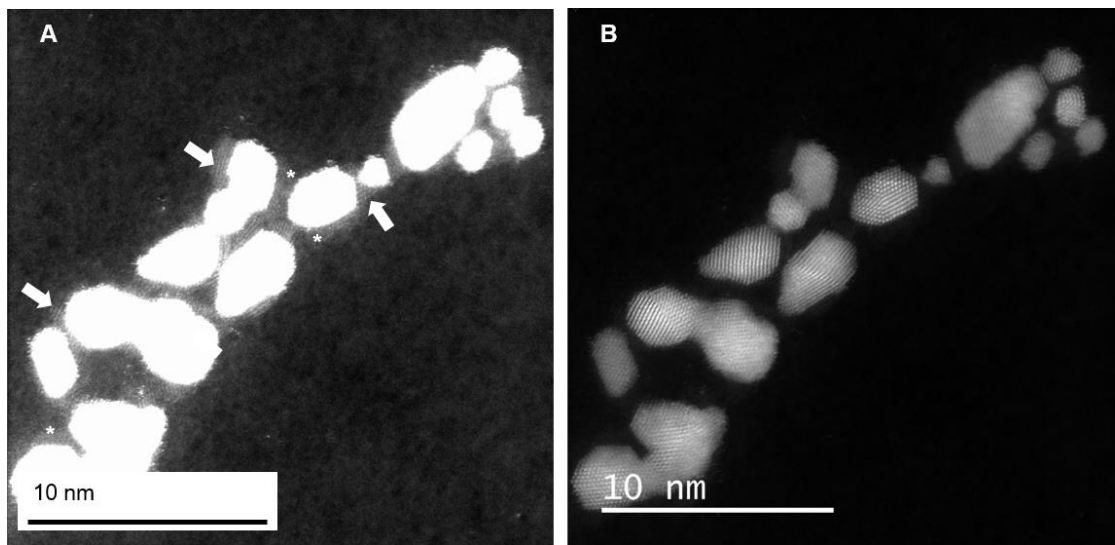


Figure 4.6 HAADF HR-STEM micrographs evidencing the manganese shell (A) surrounding the Au core (B). On image (A), the arrows point to crystalline regions of the manganese layer, while the stars indicate amorphous areas.

TEM images did not show the surrounding Mn layer (figure 4.7). However, they were useful to measure the average size of the Au core, which was approximately 4.8 nm.

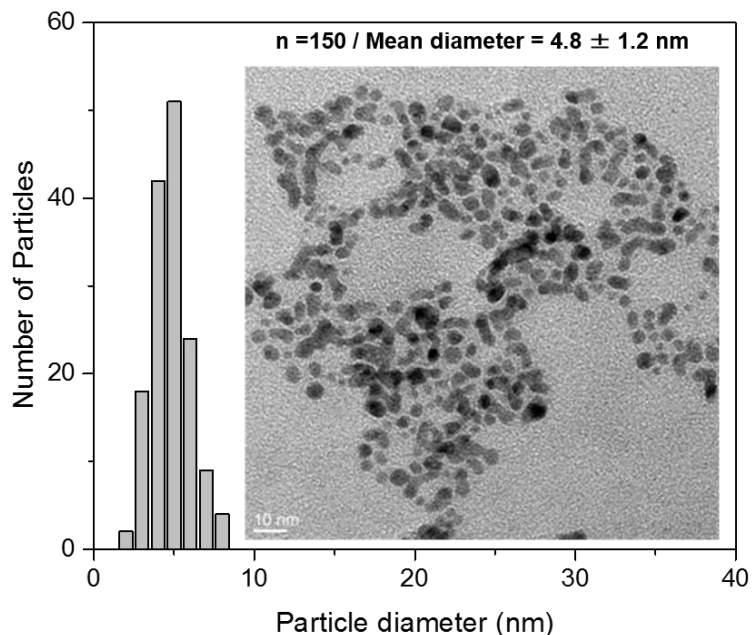


Figure 4.7 TEM image and size distribution of the Au core in the Au-Mn NPs obtained after the ablation of Au-Mn target in a solution at pH 11 (scale bar: 10 nm).

Elemental analysis were performed by XPS, EDS and NAA to determine the relative atomic percentage of Au and Mn. The results of these measurements, displayed in table 4.1, demonstrated that before washing the NPs with de-ionized water, the relative Mn content varied between 27 to 29%. The samples were washed to determine if there was solvated Mn ions or if all the Mn content was in the solid form and therefore associated to the Au core. Even after washing, the Au-Mn NPs retained a relative atomic composition of Mn varying from 26% to 29%. Hence, it was concluded that the Mn content in the sample was in the form of a manganese oxide.

Table 4.1 Relative percentage of Mn and Au atoms on Au-Mn NPs. The relative percentages were calculated based on elemental quantification obtained by XPS, EDS and NAA.

Sample	Relative Mn % ($100 \cdot \text{Mn}/(\text{Au}+\text{Mn})$)		
	XPS	EDS (TEM)	NAA
Au-Mn NPs before washing	28.6	$27.3 \pm 1.4^{\text{a}}$	29
Au-Mn NPs after washing	26.3	$27.1 \pm 7.1^{\text{b}}$	29.3

^a average of 2 measurements

^b average of 14 measurements

As described previously, Mn^{2+} is an interesting CA for MRI due to the presence of five unpaired electrons in the 3d orbital. However, as the valence state of Mn increases, less unpaired electrons are available, which can decrease the efficiency of Mn in its ability to affect the relaxation rates of water molecules. Therefore, it is important to determine the oxidation state of the Mn layer in order to assess the potential of this material to be used as a MRI CA.

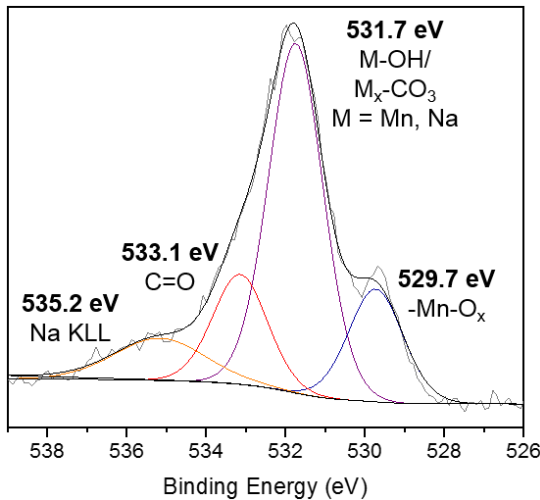


Figure 4.8 High resolution XPS spectrum of O 1s core level from Au-Mn NPs.

XPS analysis of Au-Mn NPs confirmed the presence of manganese oxide on the surface of the NPs, as shown by the presence of a photo-peak centered at 529.7 eV. In addition, another peak centered at 531.7 suggested the presence of sodium or manganese carbonate, and hydroxide species (figure 4.8). The most commonly used strategy to determine the oxidation state of Mn by XPS is to use the Mn 3s core level region.¹⁴⁷⁻¹⁴⁸ However, the Au 4f peaks overlap with this region, making it impossible to use this information. Another option is to investigate the Mn 2p_{3/2} peak position and the presence of satellite structures.¹⁴⁸⁻¹⁴⁹ Nonetheless, the Mn 2p_{3/2} core level peak is also very close to the Au 4p_{1/2} peak, which affected the observation of satellite structures and accurate determination of the Mn 2p_{3/2} peak position.

Thus, XAFS analysis was performed to determine the oxidation state of Mn. The fitting of the Mn K-edge EXAFS data revealed a Mn-O and Mn-Mn bond distance of 1.90 Å and 2.92 Å, respectively. Comparison of these values with the ones obtained for manganese oxide references (e.g. MnO, Mn₂O₃, MnO₂) suggested that the manganese oxide layer had a structure most identical to MnO₂. In addition, qualitative evaluation of the Mn K-edge XANES of Au-Mn NPs and the reference manganese oxides demonstrated a chemical similarity with the Mn₂O₃ and MnO₂ references compounds, especially regarding the absorption edge energy position and the near-edge structure features (XANES and EXAFS data as well as fitting results can be found in Article 1). Preliminary relaxometric analysis of the Au-Mn NPs demonstrated that the NPs did not affect significantly the relaxation times of water molecules, which was in agreement with a higher

oxidation state of the Mn layer as determined by XAFS analysis. Therefore, another strategy was explored to produce a dual imaging CA based on NPs synthetized by PLAL.

4.3 Au NPs synthetized by PLAL

Another approach to synthetize a dual imaging CA based on NPs synthetized by PLAL is to functionalize pure Au NPs with chelates of a paramagnetic ion. Such design can take advantage of the Au NPs surface purity, which can minimize potential toxicity related with chemical contaminants, and permits higher functionalization efficiency.³⁷ In addition, all the functionalization procedures could be carried in aqueous solutions, given that the particles and surface ligands are soluble and stable in these conditions.

As mentioned in section 1.3, the ionic content of the ablation solution can significantly improve the colloidal stability, the size and the polydispersity of Au NPs produced by PLAL.^{33, 45-46} A small diameter and narrow size distribution are desirable for *in vivo* applications of NPs as CAs. These properties are important because a small HD (up to 6 nm) allows elimination of the NPs mostly through the kidneys, and the low polydispersity is necessary for all the NPs to have similar pharmacokinetics.^{30, 32, 93} Therefore, we investigated the concentration of OH⁻ and Cl⁻ that provided the best compromise between colloidal stability, small size and low polydispersity. For this, a Au₁₀₀ metal target was ablated with a 248 nm ns-laser in aqueous solutions at several pH (4-12), adjusted with NaOH or HCl. The UV-Visible spectra of the different colloids was measured and the size, colloidal stability as well as polydispersity were assessed indirectly based on the SPR band position (figure 4.9 (A)) and on the PPI (figure 4.9 (B)). The position of the SPR band of the colloid produced in an aqueous solution at pH 11 suggested that these NPs had the smallest diameter (figure 4.9 (A), dashed circle). Regarding the PPI data, this colloid did not show the highest colloidal stability/ lowest polydispersity (figure 4.9 (B), dashed circle), however the PPI obtained was still considered very good.⁴⁵⁻⁴⁶ Therefore, this colloid was also observed by TEM (figure 4.10 (A)), which confirmed the existence of a small average size (6.6 nm) and relatively narrow size distribution (± 1.6 nm).

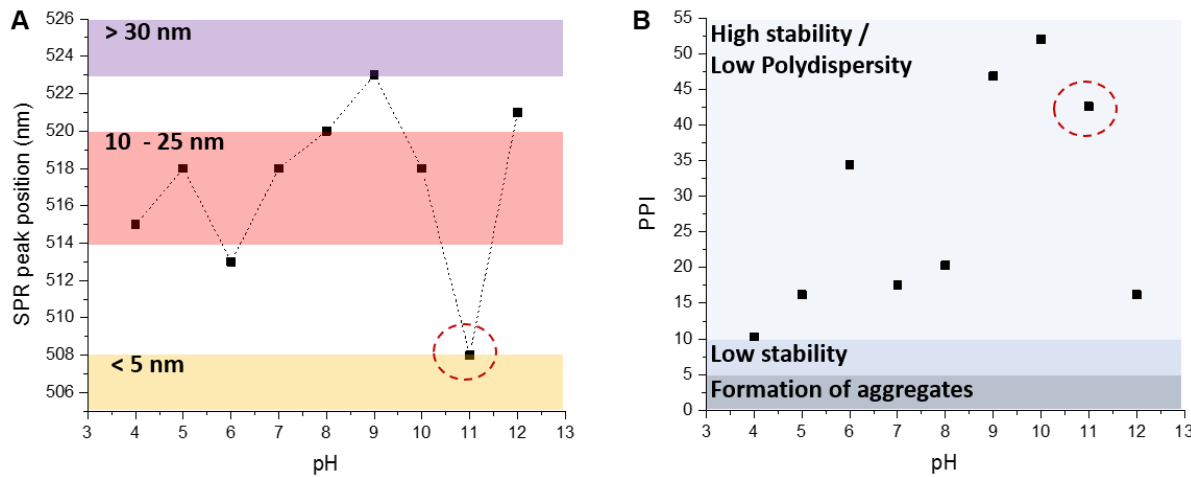


Figure 4.9 SPR peak position of Au NPs in function of the ablation solution's pH (synthesis with a 248 nm ns-laser). The estimated Au NP diameters displayed in the colored regions were obtained from reference ¹⁵⁰ (A). PPI value in function of the ablation solution's pH. The relation between the PPI value and the degree of stability / polydispersity of the Au NPs sample was obtained from references ⁴⁵⁻⁴⁶.

The Au NPs synthetized by PLAL are electrostatically stabilized by Au-OH and Au-O⁻ species formed during the ablation.^{33, 63-64} Sylvestre and co-workers were the first to demonstrate that the size of Au NPs could be controlled by increasing the hydroxyl concentration in the ablation solution.⁶³ It has been proposed that an alkaline medium promotes deprotonation of the hydroxide species adsorbed on the surface of Au NPs, which increases the negative net charge of the particles through the formation of Au-O⁻ groups. The strong charge density at the surface of Au NPs increases the repulsion between the NPs, which improves the colloidal stability and minimizes nuclei coalescence.^{33, 64}

Another factor to consider for the application of NPs as CAs is the production rate of the material. This is especially important for CT, in which relatively high concentrations of Au NPs have to be used to produce significant contrast enhancement.³² Despite the good results obtained using a UV ns-laser, the production efficiency with this set-up was limited due to self-absorption of the laser energy by the newly formed Au NPs, which strongly absorb in the UV region of light spectrum.⁶⁶ This phenomena decreases progressively the laser energy available to ablate the target as the concentration of Au NPs increases in the solution.^{57, 130} Several authors have demonstrated that the production of Au NPs can be increased by using infra-red (IR) wavelength lasers, as Au NPs have a weaker light absorption in this regime.³³ Therefore, in order to produce the amounts of Au NPs necessary for *in vivo* imaging studies, a 1064 nm ns-laser was used

together with a custom made ablation chamber.¹³⁴ These Au NPs were produced using pH 11 due to the promising results obtained in the previous experiments.

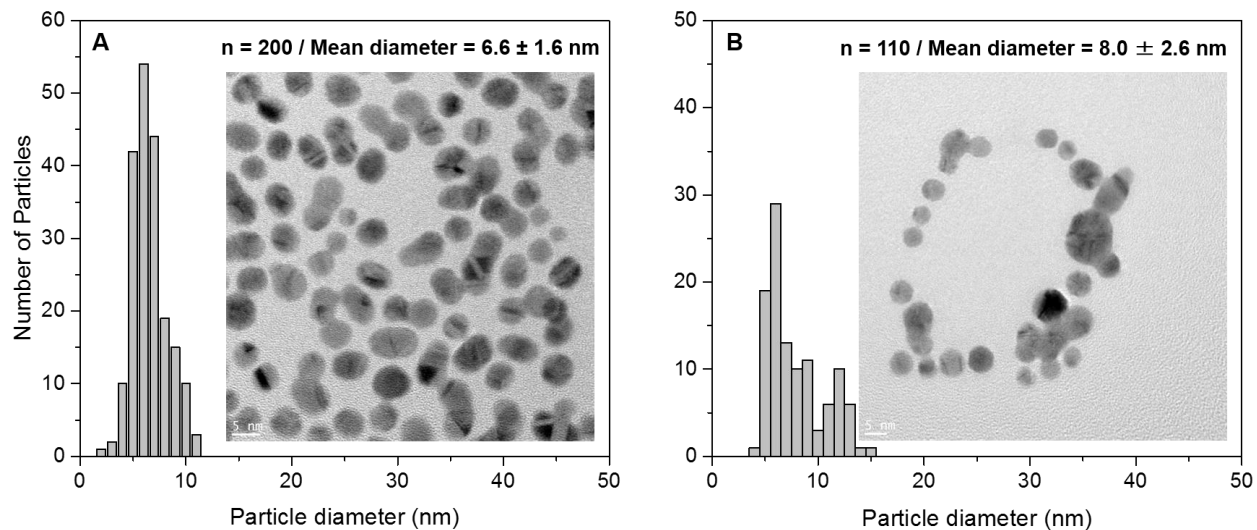


Figure 4.10 TEM image and respective size distribution of Au NPs produced by pulsed laser ablation of a Au target immersed in a solution at pH 11, using a 248 nm (A) and 1064 nm (B) ns-lasers (scale bar: 5 nm).

A TEM image and size distribution of the Au NPs produced using a IR ns-laser are shown on figure 4.10 (B). Both the size (8.0 nm) and standard deviation (± 2.6 nm) were slightly higher than the ones observed using a 248 nm ns-laser (figure 4.10 (A)). This result was expected because the decreased light absorption by Au NPs in the IR regime also minimized NPs' fragmentation by the incoming laser pulses during the ablation procedure.⁶⁶ Nevertheless, the colloidal stability and the size are still suitable for biomedical applications of these NPs.

4.4 Functionalization of Au NPs produced by PLAL with Mn²⁺-chelates

The first step in the production of multimodal CAs was to coat the PLAL-synthetized Au NPs with PEG. This coating provides steric stabilization, which is important for biomedical applications.¹¹⁶ Subsequently, the PEGylated Au NPs were functionalized with DMSA-DTPA molecules and Mn²⁺ ions, as detailed in the experimental section.

A comprehensive characterization of the NPs at the various stages of the functionalization process was performed. Figure 4.11 (A) displayed the UV-visible spectra of the Au NPs at different stages of the functionalization procedure. The observation of a slight shift of the SPR band position (2-3 nm) at each step (shown in more detail on figure 4.11 (B)), together with minimal light absorption at longer wavelengths, led to the conclusion that the samples kept their colloidal stability during the complete process and that the surface was modified during each step.

In agreement, DLS measurements demonstrated relatively narrow peaks throughout the procedure and the absence of major NP aggregates (figure 4.11 (C)). A minimal percentage (1%) of agglomerates (peak centered at 350 nm) was observed in the pure Au NPs, however those do not compromise the application of the NPs as they can be easily removed by centrifugation. In addition, the values demonstrated were intensity-weighted and this measurement mode is highly influenced by the presence of NP aggregates/agglomerates due to the strong light scattering power (proportional to the sixth power of the particle diameter - d⁶) of particles with large diameters.⁵⁴ In fact, number-weighted DLS results demonstrated a monomodal size distribution with an average size of 9.1 nm, which is similar to the 8.0 nm measured by TEM (figure 4.10 (B), section 4.3). Considering the main NPs population, the only significant change in the HD happened after the addition of PEG to the Au NPs (17.5 nm to 40.9 nm). Afterwards, the HD remained relatively constant, independently of further molecular modifications on the Au NPs surface (34.1 nm after the addition of DMSA-DTPA and 36.5 nm after Mn²⁺ chelation). The significant HD change was therefore related with the grafting of PEG molecules on the NP surface, because this polymer has a relatively high molecular weight.

TEM observation of the completely functionalized colloids (Au NPs@PEG-Mn²⁺) demonstrated an average size distribution of 7.2 nm (figure 4.11 (D)), which was similar to the one measure on pure Au NPs (figure 4.10 (B), section 4.3). Therefore, these results demonstrated that the Au NPs did not suffer significant aggregation during the functionalization process. At last, it was observed that after drying, the Au cores were evenly spaced (average inter-particle distance

of approximately 8.6 nm), which was also an indication that the Au NPs had been modified with a PEG layer.⁶⁷

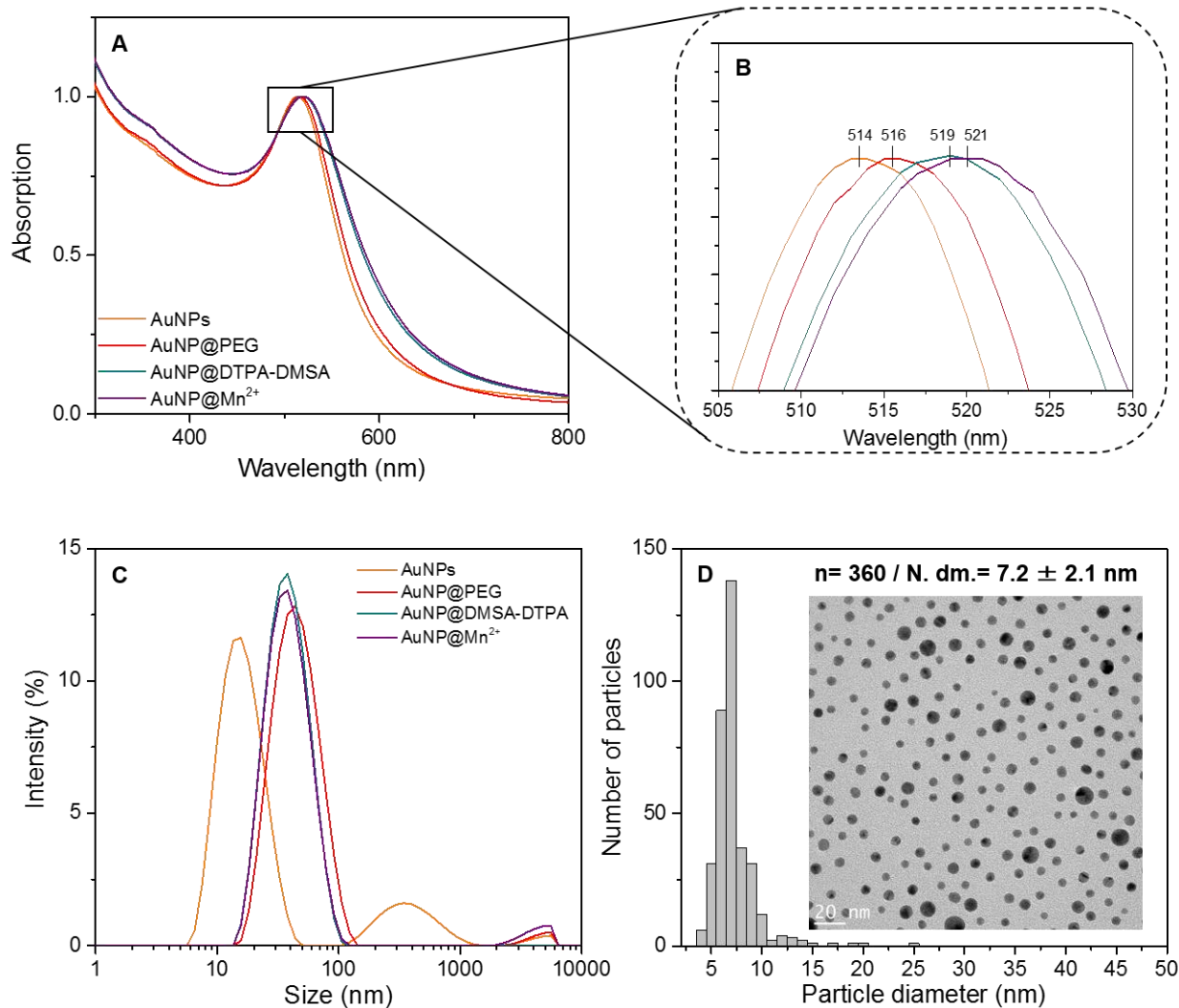


Figure 4.11 UV-visible absorption spectra (A and B) and DLS measurements (C) of the Au NPs produced with the 1064 nm ns-laser, at the end of each functionalization step. TEM image and size distribution of the Au NPs@PEG-Mn²⁺ (scale bar: 20 nm) (D).

The previous studies demonstrated that the surface of the Au NPs suffered modifications during the different steps of the functionalization procedure, and the colloidal stability of the particles was not affected during the process. However, it was necessary to confirm that the

different molecules and ions (e.g. PEG, DMSA-DTPA, Mn^{2+}) were indeed grafted to the surface of the Au NPs. For this, XPS, FTIR, zeta potential and proton NMR analysis were performed.

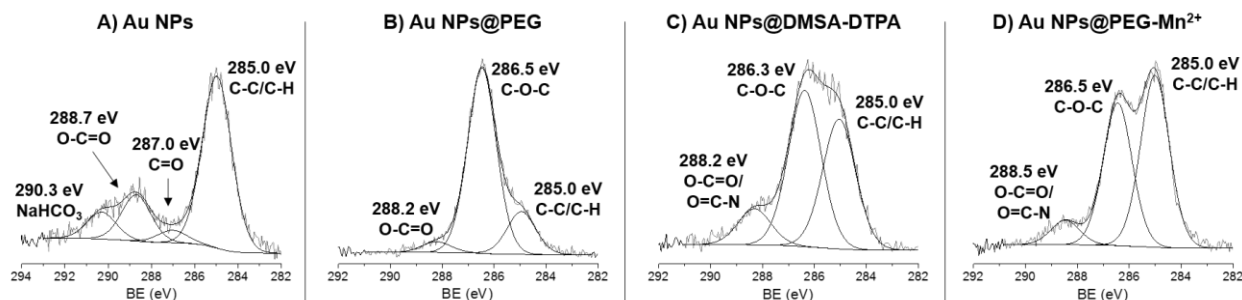


Figure 4.12 High resolution XPS spectra of C 1s core level acquired at the end of each functionalization step.

Deconvolution of the high resolution C 1s spectra clearly evidenced the modification that occurred on the Au NPs surface during the functionalization procedure (figure 4.12). Adventitious carbon contamination was observed at the surface of Au NPs (figure 4.12 (A)), which is mainly characterized by C-C/C-H bonds and a small percentage of carboxyl and carbonyl groups. This is a common consequence of sample exposition to atmospheric air after drying. In addition, carbonate functional groups were observed, originating most probably from sodium carbonate, which is consistent with the use of NaOH during the NPs' synthesis.⁶⁹ After the addition of PEG, sodium carbonate is no longer observed and the strongest XPS signal was attributed to the presence of carbon in a C-O-C bond, which is typical of the presence of PEG (figure 4.12 (B)).⁶⁸ The functionalization with DTPA-DMSA led to an increase of the relative percentage of carboxyl and possible O=C-N groups, which are present in these molecules, and the strong presence of C-O-C bonds was kept (figure 4.12 (C)). The chelation of Mn^{2+} did not modify the molecular composition at the Au NPs' surface (figure 4.12 (D)). However, there was a slight change in the relative percentage of the peaks attributed to O-C=O/O=C-N and C-O-C, which suggested that an excess of DTPA-DMSA was removed during the chelation steps and subsequent dialysis.

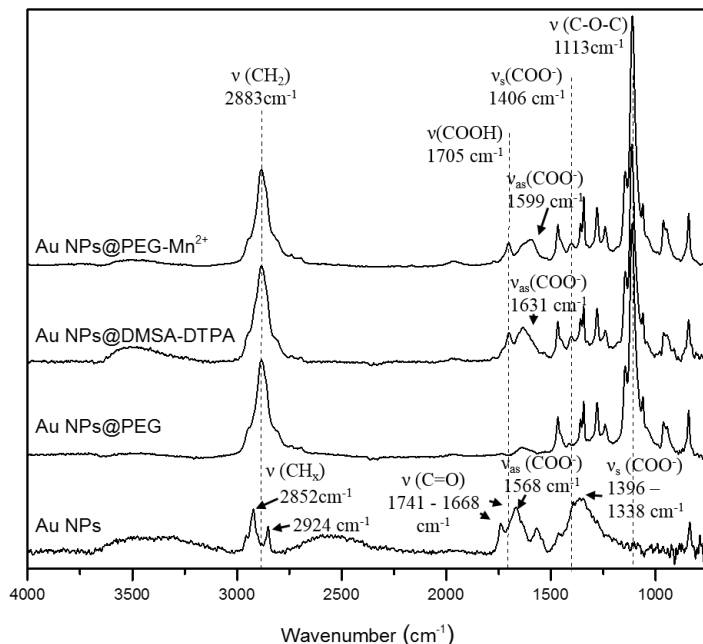


Figure 4.13 ART-FTIR spectra of Au NPs at the different steps of the functionalization procedure.

FTIR analysis confirmed the surface modification observed in the high resolution spectra of C 1s. As expected, the spectrum of pure Au NPs revealed vibration modes related to the presence of ligands containing carbonyl (at 1668 and 1741 cm⁻¹), carboxylate (in the region between 1338 and 1396 cm⁻¹, and at 1568 cm⁻¹) and C-H_x (at 2852 and 2924 cm⁻¹) groups.⁷⁰ Part of the later vibration modes could be attributed to methyl groups, which were likely a consequence of methanol traces, as this solvent was used to clean the crystal. After PEGylation of Au NPs, the main vibration modes observed in the spectrum of this colloid were attributed to the PEG backbone chain (C-O-C band at 1113 cm⁻¹).⁷¹ This result confirmed that most of the carbonate molecules were removed after PEG grafting. The presence of DMSA and DTPA molecules was evidenced by the appearance of carboxyl (1705 cm⁻¹) and carboxylate (1599 and 1406 cm⁻¹) molecules.⁷² Finally, the sole change observed after chelation of Mn²⁺ was a shift of the carboxylate asymmetric vibration mode from 1631 to 1599 cm⁻¹. Previous studies have attributed this alteration to the coordination of metal ions by carboxylate groups.⁷³ Therefore, in the present work, this suggested Mn²⁺ chelation by DTPA.

The net charge of the colloids was also used to track the surface changes that occurred at each stage of the functionalization procedure (table 4.2). Pure Au NPs demonstrated a strong

negative net charge (-28.5 mV) at pH 10, which justified the long-term stability of this colloid. On the contrary, after grafting of PEG, the surface charge became strongly positive (22.3 mV) in de-ionized water.

Table 4.2 Zeta potential values (surface net charge) of Au NPs at the end of each functionalization step.

Sample	Zeta potential (mV)	Solvent	pH
Au NPs	-28.5 ± 3.3	3.3 mM NaOH	10
Au NPs@PEG	22.3 ± 2.7	De-ionized H ₂ O	7
Au NPs@DMSA-DTPA	-3.9 ± 1.8	De-ionized H ₂ O	7
Au NPs@PEG-Mn ²⁺	5.8 ± 0.1	De-ionized H ₂ O	7

This dramatic change was attributed to the presence of amine groups in the PEG molecules, which become protonated in water. Afterwards, the addition of DMSA-DTPA induced a decrease of the net charge (-3.9 ± 1.8 mV), due to the negative charge of carboxylate groups. However, the positive charge of Mn ions increased the surface charge and lead to a zeta potential of +5.8 mV. Given the strong positive surface charge Au NPs@PEG and the negative charge of the DMSA-DTPA complex, it is important to mention that although the initial design of the Au NPs@PEG-Mn²⁺ aimed at grafting the DMSA-DTPA chelates directly on the surface of the Au NPs, it is not possible to discard the possibility of electrostatic interaction between the NPs' positively charged surface and the DMSA-DTPA complex.

At last, the presence of Mn²⁺ was also confirmed by ¹H NMR because the Au NPs@PEG-Mn²⁺ efficiently decreased the *T*₁ and *T*₂ relaxation times of water (figure 4.14).

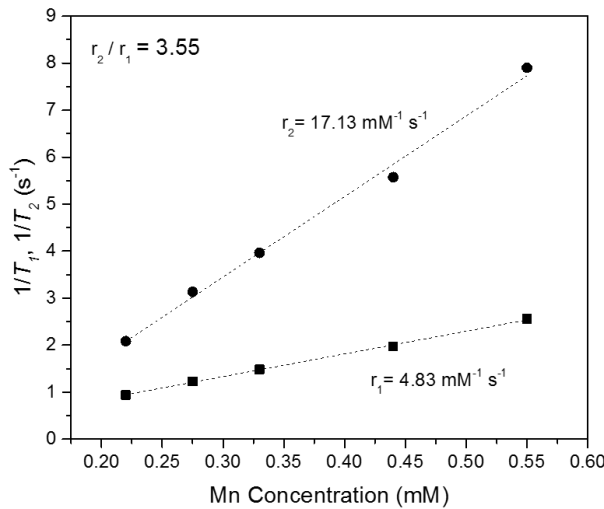


Figure 4.14 ^1H relaxation rates in function of the concentration of Mn in Au NPs@PEG-Mn $^{2+}$ at 37° C in 1.41 T.

The new colloid had a r_1 of $4.8 \text{ mM}^{-1} \text{ s}^{-1}$ and a relaxometric ratio (r_2/r_1) of 3.6, which is characteristic of “positive” MRI CAs. The r_1 value indicated that Mn $^{2+}$ was trapped within the PEG layer and chelated by DTPA, because this value was lower than that of solvated Mn $^{2+}$, but higher than that of free Mn $^{2+}$ -chelates.⁷⁴ Solvated Mn $^{2+}$ have higher relaxivity than the chelated forms, because the free ion has the five unpaired electrons available for inner-sphere coordination with the surrounding water molecules. However, after chelation with DTPA, there is no free unpaired electrons for direct coordination with the water molecules, which significantly decreases the relaxivity values. Nevertheless, the chelating agent is indispensable for *in vivo* applications due to the neurotoxicity of Mn $^{2+}$.⁴⁰ On the other hand, the increase of r_1 observed with Au NPs@PEG-Mn $^{2+}$ comparing with free Mn $^{2+}$ -chelates could be due to the lower tumbling rates of the large NPs in comparison with the small chelates, and because of increased viscosity of the medium.^{79, 85}

4.4.1 Colloidal stability and cytotoxicity of Au NPs@PEG-Mn²⁺

Biological application of NPs require testing the stability of the colloids in saline and protein rich media. Therefore, the colloidal stability of Au NPs@PEG-Mn²⁺ was measured up to seven days in de-ionized water (used as a control) and in 154 mM of NaCl. The colloid was stable for the duration of the experiment in water without formation of agglomerates (figure 4.15 (A)).

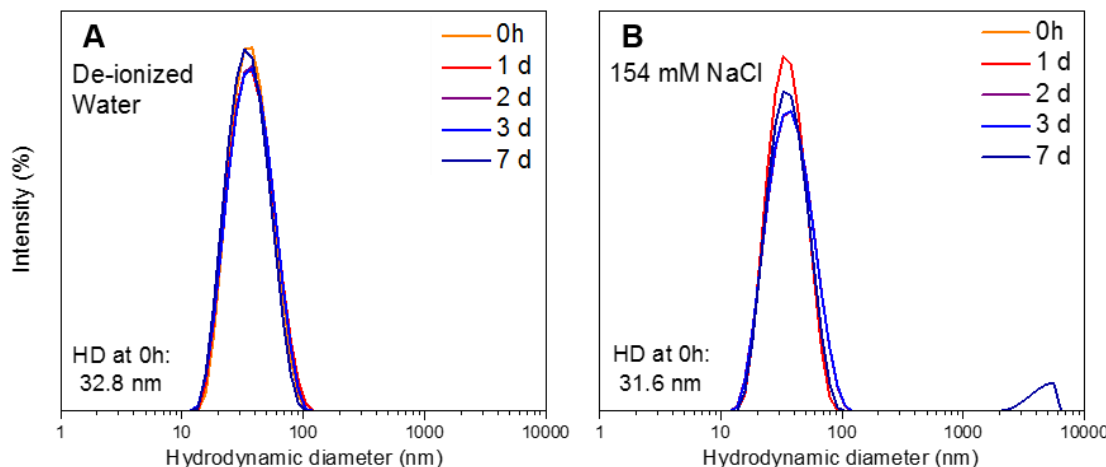


Figure 4.15 Hydrodynamic diameters of Au NPs@PEG-Mn²⁺ suspended in water (A) and 154 mM NaCl (B). The measurements were performed during seven days after suspending the NPs in the different solutions.

The Au NPs@PEG-Mn²⁺ also demonstrated strong stability in saline solution, although after seven days a minute amount (~1%) of agglomerates was detected in intensity-weighted DLS measurements (figure 4.15 (B)). The formation of these agglomerates could be related with the existence of some Au NP which were not densely coated by PEG. Thus, when dispersed in a strongly ionic solution, these particles can aggregate as the steric protection was not thick enough to overcome electrostatic and van der Walls attraction.⁶⁴ These results demonstrated that the Au NPs@PEG-Mn²⁺ could be dispersed in the saline solution required for injection and be stored at room temperature over a three days period without agglomerate formation. In addition, the minute concentration of agglomerates that could be formed upon a seven days storage in the saline medium can be easily removed by centrifugation before injection of the colloid.

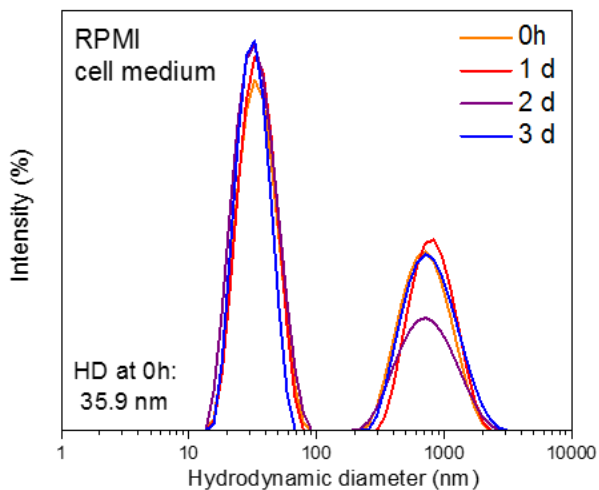


Figure 4.16 Hydrodynamic diameters of Au NPs@PEG-Mn²⁺ suspended in complete cell medium. The measurements were performed during three days after suspending the NPs in this medium.

The Au NPs@PEG-Mn²⁺ were also suspended in complete cell medium to assess the effect of saline and protein rich environment. Immediately after dispersion of the colloids in the cell medium, a bimodal size distribution was observed in intensity-weighted DLS measurements (figure 4.16). The majority of the NPs in the sample demonstrated from the beginning a slightly higher HD (35.9 nm) compared with the one observed in water (32.8 nm) or NaCl solution (31.6 nm). The other peak, centered at ~ 700 nm, accounted to only 5% of the measure scattered intensity. This bimodal size distribution remained unaffected during three days. The small fraction of agglomerates detected could have been formed due to adsorption and/or cross-linking between particles in the presence of high concentration of proteins, which contain charged or hydrophobic domains that can interact with the Au NPs@PEG-Mn²⁺ surface.⁷⁵ The small percentage of these agglomerates is not ideal for *in vivo* applications, however the HD of these agglomerates is not sufficiently large to cause vascular occlusion, and therefore the Au NPs@PEG-Mn²⁺ could still be used for vascular injection.⁷⁶ Nevertheless, improvements in NP design should be performed to attempt elimination of the formation of these agglomerates. Some strategies could include (1) to adjust the concentration of Mn²⁺-chelates to produce a zwitterionic surface, which seems to successfully avoid protein adsorption, or (2) to minimize the surface charge using methyl-terminated PEG molecules.⁷⁵

Possible cell toxicity effect of Au NPs@PEG-Mn²⁺ were also tested on PC3 prostate cancer cells. In these studies, long incubation times as well as high concentrations of NP were used to clearly demonstrate potential toxicity risks. This strategy was necessary because different cell types are expected to be in contact with relatively high concentrations of PEGylated-Au NPs for about 11 to 30 hours (observed blood half-lives for PEG-coated Au NPs in different studies).⁹⁴

109

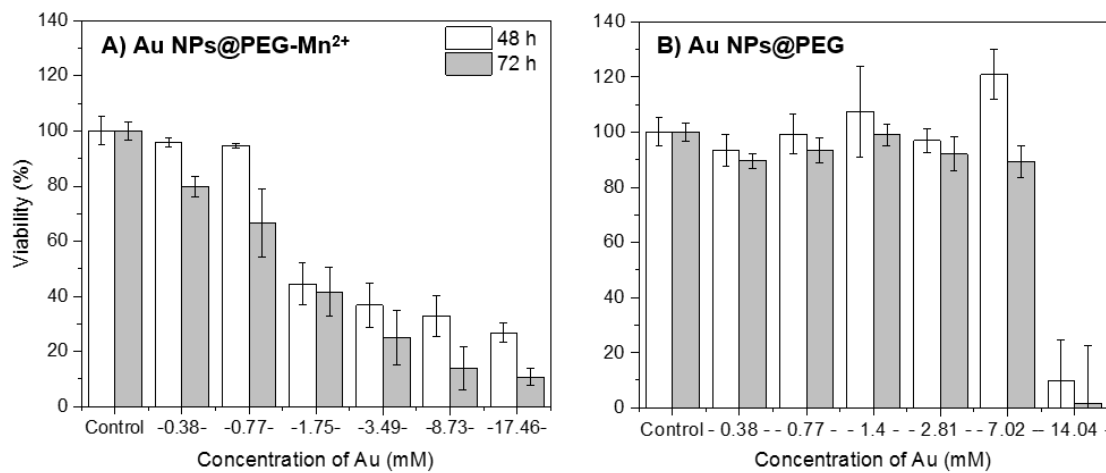


Figure 4.17 Cell toxicity studies of Au NPs@PEG-Mn²⁺ (A) and Au NPs@PEG (B) on PC3 cancer cells.

Although the cell viability was not significantly affected up to 48h of incubation and using 0.77 mM Au (which contained 0.009 mM of Mn²⁺), higher concentrations of Au NPs@PEG-Mn²⁺ significantly affected the viability of PC3 starting at 48 hours of incubation (figure 4.17 (A)). In order to investigate if the cause of cell toxicity was related with the nanostructure or with the Mn²⁺-chelates, a comparative study using only PEGylated Au NP was performed. Surprisingly, this study demonstrated that PC3 cells could tolerate up to 7 mM during 72h (figure 4.17 (B)). Therefore, these studies suggested that DMSA-DTPA-Mn²⁺ complexes may be the cause of cytotoxicity, when moderate and high concentrations of Au NPs@PEG-Mn²⁺ were used. Therefore, the concentration DMSA-DTPA-Mn²⁺ complexes should be decreased in future studies. Nevertheless, further assays using only Mn²⁺, DMSA-DTPA and Mn²⁺-DTPA should be performed in order to determine the exact source of cell toxicity. The fact that the metabolism of PC3 cancer cells was not affected by relatively high concentrations of PEGylated PLAL-synthesized Au NPs was a promising result, as most studies on the development of Au NP-based contrast agents for CT have reported cell viability studies using much lower Au concentrations.⁷⁷

⁷⁸ However, complementary assays should be performed to assure that these Au concentrations do not affect signaling pathways and gene expression in the cells.

4.4.2 CT/MRI dual imaging with Au NPs@PEG-Mn²⁺: a proof of concept

The possibility for dual MRI/CT contrast enhancement using Au NPs@PEG-Mn²⁺ was assessed *in vitro* and *in vivo* by intratumoural injections on a CAM prostate cancer model.

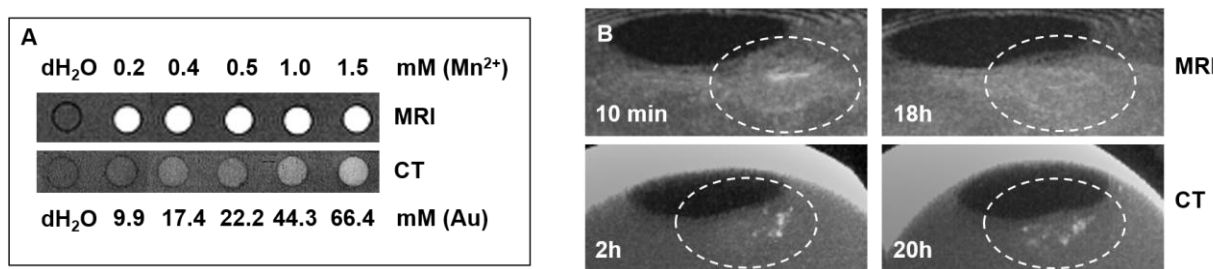


Figure 4.18 *In vitro* CT (40 kVp) / MRI (1.0 T) imaging of Au NPs@PEG-Mn²⁺ (A), and *in vivo* CT (40 kVp) / MRI (1.0 T) studies after injection of Au NPs@PEG-Mn²⁺ in a PC3 CAM tumour model (B). The dashed white circle outlines the tumour area. The CT and MRI images were acquired after the intratumoural injection of Au NPs@PEG-Mn²⁺ at different time points. The MR images, for both the *in vitro* and *in vivo* studies, were acquired using T_1 -weighted eco sequences.

Figure 4.18 (A) evidenced the contrast enhancement created by Au NPs@PEG-Mn²⁺ in both CT and MRI at different concentrations. As expected lower concentrations of Mn²⁺ (0.2 mM) were necessary to produce contrast enhancement in MRI, compared with the concentration of Au (44.3 mM) required for CT.

Injection of the Au NPs@PEG-Mn²⁺ in the PC3 CAM tumour model revealed a clear MRI (at 10 min) and CT (at 2 hours) contrast enhancement (figure 4.18 (B)). Injection follow up using both techniques permitted to track diffusion of Au NPs within the tumours matrix, especially by CT. In fact, the MRI signal faded significantly at 18 hours probably due to diffusion of the CA, which maybe reduced the concentration of Mn²⁺ bellow MRI detection threshold. In addition to the possibility for dual imaging by CT/MRI, these studies also evidenced lack of aggregation of NPs after the injection *in vivo*, as the colloids could easily diffuse away from the injection site over several hours.

4.4.3 Preliminary biodistribution studies of Au NPs@PEG-Mn²⁺

At last, the Au NPs@PEG-Mn²⁺ were injected in healthy CD-1 mice (n = 3) to assess their performance as CT vascular CAs and initial biodistribution. At the administered concentration, which was similar to the ones reported for vascular studies using Au NPs,^{65, 109, 151} the Au NPs@PEG-Mn²⁺ provided sufficient contrast enhancement to clearly observe the major blood vessels for at least 90 minutes after the injection (Figure 4.19 (A)). In addition, other organs (e.g. kidney, liver and spleen) demonstrated a slight contrast enhancement, which was likely related with the rich vasculature of these tissues. The overall contrast enhancement remained steady throughout the study starting at 15 min after the injection of the NPs, even in the spleen and liver (figure 4.19 (B)). This observation suggested a strong retention of the NPs in the bloodstream for a period suitable for angiographic procedures (e.g. 90 minutes). This can only be achieved if the coating of the NPs is not recognized by opsonin proteins, which would lead to quick uptake by organs of the MPS (e.g. liver and spleen) and if the particles do not form large agglomerates, which also triggers quick removal of the particles from the blood.^{30, 116}

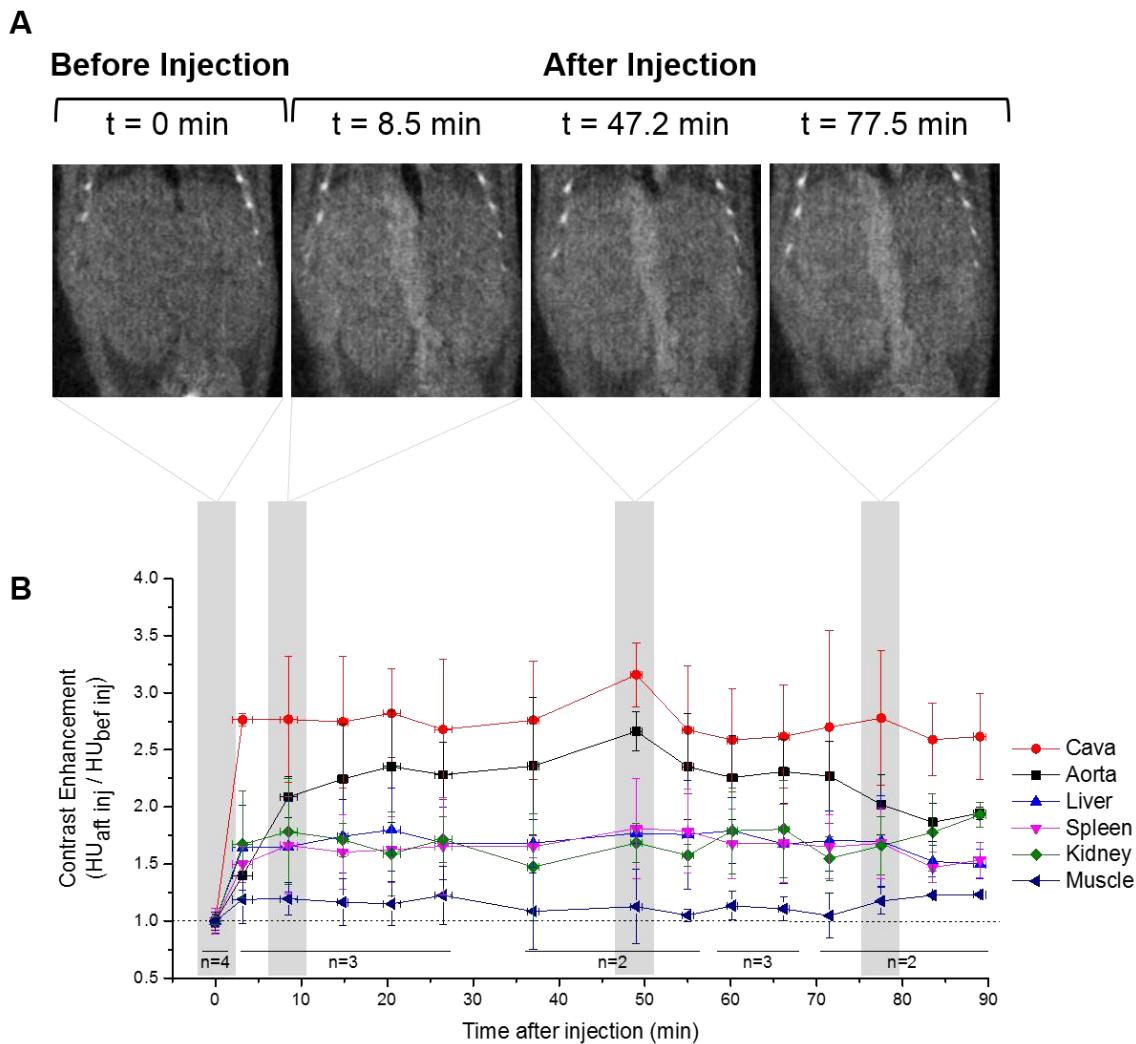


Figure 4.19 DCE-CT (40 kVp_ studies performed during 90 minutes after intravenous injection of Au NPs@PEG-Mn²⁺ in mouse models. Images show coronal sections the abdominal region in a representative mouse injected with Au NPs@PEG-Mn²⁺. The graph displays the contrast enhancement before (0 min), and at different time points following the injection.

In addition, the animals did not demonstrate signs of adverse reactions during the experiment. Finally, the biodistribution profile observed was relatively similar to those obtained with commercial Au NPs CT agents (e.g. Aurovist™, these results are included in the support information of Article 2), and to others reported in studies using PEGylated Au NPs for blood pool imaging with CT.^{109, 151}

5. CONCLUSIONS

During the first phase of this thesis, the potential of PLAL to produce Au-Gd and Au-Mn NPs in a single step was studied, as this type of NPs could be advantageous for cancer diagnosis and radiotherapy planning by CT and MRI.⁶⁻¹⁰ Pulsed laser ablation of a Au₅₀Gd₅₀ target using a UV ns-laser, in solutions with pH varying from 7 to 11, in the presence of PEG or in a solution at pH 11 using different fluences, resulted in the formation of a Gd₂O₃ network containing small Au NPs, as observed by TEM and EDS. The formation of the Gd₂O₃ network was likely a result of strong laser energy absorption and consequent melting of Gd₂O₃ NPs formed from ablation of the target. Despite the formation of an interesting structure, this composite material was not suitable for an application as a CA for *in vivo* imaging due to the shape and the lack of colloidal stability. On the other hand, pulsed laser ablation of a Au₆₄Mn₃₆ metal target produced small Au-MnO_x NPs containing approximately 29% of Mn and 71% of Au (at.), as measured by NAA, EDS and XPS. These particles were composed of a small Au core (4.8 nm) partially covered with a thin MnO_x layer (0.3 to 1.3 nm), as observed by TEM and HAADF HR-STEM. Despite meeting colloidal stability and size requirements for biomedical imaging applications, XAFS analysis demonstrated that the oxidation state of Mn was too high to allow the application of this nanostructure as an efficient CA for MRI.

Therefore, the second approach developed in this thesis was to functionalize Au NPs produced by PLAL with PEG and Mn²⁺-chelates. The first step of this strategy was to optimize the conditions of PLAL synthesis that would provide the best compromise between small size, low polydispersity and increased production rate. Hence, Au NPs with an average HD of 17.5 nm (8.0 nm core size as measured by TEM) and a polydispersity index of 0.3 were synthesized in de-ionized water containing 3.3 mM of NaOH, using a 1064 nm ns-laser. Surface analysis of these NPs confirmed the purity (i.e. absence of typical reactants used for chemical synthesis) characteristic of Au NPs produced by PLAL.⁶³ Afterwards, steric stabilization of the Au NPs was easily achieved in aqueous solutions containing minimal excess of PEG, and the production of composite NPs was obtained through the addition of DMSA-DTPA and Mn²⁺ to the PEGylated Au NPs. The final product, Au NPs@PEG-Mn²⁺, had an average HD of 36.5 nm and a polydispersity index of 0.2, which were suitable for *in vivo* application of this material. Hence, the particles were thoroughly characterized in order to investigate their potential for biomedical imaging. During these studies, it was possible to demonstrate (1) the colloidal stability of the Au@PEG-Mn²⁺ NPs

for several days at room temperature in de-ionized water, saline solution and complete cell medium; and (2) that the Au@PEG-Mn²⁺ NPs were suitable for dual imaging by CT/MRI. At last, CT imaging of mouse models after intravenous injection of the Au@PEG-Mn²⁺ NPs demonstrated a stable contrast enhancement in large vessels for at least 90 minutes after the injection. In addition, the contrast enhancement produced in the liver and spleen was steady during this period. This suggested that the Au@PEG-Mn²⁺ NPs evaded MPS recognition, which indicated the presence of an adequate PEG coating.

Therefore, thanks to PLAL synthesis, it was possible to create composite NPs, covered by biocompatible molecules already used in clinical practice, through a simple and exclusively aqueous-based method. This was the first time that such a procedure was described for the development of CT/MRI CAs using Au NPs and a paramagnetic element. The procedures previously reported for the synthesis of this type of CA, required the utilization of different organic solvents, reducing and stabilizing agents, which were avoided in this study, leading to pristine NPs surfaces.^{16-20, 22} In fact, the purity of the Au NPs produced by PLAL was evident from the cytotoxicity assays performed with the Au NPs@PEG. In this assay, it was observed that the viability of PC3 cells was not affect up to 72h in the presence of 7 mM of Au. This was an interesting result, as most studies dedicated to assess the toxicity of PEGylated Au NPs have performed cell viability studies with significantly lower Au concentrations.⁷⁷⁻⁷⁸ Another particularity of the toxicity studies performed in this thesis, was to expose the PC3 cells for relatively long periods to the high concentrations of Au. This was an important evaluation for the application of Au NPs as a CA for CT, as relatively high concentrations of Au have to be injected *in vivo*, and these materials are expected to remain in circulation for several hours, and to accumulate in different organs for many days before being excreted.^{94, 104, 109} However, this type of high concentration and long cell exposure study has not been reported in the literature yet.

In contrast with the cytotoxicity studies performed on Au NPs@PEG, the presence of the Mn²⁺-chelates on the surface of these particles, affected the cell viability at lower concentrations of Au, decreasing it to approximately 65% after 48h of incubation. Therefore, the innocuous concentrations of Au NPs@PEG-Mn²⁺ are limited to less than 0.77 mM of Au and 0.009 mM of Mn²⁺. Nonetheless, other studies dedicated to the development of “positive” MRI/CT CAs have reported cell viability reduction to 30% already after 24h of incubation with 100 µM of Au.¹⁹ Thus, the Au@PEG-Mn²⁺ NPs presented lower cytotoxicity comparing with other “positive” MRI/CT CAs. Despite these promising results, the concentration of Mn²⁺-chelates could be optimized in order

to decorate the PEGylated Au NPs with the minimum concentration possible of Mn²⁺-chelates (i.e. the concentration necessary to obtain sufficient contrast enhancement by MRI).

Another advantage of the present CA is the relatively small HD (36.5 nm), as other multifunctional NPs for the same application demonstrated HD values larger than 80 nm, especially after coating with non-biofouling polymers.¹⁸⁻²⁰ In addition, the Au NPs@PEG-Mn²⁺ were the first CA designed for CT/MRI using Au NPs and Mn²⁺-chelates. There are different works on CT/MRI CAs combining Au NPs and Gd³⁺, because this paramagnetic element presents higher relaxivities.^{16-20, 22} However, for applications using Au NPs with HDs higher than 10 nm, which are expected to remain in the body for several days before elimination (as the case of the present work), Mn²⁺ could be beneficial comparing with Gd³⁺, as it is less toxic. Surprisingly, comparison of the longitudinal relaxivity (r_1) obtained for the Au NPs@PEG-Mn²⁺ with others reported in different works dedicated to the development of “positive” MRI/CT CAs (table 5.1), suggested that the design of Au NPs@PEG-Mn²⁺ allowed to achieve a r_1 comparable to most of the CAs containing Gd³⁺-chelates, and relatively higher than Au@MnO nanostructures. This confirmed that the addition of Mn²⁺-chelates to the Au NPs’ surface is not only a less toxic alternative, but it also allows to achieve relaxivities comparable to NPs containing Gd³⁺.

Table 5.1 Longitudinal relaxivities (r_1) of nanoparticle-based “positive” MRI/CT contrast agents

NP-based “positive” MRI/CT CA	r_1 (mM ⁻¹ s ⁻¹)	Magnetic field strength (T) /Temperature (°C)	Reference
Au NPs@PEG-Mn ²⁺	4.8	1.4 / 37	Current work
Au-HDL	12.2	1.4 / 40	22
NaY/GdF ₄ : Yb, Er, Tm@silica-Au NPs	1.25	3.0 / RT	18
Gd-Au DENPs	1.05	3.0 / RT	19
GdMOF-PAA-Au nanocomposites	4.9	4.7 / RT	20
Au@DTDTPA-Gd ₅₀ NPs	4.1	7.0 / 25	17
Au@MnO nanoflowers	0.22	3.0 / RT	105

To finalize, the second multi-step strategy explored in this thesis allowed to control the oxidation of the paramagnetic element added on the surface of the Au NPs. Thus, this method was suitable to produce a NP-based CA appropriate for dual imaging by CT/MRI, using a simple and aqueous based procedure, which presents a significant advantage comparing with previously reported methods for the synthesis of “positive” MRI/CT CAs.

5.1 Perspectives

The work described in this thesis demonstrated the benefits that PLAL-synthesized NPs can bring for CA applications, and evidenced some limitations of this method, which will require further research in order to reach the full potential that PLAL can offer to the field of NP-based CAs. Therefore, some suggestions for future investigation are as follow:

- the production of individual Au-Gd₂O₃ NPs by PLAL in a single step may be achieved by reducing the content of Gd in the metal target, and by decreasing the particle size of the micro-powder used to make the target, or by using Au-Gd alloyed target (however, using an alloy with low content of Gd). These strategies will create an environment with less Gd and with increased homogeneity of the ablated elements, which may favor the formation of a relatively thin layer of Gd₂O₃ around the Au NPs. If a network still appears, another option would be to change the laser wavelength, for example 532 nm or 1064 nm laser wavelengths could be used. At these wavelengths different absorption of light should occur, so it might be possible to avoid the formation of the Gd₂O₃ net. Afterwards, different pulse widths (e.g. ps or fs) could also be tested, especially to increase ablation rate (assuming that the required structure is still obtained).
- the synthesis of Au-MnO_x NPs in a single step by PLAL requires controlling the oxidation state of Mn. Thus, characterization of the Mn oxidation obtained using different laser wavelengths and pulse width, may provide more information on how to minimize the oxidation of Mn during the ablation in aqueous media. Another approach would be to explore the ablation of the target in ethanol, as Amendola *et al.* performed to obtain the Au-Fe alloy NPs.²³ However, for this strategy, UV lasers cannot be used due to strong absorption of organic solvents in the UV regime. At last, if synthesis in ethanol produces suitable nanostructures, careful surface characterization should be performed to ensure that the purity of the NPs' surface is not compromised.
- the Au NPs@PEG-Mn²⁺ could also be improved regarding (1) the size polydispersity; (2) the binding strength of the PEG layer to the Au NP surface, (3) the Au/Mn ratio, and (4) the surface charge as well as to minimize electrostatic interaction of DMSA-DTPA complex with the charged PEG layer. As soon as the enumerated parameters are optimized, scale up of the procedure would also be necessary. For the first aspect, a possible avenue would be to perform post-irradiation of the colloid produced by ablation of Au target using a 1064 nm laser. The post-irradiation should be performed using a 532 nm ps-laser, as this wavelength and pulse width can

efficiently fragment the Au NPs. Considering the second point, a suitable strategy could be to use di-thiol or multi-dentate PEG molecules, because multiple anchoring groups could strengthen the binding of PEG to the Au NPs' surface. The third point, would require to produce Au NPs@PEG-Mn²⁺ using different Mn²⁺-chelates ratios, another chelating agent (e.g. EDTA), or to change the incubation time of DMSA-DTPA with Au NPs@PEG. Afterwards, the new Au NPs@PEG-Mn²⁺ with different Au/Mn ratios would have to be tested for dual imaging in order to determine the best ratio. Regarding the surface charge, it could be minimized by using a mixture of methyl- and amine-terminated PEG molecules, which would still allow latter functionalization with targeting ligands. To finalize, scale up of the procedure could be performed by minimizing the time spent on the functionalization steps (e.g. by determining the possibility of adding the Mn²⁺ already chelated to the Au NPs@PEG). The next step of this investigation would be to increase the reaction volumes. In a final phase, a reactor transferring irradiated particles directly to a container with the PEG would again significantly reduce the production time.

PART II: ARTICLES

Cet article a dû être retiré de la version électronique en raison de restrictions liées au droit d'auteur.

ARTICLE 1: GOLD-MANGANESE OXIDE CORE-SHELL NANOPARTICLES PRODUCED BY PULSED LASER ABLATION IN WATER

AUTHORS

Teresa Simao,¹ Daniel M. Chevrier,² Jurij Jakobi,³ Andreas Korinek,⁴ Gregory Goupil,¹ Marcus Lau,³ Sébastien Garbarino,¹ Peng Zhang,² Stephan Barcikowski,³ Marc-André Fortin,^{*5, 6, 7} Daniel Guay^{*1}

¹ Institut National de la Recherche Scientifique, Centre Énergie Matériaux Télécommunications, 1650 Lionel-Boulet Boulevard, Varennes (QC), J3X 1S2, Canada; ² Department of Chemistry, Dalhousie University, Halifax (NS), B3H 4R2, Canada; ³ Technical Chemistry I, University of Duisburg-Essen and Center for Nanointegration Duisburg-Essen CENIDE, Universitaetsstrasse 7, 45141 Essen, Germany; ⁴ Canadian Centre for Electron Microscopy, Brockhouse Institute for Materials Research, McMaster University, 1280 Main Street West, Hamilton (ON), L8S 4M1, Canada; ⁵ Centre de recherche du Centre hospitalier universitaire de Québec (CR-CHUQ), Axe médecine régénératrice, Quebec City (QC), G1L 3L5, Canada; ⁶ Centre de recherche sur les matériaux avancés (CERMA), Université Laval, Quebec City (QC), G1V 0A6, Canada; ⁷ Département de Génie des Mines, de la Métallurgie et des Matériaux, Université Laval, Quebec City (QC), G1V 0A6, Canada

CONTRIBUTION

Prepared the metal targets, determined the parameters for the synthesis of Au-MO_x and Au NPs by PLAL, and performed the synthesis of the Au-MO_x NPs using the different lasers. Performed all the material characterization and data analysis, except the acquisition of TEM images of Au NPs, HAADF HR-STEM, EELS, XAFS, HAADF STEM and EDS. XAFS data analysis was also performed by a co-author.

Wrote the first version of the manuscript, which was later revised by the co-authors.

PUBLICATION

Submitted to the Journal of Physical Chemistry C

ARTICLE 2: LASER-SYNTHESIZED LIGAND-FREE AU NANOPARTICLES FOR CONTRAST AGENT APPLICATIONS IN COMPUTED TOMOGRAPHY AND MAGNETIC RESONANCE IMAGING

AUTHORS

Teresa Simão,¹ Pascale Chevallier,^{2,3} Jean Lagueux,² Marie-France Côté,² Christoph Rehbock,⁴ Stephan Barcikowski,⁴ Marc-André Fortin,^{*2,3,5} Daniel Guay^{*1}

¹ Institut National de la Recherche Scientifique (INRS), Centre Énergie Matériaux Télécommunications 1650 Lionel-Boulet Boulevard, Varennes (QC), J3X 1S2, Canada; ² Centre de recherche du Centre hospitalier universitaire de Québec (CR-CHUQ), Axe Médecine Régénératrice, Quebec City (QC), G1L 3L5, Canada; ³ Centre de recherche sur les matériaux avancés (CERMA), Université Laval, Quebec City (QC), G1V 0A6, Canada; ⁴ Technical Chemistry I, University of Duisburg-Essen and Center for Nanointegration Duisburg-Essen CENIDE, Universitaetsstrasse 7, 45141 Essen, Germany; ⁵ Département de génie des mines, de la métallurgie et des matériaux, Université Laval, Quebec City (QC), G1V 0A6, Canada

CONTRIBUTION

Determined the parameters for the synthesis of the Au NPs by PLAL, participated in the design of the functionalization procedure and optimized it. Performed all the material characterization and data analysis, except the XPS data acquisition, which was performed by Dr. Pascale Chevallier.

For the cell toxicity studies, participated in the design of the experiment, prepared the NPs for the studies, performed data acquisition and analysis of the results. Cell culture and handling procedures were performed by Dr. Marie-France Côté.

For the *in vitro* and *in vivo* imaging studies participated in the design of the experiment, prepared the NPs for the studies, and performed data analysis. The development of the CAM tumour model and intratumoural injections were performed by Dr. Marie-France Côté. Animal handling as well as MRI and CT image acquisitions were performed by Dr. Jean Lagueux.

Wrote the first version of the manuscript, which was later revised by the co-authors.

6. REFERENCES

1. Statistics, C. C. S. s. A. C. o. C. *Canadian Cancer Statistics 2013*; Canadian Cancer Society: Toronto, ON, **2013**; pp 1-114.
2. Statistics, C. C. S. s. A. C. o. C. *Canadian Cancer Statistics 2015*; Canadian Cancer Society: Toronto, ON, **2015**; pp 1-151.
3. Solomon, S. B.; Silverman, S. G., Imaging in interventional oncology. *RY* **2010**, 257 (3), 624-40.
4. Turkbey, B.; Kobayashi, H.; Ogawa, M.; Bernardo, M.; Choyke, P. L., Imaging of tumor angiogenesis: functional or targeted? *American Journal of Roentgenology* **2009**, 193 (2), 304-13.
5. Brindle, K., New approaches for imaging tumour responses to treatment. *Nat Rev Cancer* **2008**, 8 (2), 94-107.
6. Barentsz, J. O.; Richenberg, J.; Clements, R.; Choyke, P.; Verma, S.; Villeirs, G.; Rouviere, O.; Logager, V.; Futterer, J. J.; European Society of Urogenital, R., ESUR prostate MR guidelines 2012. *Eur Radiol* **2012**, 22 (4), 746-57.
7. Hricak, H.; Choyke, P. L.; Eberhardt, S. C.; Leibel, S. A.; Scardino, P. T., Imaging prostate cancer: a multidisciplinary perspective. *RY* **2007**, 243 (1), 28-53.
8. Kuhl, C., The current status of breast MR imaging. Part I. Choice of technique, image interpretation, diagnostic accuracy, and transfer to clinical practice. *RY* **2007**, 244 (2), 356-78.
9. Prionas, N. D.; Lindfors, K. K.; Ray, S.; Huang, S. Y.; Beckett, L. A.; Monsky, W. L.; Boone, J. M., Contrast-enhanced dedicated breast CT: initial clinical experience. *RY* **2010**, 256 (3), 714-23.
10. Sardanelli, F.; Boetes, C.; Borisch, B.; Decker, T.; Federico, M.; Gilbert, F. J.; Helbich, T.; Heywang-Kobrunner, S. H.; Kaiser, W. A.; Kerin, M. J.; Mansel, R. E.; Marotti, L.; Martincich, L.; Mauriac, L.; Meijers-Heijboer, H.; Orechia, R.; Panizza, P.; Ponti, A.; Purushotham, A. D.; Regitnig, P.; Del Turco, M. R.; Thibault, F.; Wilson, R., Magnetic resonance imaging of the breast: recommendations from the EUSOMA working group. *European Journal of Cancer* **2010**, 46 (8), 1296-316.
11. Claus, F.; Hricak, H., Imaging in Radiation Therapy: Recent Advances and Their Role in Radiotherapy. In *Technical Basis of Radiation Therapy: Practical Clinical Applications*, Levitt, S. H.; Purdy, J. A.; Perez, C. A.; Vijayakumar, S., Eds. Springer Berlin Heidelberg: **2008**; Chapter 4.
12. Weissleder, R., Scaling down imaging: molecular mapping of cancer in mice. *Nat Rev Cancer* **2002**, 2 (1), 11-8.
13. Krause, W., Delivery of diagnostic agents in computed tomography. *Adv Drug Deliv Rev* **1999**, 37 (1-3), 159-173.
14. Zheng, J.; Liu, J.; Dunne, M.; Jaffray, D. A.; Allen, C., In vivo performance of a liposomal vascular contrast agent for CT and MR-based image guidance applications. *Pharm Res* **2007**, 24 (6), 1193-201.
15. Zheng, J.; Perkins, G.; Kirilova, A.; Allen, C.; Jaffray, D. A., Multimodal contrast agent for combined computed tomography and magnetic resonance imaging applications. *Invest Radiol* **2006**, 41 (3), 339-48.

16. Debouttière, P. J.; Roux, S.; Vocanson, F.; Billotey, C.; Beuf, O.; Favre-Réguillon, A.; Lin, Y.; Pellet-Rostaing, S.; Lamartine, R.; Perriat, P.; Tillement, O., Design of Gold Nanoparticles for Magnetic Resonance Imaging. *Adv. Funct. Mater.* **2006**, 16 (18), 2330-2339.
17. Alric, C.; Taleb, J.; Duc, G. L.; Mandon, C., Gadolinium Chelate Coated Gold Nanoparticles As Contrast Agents for Both X-ray Computed Tomography and Magnetic Resonance Imaging. *J. Am. Chem. Soc.* **2008**, 130, 5908-5915.
18. Xing, H.; Bu, W.; Zhang, S.; Zheng, X.; Li, M.; Chen, F.; He, Q.; Zhou, L.; Peng, W.; Hua, Y.; Shi, J., Multifunctional nanoprobes for upconversion fluorescence, MR and CT trimodal imaging. *Biomaterials* **2012**, 33 (4), 1079-89.
19. Wen, S.; Li, K.; Cai, H.; Chen, Q.; Shen, M.; Huang, Y.; Peng, C.; Hou, W.; Zhu, M.; Zhang, G.; Shi, X., Multifunctional dendrimer-entrapped gold nanoparticles for dual mode CT/MR imaging applications. *Biomaterials* **2013**, 34 (5), 1570-80.
20. Tian, C.; Zhu, L.; Lin, F.; Boyes, S. G., Poly(acrylic acid) Bridged Gadolinium Metal-Organic Framework-Gold Nanoparticle Composites as Contrast Agents for Computed Tomography and Magnetic Resonance Bimodal Imaging. *ACS Appl. Mater. Interfaces* **2015**, 7 (32), 17765-75.
21. Chou, S. W.; Shau, Y. H.; Wu, P. C.; Yang, Y. S.; Shieh, D. B.; Chen, C. C., In vitro and in vivo studies of FePt nanoparticles for dual modal CT/MRI molecular imaging. *J. Am. Chem. Soc.* **2010**, 132 (38), 13270-8.
22. Cormode, D. P.; Skajaa, T.; van Schooneveld, M. M.; Koole, R.; Jarzyna, P.; Lobatto, M. E.; Calcagno, C.; Barazza, A.; Gordon, R. E.; Zanzonico, P.; Fisher, E. A.; Fayad, Z. A.; Mulder, W. J., Nanocrystal core high-density lipoproteins: a multimodality contrast agent platform. *Nano Lett.* **2008**, 8 (11), 3715-23.
23. Amendola, V.; Scaramuzza, S.; Litti, L.; Meneghetti, M.; Zuccolotto, G.; Rosato, A.; Nicolato, E.; Marzola, P.; Fracasso, G.; Anselmi, C.; Pinto, M.; Colombatti, M., Magneto-plasmonic Au-Fe alloy nanoparticles designed for multimodal SERS-MRI-CT imaging. *Small* **2014**, 10 (12), 2476-86.
24. Li, J.; Hu, Y.; Yang, J.; Wei, P.; Sun, W.; Shen, M.; Zhang, G.; Shi, X., Hyaluronic acid-modified Fe₃O₄@Au core/shell nanostars for multimodal imaging and photothermal therapy of tumors. *Biomaterials* **2015**, 38 (C), 10-21.
25. Ferrari, M., Cancer nanotechnology: opportunities and challenges. *Nat Rev Cancer* **2005**, 5 (3), 161-71.
26. Weissleder, R.; Pittet, M. J., Imaging in the era of molecular oncology. *Nature* **2008**, 452 (7187), 580-589.
27. Dreaden, E. C.; Mackey, M. A.; Huang, X.; Kang, B.; El-Sayed, M. A., Beating cancer in multiple ways using nanogold. *Chem. Soc. Rev.* **2011**, 40 (7), 3391.
28. Algar, W. R.; Prasuhn, D. E.; Stewart, M. H.; Jennings, T. L.; Blanco-Canosa, J. B.; Dawson, P. E.; Medintz, I. L., The controlled display of biomolecules on nanoparticles: a challenge suited to bioorthogonal chemistry. *Bioconjugate Chem.* **2011**, 22 (5), 825-58.
29. De, M.; Ghosh, P. S.; Rotello, V. M., Applications of Nanoparticles in Biology. *Adv. Mater.* **2008**, 20 (22), 4225-4241.
30. Albanese, A.; Tang, P. S.; Chan, W. C., The effect of nanoparticle size, shape, and surface chemistry on biological systems. *Annu. Rev. Biomed. Eng.* **2012**, 14 (1), 1-16.

31. Park, J. W.; Shumaker-Parry, J. S., Strong resistance of citrate anions on metal nanoparticles to desorption under thiol functionalization. *ACS Nano* **2015**, 9 (2), 1665-82.
32. Skotland, T.; Iversen, T. G.; Sandvig, K., New metal-based nanoparticles for intravenous use: requirements for clinical success with focus on medical imaging. *Nanomedicine: Nanotechnology, Biology, and Medicine* **2010**, 6 (6), 730-7.
33. Amendola, V.; Meneghetti, M., Laser ablation synthesis in solution and size manipulation of noble metal nanoparticles. *Physical Chemistry Chemical Physics* **2009**, 11 (20), 3805.
34. Neumeister, A.; Jakobi, J.; Rehbock, C.; Moysig, J.; Barcikowski, S., Monophasic ligand-free alloy nanoparticle synthesis determinants during pulsed laser ablation of bulk alloy and consolidated microparticles in water. *Phys. Chem. Chem. Phys.* **2014**, 16 (43), 23671-8.
35. Wagener, P.; Jakobi, J.; Rehbock, C.; Chakravadhanula, V. S. K.; Thede, C.; Wiedwald, U.; Bartsch, M.; Kienle, L.; Barcikowski, S., Solvent-surface interactions control the phase structure in laser-generated iron-gold core-shell nanoparticles. *Sci. Rep.* **2016**, 1-12.
36. Zhang, J.; Oko, D. N.; Garbarino, S.; Imbeault, R.; Chaker, M.; Tavares, A. C.; Guay, D.; Ma, D., Preparation of PtAu Alloy Colloids by Laser Ablation in Solution and Their Characterization. *J. Phys. Chem. C* **2012**, 116 (24), 13413-13420.
37. Petersen, S.; Barcikowski, S., Conjugation Efficiency of Laser-Based Bioconjugation of Gold Nanoparticles with Nucleic Acids. *J. Phys. Chem. C* **2009**, 113, 19830-19835.
38. Committee, A. I. H., *ASM Handbook: Alloy phase diagrams*. ASM International: **1992**.
39. Love, J. C.; Estroff, L. A.; Kriebel, J. K.; Nuzzo, R. G.; Whitesides, G. M., Self-Assembled Monolayers of Thiolates on Metals as a Form of Nanotechnology. *Chem. Rev.* **2005**, 105 (4), 1103-1170.
40. Kueny-Stotz, M.; Garofalo, A.; Felder-Flesch, D., Manganese-Enhanced MRI Contrast Agents: From Small Chelates to Nanosized Hybrids. *Eur. J. Inorg. Chem.* **2012**, 2012 (12), 1987-2005.
41. Eustis, S.; El-Sayed, M. A., Why gold nanoparticles are more precious than pretty gold: Noble metal surface plasmon resonance and its enhancement of the radiative and nonradiative properties of nanocrystals of different shapes. *Chem Soc Rev* **2006**, 35 (3), 209-217.
42. Rahme, K.; Chen, L.; Hobbs, R. G.; Morris, M. A.; O'Drisoll, C.; Holmes, J. D., PEGylated gold nanoparticles: polymer quantification as a function of PEG lengths and nanoparticle dimensions. *RSC Adv.* **2013**, 3 (17), 6085-6094.
43. Jennings, T.; Strouse, G., Past, Present, and Future of Gold Nanoparticles. In *Bio-Applications of Nanoparticles*, Chan, W. W., Ed. Springer New York: **2007**; Chapter 3, pp 34-47.
44. Muto, H.; Yamada, K.; Miyajima, K.; Mafune, F., Estimation of surface oxide on surfactant-free gold nanoparticles laser-ablated in water. *J Phys Chem C* **2007**, 111 (46), 17221-17226.
45. Rehbock, C.; Merk, V.; Gamrad, L.; Streubel, R.; Barcikowski, S., Size control of laser-fabricated surfactant-free gold nanoparticles with highly diluted electrolytes and their subsequent bioconjugation. *Physical Chemistry Chemical Physics* **2013**, 15 (9), 3057.
46. Merk, V.; Rehbock, C.; Becker, F.; Hagemann, U.; Nienhaus, H.; Barcikowski, S., In SituNon-DLVO Stabilization of Surfactant-Free, Plasmonic Gold Nanoparticles: Effect of Hofmeister's Anions. *Langmuir* **2014**, 30 (15), 4213-4222.

47. Owen, T., *Fundamentals of Modern UV-visible Spectroscopy: Primer*. Agilent Technologies: **2000**.
48. Williams, D. B.; Carter, C. B., *Transmission Electron Microscopy: A Textbook for Materials Science*. Springer US: **2009**.
49. Fultz, B.; Howe, J. M., *Transmission Electron Microscopy and Diffractometry of Materials*. Springer Berlin Heidelberg: **2007**.
50. Cullity, B. D., *Elements of X-ray Diffraction*. Addison-Wesley Publishing Company: **1978**.
51. Brandon, D. G.; Kaplan, W. D., Chemical Analysis of Surface Composition. In *Microstructural characterization of materials*, John Wiley: **2008**; Chapter 8.
52. Lucas, C. A., Surface Structure Determination by Interference Techniques. In *Surface Analysis: The Principal Techniques*, Vickerman, J. C.; Gilmore, I., Eds. Wiley: **2009**; Chapter 8.
53. Leng, Y., Vibrational Spectroscopy for Molecular Analysis. In *Materials Characterization: Introduction to Microscopic and Spectroscopic Methods*, Wiley: **2012**; Chapter 9.
54. Collins, A., Common Analytical Techniques for Nanoscale Materials. In *Nanotechnology Cookbook: Practical, Reliable and Jargon-free Experimental Procedures*, Elsevier Science: **2012**; Chapter 3.
55. O'Brien, J.; Wilson, I.; Orton, T.; Pognan, F., Investigation of the Alamar Blue (resazurin) fluorescent dye for the assessment of mammalian cell cytotoxicity. *Eur J Biochem* **2000**, 267(17), 5421-6.
56. Tarasenko, N. V.; Butsen, A. V.; Nevar, A. A., Laser ablation of gadolinium targets in liquids for nanoparticle preparation. *Applied Physics A* **2008**, 93 (4), 837-841.
57. Tsuji, T., Preparation of nanoparticles using laser ablation in liquids: fundamental aspects and efficient utilization. In *Laser Ablation in Liquids: Principles and Applications in the Preparation of Nanomaterials*, Yang, G., Ed. Pan Stanford Publishing: **2012**; Chapter 4.
58. Jain, P. K.; Huang, X.; El-Sayed, I. H.; El-Sayed, M. A., Noble metals on the nanoscale: optical and photothermal properties and some applications in imaging, sensing, biology, and medicine. *Acc. Chem. Res.* **2008**, 41 (12), 1578-86.
59. Link, S.; Wang, Z. L.; El-Sayed, M. A., Alloy Formation of Gold–Silver Nanoparticles and the Dependence of the Plasmon Absorption on Their Composition. *J. Phys. Chem. B* **1999**, 103 (18), 3529-3533.
60. Link, S.; El-Sayed, M. A., Shape and size dependence of radiative, non-radiative and photothermal properties of gold nanocrystals. *Int Rev Phys Chem* **2000**, 19 (3), 409-453.
61. Amendola, V.; Meneghetti, M.; Bakr, O. M.; Riello, P.; Polizzi, S.; Anjum, D. H.; Fiameni, S.; Arosio, P.; Orlando, T.; de Julian Fernandez, C.; Pineider, F.; Sangregorio, C.; Lascialfari, A., Coexistence of plasmonic and magnetic properties in Au₈₉Fe₁₁ nanoalloys. *Nanoscale* **2013**, 5 (12), 5611-9.
62. Geraldes, C. F.; Laurent, S., Classification and basic properties of contrast agents for magnetic resonance imaging. *Contrast Media Mol Imaging* **2009**, 4 (1), 1-23.
63. Sylvestre, J. P.; Poulin, S.; Kabashin, A. V.; Sacher, E.; Meunier, M.; Luong, J. H. T., Surface chemistry of gold nanoparticles produced by laser ablation in aqueous media. *J Phys Chem B* **2004**, 108 (43), 16864-16869.

64. Pfeiffer, C.; Rehbock, C.; Huhn, D.; Carrillo-Carrion, C.; de Aberasturi, D. J.; Merk, V.; Barcikowski, S.; Parak, W. J., Interaction of colloidal nanoparticles with their local environment: the (ionic) nanoenvironment around nanoparticles is different from bulk and determines the physico-chemical properties of the nanoparticles. *Journal of The Royal Society Interface* **2014**, 11 (96), 20130931-20130931.
65. Hainfeld, J. F.; Slatkin, D. N.; Focella, T. M.; Smilowitz, H. M., Gold nanoparticles: a new X-ray contrast agent. *Br J Radiol* **2006**, 79 (939), 248-253.
66. Hashimoto, S.; Werner, D.; Uwada, T., Studies on the interaction of pulsed lasers with plasmonic gold nanoparticles toward light manipulation, heat management, and nanofabrication. *Journal of Photochemistry and Photobiology C: Photochemistry Reviews* **2012**, 13 (1), 28-54.
67. Wuelfing, W. P.; Gross, S. M.; Miles, D. T.; Murray, R. W., Nanometer Gold Clusters Protected by Surface-Bound Monolayers of Thiolated Poly(ethylene glycol) Polymer Electrolyte. *Journal of the American Chemical Society* **1998**, 120 (48), 12696-12697.
68. Beamson, G.; Briggs, D., *High Resolution XPS of Organic Polymers: The Scienta ESCA300 Database*. Wiley: **1992**.
69. Shchukarev, A. V.; Korolkov, D. V., XPS Study of group IA carbonates. *cent.eur.j.chem.* **2004**, 2 (2), 347-362.
70. Lambert, J. B., *Organic structural analysis*. Macmillan: **1976**.
71. Manson, J.; Kumar, D.; Meenan, B. J.; Dixon, D., Polyethylene glycol functionalized gold nanoparticles: the influence of capping density on stability in various media. *Gold Bull* **2011**, 44 (2), 99-105.
72. Laprise-Pelletier, M.; Bouchoucha, M.; Lagueux, J.; Chevallier, P.; Lecomte, R.; Gossuin, Y.; Kleitz, F.; Fortin, M.-A., Metal chelate grafting at the surface of mesoporous silica nanoparticles (MSNs): physico-chemical and biomedical imaging assessment. *J. Mater. Chem. B* **2015**, 3 (5), 748-758.
73. Nakamoto, K., *Infrared and Raman Spectra of Inorganic and Coordination Compounds, Theory and Applications in Inorganic Chemistry*. Wiley: **2008**.
74. Lauffer, R. B., Paramagnetic metal complexes as water proton relaxation agents for NMR imaging: theory and design. *Chem. Rev.* **1987**, 87 (5), 901-927.
75. Murthy, A. K.; Stover, R. J.; Hardin, W. G.; Schramm, R.; Nie, G. D.; Gourisankar, S.; Truskett, T. M.; Sokolov, K. V.; Johnston, K. P., Charged gold nanoparticles with essentially zero serum protein adsorption in undiluted fetal bovine serum. *J. Am. Chem. Soc.* **2013**, 135 (21), 7799-802.
76. Bakan, D. A.; Longino, M. A.; Weichert, J. P.; Counsell, R. E., Physicochemical Characterization of a Synthetic Lipid Emulsion for Hepatocyte-Selective Delivery of Lipophilic Compounds: Application to Polyiodinated Triglycerides as Contrast Agents for Computed Tomography. *Journal of Pharmaceutical Sciences* **1996**, 85 (9), 908-914.
77. Shukla, R.; Bansal, V.; Chaudhary, M.; Basu, A.; Bhone, R. R.; Sastry, M., Biocompatibility of Gold Nanoparticles and Their Endocytotic Fate Inside the Cellular Compartment: A Microscopic Overview. *Langmuir* **2005**, 21 (23), 10644-10654.
78. Khlebtsov, N.; Dykman, L., Biodistribution and toxicity of engineered gold nanoparticles: a review of in vitro and in vivo studies. *Chem. Soc. Rev.* **2011**, 40 (3), 1647-1671.

79. Wegner, G.; Auger, M.; Bélanger, D.; Bénard, P.; Claverie, J.; Fortin, M. A.; Greener, J.; Kleitz, F.; Laroche, G.; Morin, J. F., *Functional Materials: For Energy, Sustainable Development and Biomedical Sciences*. De Gruyter: **2014**.
80. Bushong, S. C., *Magnetic Resonance Imaging*. Mosby: **2003**.
81. McRobbie, D. W.; Moore, E. A.; Graves, M. J.; Prince, M. R., *MRI from Picture to Proton*. Cambridge University Press: **2006**.
82. Kiessling, F.; Pichler, B. J., *Small Animal Imaging: Basics and Practical Guide*. Springer Berlin Heidelberg: **2011**.
83. Merbach, A. S.; Helm, L.; Tóth, É., *The Chemistry of Contrast Agents in Medical Magnetic Resonance Imaging*. Wiley: **2013**.
84. Bushberg, J. T.; Seibert, J. A.; Leidholdt, E. M.; Boone, J. M., *The Essential Physics of Medical Imaging*. Wolters Kluwer Health: **2011**.
85. Villaraza, A. J.; Bumb, A.; Brechbiel, M. W., Macromolecules, dendrimers, and nanomaterials in magnetic resonance imaging: the interplay between size, function, and pharmacokinetics. *Chem Rev* **2010**, 110 (5), 2921-59.
86. Na, H. B.; Song, I. C.; Hyeon, T., Inorganic Nanoparticles for MRI Contrast Agents. *Adv. Mater.* **2009**, 21 (21), 2133-2148.
87. Kachelriess, M., Clinical X-Ray Computed Tomography. In *New Technologies in Radiation Oncology*, Schlegel, W.; Bortfeld, T.; Grosu, A.-L., Eds. Springer Berlin Heidelberg: **2006**; Chapter 7, pp 41-80.
88. Kircher, M. F.; Willmann, J. K., Molecular body imaging: MR imaging, CT, and US. part I. principles. *RJ* **2012**, 263 (3), 633-43.
89. Gore, J. C.; Yankelev, T. E.; Peterson, T. E.; Avison, M. J., Molecular Imaging Without Radiopharmaceuticals? *Journal of Nuclear Medicine* **2009**, 50 (6), 999-1007.
90. Lusic, H.; Grinstaff, M. W., X-ray-computed tomography contrast agents. *Chem Rev* **2013**, 113 (3), 1641-66.
91. Speck, U., Contrast Agents: X-ray Contrast Agents and Molecular Imaging – A Contradiction? In *Molecular Imaging I*, Semmler, W.; Schwaiger, M., Eds. Springer Berlin Heidelberg: **2008**; Chapter 8, pp 167-175.
92. Chauhan, V. P.; Stylianopoulos, T.; Boucher, Y.; Jain, R. K., Delivery of molecular and nanoscale medicine to tumors: transport barriers and strategies. *Annu Rev Chem Biomol Eng* **2011**, 2, 281-98.
93. Moghimi, S. M.; Hunter, A. C.; Andrensen, T. L., Factors controlling nanoparticle pharmacokinetics: an integrated analysis and perspective. *Annu. Rev. Pharmacol. Toxicol.* **2012**, 52 (1), 481-503.
94. Perrault, S. D.; Walkey, C.; Jennings, T.; Fischer, H. C.; Chan, W. C. W., Mediating Tumor Targeting Efficiency of Nanoparticles Through Design. *Nano letters* **2009**, 9 (5), 1909-1915.
95. Bonitatibus, P. J., Jr.; Torres, A. S.; Kandapallil, B.; Lee, B. D.; Goddard, G. D.; Colborn, R. E.; Marino, M. E., Preclinical assessment of a zwitterionic tantalum oxide nanoparticle X-ray contrast agent. *ACS Nano* **2012**, 6 (8), 6650-8.

96. Al Zaki, A.; Joh, D.; Cheng, Z.; De Barros, A. L. B.; Kao, G.; Dorsey, J.; Tsourkas, A., Gold-Loaded Polymeric Micelles for Computed Tomography-Guided Radiation Therapy Treatment and Radiosensitization. *ACS Nano* **2014**, 8 (1), 104-112.
97. Torchilin, V. P.; Frank-Kamenetsky, M. D.; Wolf, G. L., CT visualization of blood pool in rats by using long-circulating, iodine-containing micelles. *Academic Radiology* **1999**, 6 (1), 61-65.
98. Peng, C.; Zheng, L.; Chen, Q.; Shen, M.; Guo, R.; Wang, H.; Cao, X.; Zhang, G.; Shi, X., PEGylated dendrimer-entrapped gold nanoparticles for in vivo blood pool and tumor imaging by computed tomography. *Biomaterials* **2012**, 33 (4), 1107-19.
99. Cormode, D. P.; Roessl, E.; Thran, A.; Skajaa, T.; Gordon, R. E.; Schlomka, J. P.; Fuster, V.; Fisher, E. A.; Mulder, W. J.; Proksa, R.; Fayad, Z. A., Atherosclerotic plaque composition: analysis with multicolor CT and targeted gold nanoparticles. *Radiology* **2010**, 256 (3), 774-82.
100. Allijn, I. E.; Leong, W.; Tang, J.; Gianella, A.; Mieszawska, A. J.; Fay, F.; Ma, G.; Russell, S.; Callo, C. B.; Gordon, R. E.; Korkmaz, E.; Post, J. A.; Zhao, Y.; Gerritsen, H. C.; Thran, A.; Proksa, R.; Daerr, H.; Storm, G.; Fuster, V.; Fisher, E. A.; Fayad, Z. A.; Mulder, W. J. M.; Cormode, D. P., Gold Nanocrystal Labeling Allows Low-Density Lipoprotein Imaging from the Subcellular to Macroscopic Level. *ACS Nano* **2013**, 7 (11), 9761-9770.
101. Galper, M. W.; Saung, M. T.; Fuster, V.; Roessl, E.; Thran, A.; Proksa, R.; Fayad, Z. A.; Cormode, D. P., Effect of computed tomography scanning parameters on gold nanoparticle and iodine contrast. *Invest Radiol* **2012**, 47 (8), 475-81.
102. Jackson, P. A.; Rahman, W. N. W. A.; Wong, C. J.; Ackerly, T.; Geso, M., Potential dependent superiority of gold nanoparticles in comparison to iodinated contrast agents. *European Journal of Radiology* **2010**, 75 (1), 104-109.
103. Hubbell, J. H.; Seltzer, S. M., Tables of X-Ray Mass Attenuation Coefficients and Mass Energy-Absorption Coefficients from 1 keV to 20 MeV for Elements Z = 1 to 92 and 48 Additional Substances of Dosimetric Interest. May 1996 ed.
104. Nebuloni, L.; Kuhn, G. A.; Muller, R., A comparative analysis of water-soluble and blood-pool contrast agents for in vivo vascular imaging with micro-CT. *Acad Radiol* **2013**, 20 (10), 1247-55.
105. Thakor, A. S.; Jokerst, J.; Zavaleta, C.; Massoud, T. F.; Gambhir, S. S., Gold nanoparticles: a revival in precious metal administration to patients. *Nano Lett.* **2011**, 11 (10), 4029-36.
106. Dreaden, E. C.; Alkilany, A. M.; Huang, X.; Murphy, C. J.; El-Sayed, M. A., The golden age: gold nanoparticles for biomedicine. *Chem Soc Rev* **2012**, 41 (7), 2740-79.
107. Hainfeld, J.; Smilowitz, H.; O'Connor, M.; Dilmanian, F.; Slatkin, D.; OConnor, M., Gold nanoparticle imaging and radiotherapy of brain tumors in mice. *Nanomedicine: Nanotechnology, Biology, and Medicine* **2013**, 8 (10), 1601-1609.
108. Butterworth, K. T.; McMahon, S. J.; Currell, F. J.; Prise, K. M., Physical basis and biological mechanisms of gold nanoparticle radiosensitization. *Nanoscale* **2012**, 4 (16), 4830-4838.
109. Cai, Q. Y.; Kim, S. H.; Choi, K. S.; Kim, S. Y.; Byun, S. J.; Kim, K. W.; Park, S. H.; Juhng, S. K.; Yoon, K. H., Colloidal gold nanoparticles as a blood-pool contrast agent for x-ray computed tomography in mice. *Investigative Radiology* **2007**, 42 (12), 797-806.
110. Choi, H. S.; Liu, W.; Liu, F.; Nasr, K.; Misra, P.; Bawendi, M. G.; Frangioni, J. V., Design considerations for tumour-targeted nanoparticles. *Nature Nanotech* **2010**, 5 (1), 42-7.

111. Eck, W.; Nicholson, A. I.; Zentgraf, H.; Semmler, W.; Bartling, S., Anti-CD4-targeted gold nanoparticles induce specific contrast enhancement of peripheral lymph nodes in X-ray computed tomography of live mice. *Nano Lett.* **2010**, *10* (7), 2318-22.
112. Popovtzer, R.; Agrawal, A.; Kotov, N. A.; Popovtzer, A.; Balter, J.; Carey, T. E.; Kopelman, R., Targeted Gold Nanoparticles Enable Molecular CT Imaging of Cancer. *Nano letters* **2008**, *8* (12), 4593-4596.
113. Besner, S. b.; Kabashin, A. V.; Winnik, F. o. M.; Meunier, M., Synthesis of Size-Tunable Polymer-Protected Gold Nanoparticles by Femtosecond Laser-Based Ablation and Seed Growth. *J. Phys. Chem. C* **2009**, *113* (22), 9526-9531.
114. Saha, K.; Agasti, S. S.; Kim, C.; Li, X.; Rotello, V. M., Gold nanoparticles in chemical and biological sensing. *Chem Rev* **2012**, *112* (5), 2739-79.
115. Neouze, M.-A.; Schubert, U., Surface Modification and Functionalization of Metal and Metal Oxide Nanoparticles by Organic Ligands. *Monatsh Chem* **2008**, *139* (3), 183-195.
116. Owens, D. E.; Peppas, N. A., Opsonization, biodistribution, and pharmacokinetics of polymeric nanoparticles. *International Journal of Pharmaceutics* **2006**, *307* (1), 93-102.
117. Arifin, D. R.; Long, C. M.; Gilad, A. A.; Alric, C.; Roux, S.; Tillement, O.; Link, T. W.; Arepally, A.; Bulte, J. W., Trimodal gadolinium-gold microcapsules containing pancreatic islet cells restore normoglycemia in diabetic mice and can be tracked by using US, CT, and positive-contrast MR imaging. *RY* **2011**, *260* (3), 790-8.
118. Narayanan, S.; Sathy, B. N.; Mony, U.; Koyakutty, M.; Nair, S. V.; Menon, D., Biocompatible magnetite/gold nanohybrid contrast agents via green chemistry for MRI and CT bioimaging. *ACS Appl. Mater. Interfaces* **2012**, *4* (1), 251-60.
119. Faucher, L.; Tremblay, M.; Lagueux, J.; Gossuin, Y.; Fortin, M. A., Rapid synthesis of PEGylated ultrasmall gadolinium oxide nanoparticles for cell labeling and tracking with MRI. *ACS Appl. Mater. Interfaces* **2012**, *4* (9), 4506-15.
120. Mutic, S.; Purdy, J. A.; Michalski, J. M.; Perez, C. A., The Simulation Process in the Determination and Definition of the Treatment Volume and Treatment Planning. In *Technical Basis of Radiation Therapy: Practical Clinical Applications*, Levitt, S. H.; Purdy, J. A.; Perez, C. A.; Vijayakumar, S., Eds. Springer Berlin Heidelberg: **2008**; Chapter 6.
121. Krishnan, A. S.; Neves, A. A.; de Backer, M. M.; Hu, D. E.; Davletov, B.; Kettunen, M. I.; Brindle, K. M., Detection of cell death in tumors by using MR imaging and a gadolinium-based targeted contrast agent. *RY* **2008**, *246* (3), 854-62.
122. Morawski, A. M.; Winter, P. M.; Crowder, K. C.; Caruthers, S. D.; Fuhrhop, R. W.; Scott, M. J.; Robertson, J. D.; Abendschein, D. R.; Lanza, G. M.; Wickline, S. A., Targeted nanoparticles for quantitative imaging of sparse molecular epitopes with MRI. *Magn Reson Med* **2004**, *51* (3), 480-6.
123. Neddersen, J.; Chumanov, G.; Cotton, T. M., Laser Ablation of Metals: A New Method for Preparing SERS Active Colloids. *Applied Spectroscopy* **1993**, *47* (12), 1959-1964.
124. Fojtik, A.; Henglein, A., Laser ablation of films and suspended particles in a solvent: formation of cluster and colloid solutions. *Ber. Bunsenges. Phys. Chem.* **1993**, *(97)*, 252–254.
125. Poondi, D.; Singh, J., Synthesis of metastable silver-nickel alloys by a novel laser-liquid-solid interaction technique. *Journal of Materials Science* **2000**, *35* (10), 2467-2476.

126. Yang, G. W., Laser ablation in liquids: Applications in the synthesis of nanocrystals. *Progress in Materials Science* **2007**, 52 (4), 648-698.
127. Scaramuzza, S.; Agnoli, S.; Amendola, V., Metastable alloy nanoparticles, metal-oxide nanocrescents and nanoshells generated by laser ablation in liquid solution: influence of the chemical environment on structure and composition. *Phys. Chem. Chem. Phys.* **2015**, 17 (42), 28076-87.
128. Ibrahimkutty, S.; Wagener, P.; dos Santos Rolo, T.; Karpov, D.; Menzel, A.; Baumbach, T.; Barcikowski, S.; Plech, A., A hierarchical view on material formation during pulsed-laser synthesis of nanoparticles in liquid. *Sci Rep* **2015**, 5, 16313.
129. Itina, T. E., On Nanoparticle Formation by Laser Ablation in Liquids. *J. Phys. Chem. C* **2011**, 115 (12), 5044-5048.
130. Amendola, V.; Meneghetti, M., What controls the composition and the structure of nanomaterials generated by laser ablation in liquid solution? *Physical Chemistry Chemical Physics* **2013**, 15 (9), 3027.
131. Dell'Aglio, M.; Gaudioso, R.; De Pascale, O.; De Giacomo, A., Mechanisms and processes of pulsed laser ablation in liquids during nanoparticle production. *Applied Surface Science* **2015**, 348, 4-9.
132. Tarasenko, N., Pulsed laser ablation synthesis and modification of composite nanoparticles in liquids. In *Laser Ablation in Liquids: Principles and Applications in the Preparation of Nanomaterials*, Yang, G., Ed. Pan Stanford: **2012**; Chapter 14, pp 709-768.
133. Woehrle, G. H.; Brown, L. O.; Hutchison, J. E., Thiol-functionalized, 1.5-nm gold nanoparticles through ligand exchange reactions: scope and mechanism of ligand exchange. *J. Am. Chem. Soc.* **2005**, 127 (7), 2172-83.
134. Nachev, P.; van 'T Zand, D. D.; Coger, V.; Wagener, P.; Reimers, K.; Vogt, P. M.; Barcikowski, S.; Pich, A., Synthesis of hybrid microgels by coupling of laser ablation and polymerization in aqueous medium. *J. Laser Appl.* **2012**, 24 (4), 042012.
135. Leena, P.; Jouni, H.; Timo, L., Drug Nanocrystals and Nanosuspensions in Medicine. In *Handbook of Nanobiomedical Research*, WORLD SCIENTIFIC: **2013**, pp 169-197.
136. Smith, A. M.; Marbella, L. E.; Johnston, K. A.; Hartmann, M. J.; Crawford, S. E.; Kozycz, L. M.; Seferos, D. S.; Millstone, J. E., Quantitative Analysis of Thiolated Ligand Exchange on Gold Nanoparticles Monitored by ^1H NMR Spectroscopy. *Anal. Chem.* **2015**, 87 (5), 2771-2778.
137. Fauconnier, N.; Pons, J. N.; Roger, J.; Bee, A., Thiolation of Maghemite Nanoparticles by Dimercaptosuccinic Acid. *Journal of Colloid and Interface Science* **1997**, 194 (2), 427-433.
138. Letourneau, M.; Tremblay, M.; Faucher, L.; Rojas, D.; Chevallier, P.; Gossuin, Y.; Lagueux, J.; Fortin, M. A., MnO-labeled cells: positive contrast enhancement in MRI. *J Phys Chem B* **2012**, 116 (44), 13228-38.
139. Verma, H. R., Neutron Activation Analysis. In *Atomic and Nuclear Analytical Methods: XRF, Mössbauer, XPS, NAA and Ion-Beam Spectroscopic Techniques*, Springer Berlin Heidelberg: **2007**; Chapter 6.
140. Skoog, D. A.; Holler, F. J.; Nieman, T. A., *Principes d'analyse instrumentale*. De Boeck: **2003**.

141. Deryugina, E. I.; Quigley, J. P., Chick embryo chorioallantoic membrane model systems to study and visualize human tumor cell metastasis. *Histochem Cell Biol* **2008**, 130 (6), 1119-30.
142. Lokman, N. A.; Elder, A. S.; Ricciardelli, C.; Oehler, M. K., Chick chorioallantoic membrane (CAM) assay as an in vivo model to study the effect of newly identified molecules on ovarian cancer invasion and metastasis. *IJMS* **2012**, 13 (8), 9959-70.
143. AshaRani, P. V.; Low Kah Mun, G.; Hande, M. P.; Valiyaveettil, S., Cytotoxicity and genotoxicity of silver nanoparticles in human cells. *ACS Nano* **2009**, 3 (2), 279-90.
144. King, M. A., Detection of dead cells and measurement of cell killing by flow cytometry. *J Immunol Methods* **2000**, 243 (1-2), 155-66.
145. Connolly, M.; Perez, Y.; Mann, E.; Herradon, B.; Fernandez-Cruz, M. L.; Navas, J. M., Peptide-biphenyl hybrid-capped AuNPs: stability and biocompatibility under cell culture conditions. *Nanoscale Res Lett* **2013**, 8 (1), 315.
146. Schick, I.; Lorenz, S.; Gehrig, D.; Schilmann, A. M.; Bauer, H.; Panthofer, M.; Fischer, K.; Strand, D.; Laquai, F.; Tremel, W., Multifunctional two-photon active silica-coated Au@MnO Janus particles for selective dual functionalization and imaging. *J. Am. Chem. Soc.* **2014**, 136 (6), 2473-83.
147. Ardizzone, S.; Bianchi, C. L.; Tirelli, D., Mn₃O₄ and g-MnOOH powders, preparation, phase composition and XPS characterization. *Colloids and Surfaces A* **1998**, 134, 305-312.
148. Biesinger, M. C.; Payne, B. P.; Grosvenor, A. P.; Lau, L. W. M.; Gerson, A. R.; Smart, R. S. C., Resolving surface chemical states in XPS analysis of first row transition metals, oxides and hydroxides: Cr, Mn, Fe, Co and Ni. *Applied Surface Science* **2011**, 257 (7), 2717-2730.
149. Guillet-Nicolas, R.; Laprise-Pelletier, M.; Nair, M. M.; Chevallier, P.; Lagueux, J.; Gossuin, Y.; Laurent, S.; Kleitz, F.; Fortin, M. A., Manganese-impregnated mesoporous silica nanoparticles for signal enhancement in MRI cell labelling studies. *Nanoscale* **2013**, 5 (23), 11499-511.
150. Nanopartz, I. Part #A11, Accurate Spherical Gold Nanoparticles, OD=1, 0.05 mg/mL. http://www.nanopartz.com/bare_spherical_gold_nanoparticles.asp.
151. Kim, D.; Park, S.; Lee, J. H.; Jeong, Y. Y.; Jon, S., Antibiofouling polymer-coated gold nanoparticles as a contrast agent for in vivo X-ray computed tomography imaging. *J. Am. Chem. Soc.* **2007**, 129 (24), 7661-5.
152. Ghosh Chaudhuri, R.; Paria, S., Core/shell nanoparticles: classes, properties, synthesis mechanisms, characterization, and applications. *Chem Rev* **2012**, 112 (4), 2373-433.
153. Toshima, N.; Yonezawa, T., Bimetallic nanoparticles—novel materials for chemical and physical applications. *New J. Chem.* **1998**, 22 (11), 1179-1201.
154. Zanella, R.; Giorgio, S.; Henry, C. R.; Louis, C., Alternative Methods for the Preparation of Gold Nanoparticles Supported on TiO₂. *J. Phys. Chem. B* **2002**, 106 (31), 7634-7642.
155. Liu, X.; Liu, M. H.; Luo, Y. C.; Mou, C. Y.; Lin, S. D.; Cheng, H.; Chen, J. M.; Lee, J. F.; Lin, T. S., Strong metal-support interactions between gold nanoparticles and ZnO nanorods in CO oxidation. *J. Am. Chem. Soc.* **2012**, 134 (24), 10251-8.
156. Suzuki, K.; Yamaguchi, T.; Matsushita, K.; Itsuka, C.; Miura, J.; Akaogi, T.; Ishida, H., Aerobic Oxidative Esterification of Aldehydes with Alcohols by Gold–Nickel Oxide Nanoparticle Catalysts with a Core–Shell Structure. *ACS Catal.* **2013**, 3 (8), 1845-1849.

157. Soule, J. F.; Miyamura, H.; Kobayashi, S., Powerful amide synthesis from alcohols and amines under aerobic conditions catalyzed by gold or gold/iron, -nickel or -cobalt nanoparticles. *J. Am. Chem. Soc.* **2011**, 133 (46), 18550-3.
158. Kim, D.; Resasco, J.; Yu, Y.; Asiri, A. M.; Yang, P., Synergistic geometric and electronic effects for electrochemical reduction of carbon dioxide using gold-copper bimetallic nanoparticles. *Nature Communications* **2014**, 5, 4948.
159. Djoumessi, D.; Laprise-Pelletier, M.; Chevallier, P.; Lagueux, J.; Côté, M. F.; Fortin, M. A., Rapid, one-pot procedure to synthesise¹⁰³Pd:Pd@Au nanoparticles en route for radiosensitisation and radiotherapeutic applications. *J. Mater. Chem. B* **2015**, 3 (10), 2192-2205.
160. Lin, X.-D.; Uzayisenga, V.; Li, J.-F.; Fang, P.-P.; Wu, D.-Y.; Ren, B.; Tian, Z.-Q., Synthesis of ultrathin and compact Au@MnO₂ nanoparticles for shell-isolated nanoparticle-enhanced Raman spectroscopy (SHINERS). *J. Raman Spectrosc.* **2012**, 43 (1), 40-45.
161. Longo, A.; Liotta, L. F.; Carlo, G. D.; Giannici, F.; Venezia, A. M.; Martorana, A., Structure and the Metal Support Interaction of the Au/Mn Oxide Catalysts. *Chem. Mater.* **2010**, 22 (13), 3952-3960.
162. Wang, L.; Huang, X.; Liu, Q.; Liu, Y.; Cao, Y.; He, H.; Fan, K.; Zhuang, J., Gold nanoparticles deposited on manganese(III) oxide as novel efficient catalyst for low temperature CO oxidation. *Journal of Catalysis* **2008**, 259 (1), 66-74.
163. Lee, S.-J.; Gavrilidis, A.; Pankhurst, Q. A.; Kyek, A.; Wagner, F. E.; Wong, P. C. L.; Yeung, K. L., Effect of Drying Conditions of Au-Mn Co-Precipitates for Low-Temperature CO Oxidation. *Journal of Catalysis* **2001**, 200 (2), 298-308.
164. Wang, L. C.; Liu, Y. M.; Chen, M.; Cao, Y., MnO₂ Nanorod Supported Gold Nanoparticles with Enhanced Activity for Solvent-free Aerobic Alcohol Oxidation - The Journal of Physical Chemistry C (ACS Publications). *J Phys Chem C* **2008**, 112 (17), 6981-6987.
165. Sinha, A. K.; Suzuki, K.; Takahara, M.; Azuma, H.; Nonaka, T.; Fukumoto, K., Mesostructured manganese oxide/gold nanoparticle composites for extensive air purification. *Angew. Chem.* **2007**, 46 (16), 2891-4.
166. Padayachee, D.; Golovko, V.; Marshall, A. T., The effect of MnO₂ loading on the glycerol electrooxidation activity of Au/MnO₂/C catalysts. *Electrochimica Acta* **2013**, 98, 208-217.
167. Schladt, T. D.; Shukoor, M. I.; Schneider, K.; Tahir, M. N.; Natalio, F.; Ament, I.; Becker, J.; Jochum, F. D.; Weber, S.; Kohler, O.; Theato, P.; Schreiber, L. M.; Sonnichsen, C.; Schroder, H. C.; Muller, W. E.; Tremel, W., Au@MnO nanoflowers: hybrid nanocomposites for selective dual functionalization and imaging. *Angew. Chem.* **2010**, 49 (23), 3976-80.
168. Huang, C. C.; Khu, N. H.; Yeh, C. S., The characteristics of sub 10 nm manganese oxide T1 contrast agents of different nanostructured morphologies. *Biomaterials* **2010**, 31 (14), 4073-8.
169. Taylor, U.; Rehbock, C.; Streich, C.; Rath, D.; Barcikowski, S., Rational design of gold nanoparticle toxicology assays: a question of exposure scenario, dose and experimental setup. *Nanomedicine (Lond)* **2014**, 9 (13), 1971-89.
170. Li, D.; Wang, C.; Tripkovic, D.; Sun, S.; Markovic, N. M.; Stamenkovic, V. R., Surfactant Removal for Colloidal Nanoparticles from Solution Synthesis: The Effect on Catalytic Performance. *ACS Catal.* **2012**, 2 (7), 1358-1362.

171. Luo, N.; Tian, X.; Yang, C.; Xiao, J.; Hu, W.; Chen, D.; Li, L., Ligand-free gadolinium oxide for in vivo T1-weighted magnetic resonance imaging. *Phys. Chem. Chem. Phys.* **2013**, *15* (29), 12235-40.
172. Lv, Q.; Wang, S.; Sun, H.; Luo, J.; Xiao, J.; Xiao, F.; Wang, S., Solid-State Thin-Film Supercapacitors with Ultrafast Charge/Discharge Based on N-Doped-Carbon-Tubes/Au-Nanoparticles-Doped-MnO₂ Nanocomposites. *Nano Lett.* **2016**, *16* (1), 40-7.
173. Asahi, T.; Mafuné, F.; Rehbock, C.; Barcikowski, S., Strategies to harvest the unique properties of laser-generated nanomaterials in biomedical and energy applications. *Applied Surface Science* **2015**, *348*, 1-3.
174. Oko, D. N.; Garbarino, S.; Zhang, J.; Xu, Z.; Chaker, M.; Ma, D.; Guay, D.; Tavares, A. C., Dopamine and ascorbic acid electro-oxidation on Au, AuPt and Pt nanoparticles prepared by pulse laser ablation in water. *Electrochimica Acta* **2015**, *159*, 174-183.
175. Liu, J.; Tian, X.; Luo, N.; Yang, C.; Xiao, J.; Shao, Y.; Chen, X.; Yang, G.; Chen, D.; Li, L., Sub-10 nm monoclinic Gd₂O₃:Eu³⁺ nanoparticles as dual-modal nanoprobes for magnetic resonance and fluorescence imaging. *Langmuir* **2014**, *30* (43), 13005-13.
176. Chen, F.; Chen, M.; Yang, C.; Liu, J.; Luo, N.; Yang, G.; Chen, D.; Li, L., Terbium-doped gadolinium oxide nanoparticles prepared by laser ablation in liquid for use as a fluorescence and magnetic resonance imaging dual-modal contrast agent. *Phys. Chem. Chem. Phys.* **2015**, *17* (2), 1189-96.
177. Lau, M.; Barcikowski, S., Quantification of mass-specific laser energy input converted into particle properties during picosecond pulsed laser fragmentation of zinc oxide and boron carbide in liquids. *Applied Surface Science* **2015**, *348*, 22-29.
178. Ott, H., *Zeitschrift fuer Kristallographie, Kristallgeometrie, Kristallphysik, Kristallchemie* **1977**, *63*, 222-230.
179. Geller, S., *Acta Crystallographica Section B* . **1971**, *27*, 821-828.
180. Wyckoff, R. W. G., *Crystal Structures*. Wiley: New York, **1963**; Vol. 1.
181. Ankudinov, A. L.; Ravel, B.; Rehr, J. J.; Conradson, S. D., *Phys. Rev. B: Condens. Matter Mater. Phys.* **1998** (58), 7565-7576.
182. Newville, M.; Boyanov, B. I.; Sayers, D. E., *J. Synchrotron Radiat.* **1999**, *6*, 264-265.
183. Jennings, T.; Strouse, G., Past, Present, and Future of Gold Nanoparticles. In *Bio-applications of Nanoparticles*, Chan, W. C. W., Ed. Springer New York: **2007**, pp 34-47.
184. Yu, R.; Machavariani, V. S.; Voronel, A.; Garber, S.; Rubshtain, A.; Frenkel, A. I.; Stern, E. A., Strain energy density in the x-ray powder diffraction from mixed crystals and alloys. *Journal of Physics: Condensed Matter* **2000**, *12* (37), 8081.
185. Huang, Z.; Thomson, P.; Di, S., Lattice contractions of a nanoparticle due to the surface tension: A model of elasticity. *Journal of Physics and Chemistry of Solids* **2007**, *68* (4), 530-535.
186. Tsuji, T.; Iryo, K.; Watanabe, N.; Tsuji, M., Preparation of silver nanoparticles by laser ablation in solution: influence of laser wavelength on particle size. *Applied Surface Science* **2002**, *202*, 80-85.
187. Inasawa, S.; Sugiyama, M.; Yamaguchi, Y., Bimodal Size Distribution of Gold Nanoparticles under Picosecond Laser Pulses. *J Phys Chem B* **2005**, *109* (19), 9404-10.

188. Pyatenko, A.; Wang, H.; Koshizaki, N.; Tsuji, T., Mechanism of pulse laser interaction with colloidal nanoparticles. *Laser & Photonics Reviews* **2013**, 7 (4), 596-604.
189. Jimenez, E.; Abderrafi, K.; Abargues, R.; Valdes, J. L.; Martinez-Pastor, J. P., Laser-ablation-induced synthesis of SiO₂-capped noble metal nanoparticles in a single step. *Langmuir* **2010**, 26 (10), 7458-63.
190. Compagnini, G.; Messina, E.; Puglisi, O.; Cataliotti, R. S.; Nicolosi, V., Spectroscopic evidence of a core-shell structure in the earlier formation stages of Au-Ag nanoparticles by pulsed laser ablation in water. *Chem Phys Lett* **2008**, 457 (4-6), 386-390.
191. Bajaj, G.; Soni, R. K., Synthesis of composite gold/tin-oxide nanoparticles by nano-soldering. *J Nanopart Res* **2010**, 12 (7), 2597-2603.
192. Kawaguchi, K.; Jaworski, J.; Ishikawa, Y.; Sasaki, T.; Koshizaki, N., Preparation of gold/iron-oxide composite nanoparticles by a unique laser process in water. *J Magn Magn Mater* **2007**, 310 (2), 2369-2371.
193. Mafune, F.; Kohno, J. Y.; Takeda, Y.; Kondow, T., Nanoscale soldering of metal nanoparticles for construction of higher-order structures. *J Am. Chem. Soc.* **2003**, 125 (7), 1686-7.
194. Jurij, J.; Ana, M.-M.; Venkata Sai Kiran, C.; Lorenz, K.; Philipp, W.; Stephan, B., Stoichiometry of alloy nanoparticles from laser ablation of PtIr in acetone and their electrophoretic deposition on PtIr electrodes. *Nanotechnology* **2011**, 22 (14), 145601.
195. Menéndez-Manjón, A.; Schwenke, A.; Steinke, T.; Meyer, M.; Giese, U.; Wagener, P.; Barcikowski, S., Ligand-free gold–silver nanoparticle alloy polymer composites generated by picosecond laser ablation in liquid monomer. *Applied Physics A* **2012**, 110 (2), 343-350.
196. Thakor, A. S.; Jokerst, J.; Zavaleta, C.; Massoud, T. F.; Gambhir, S. S., Gold Nanoparticles: A Revival in Precious Metal Administration to Patients. *Nano Lett.* **2011**, 11 (10), 4029-4036.
197. Clark, D. P.; Ghaghada, K.; Moding, E. J.; Kirsch, D. G.; Badea, C. T., In vivo characterization of tumor vasculature using iodine and gold nanoparticles and dual energy micro-CT. *Phys. Med. Biol.* **2013**, 58 (6), 1683-704.
198. Schürmann, C.; Gremse, F.; Jo, H.; Kiessling, F.; Brandes, R. P., Micro-CT Technique Is Well Suited for Documentation of Remodeling Processes in Murine Carotid Arteries. *PLoS ONE* **2015**, 10 (6), e0130374.
199. Magnoni, M.; Ammirati, E.; Camici, P. G., Non-invasive molecular imaging of vulnerable atherosclerotic plaques. *Journal of Cardiology* **2015**, 65 (4), 261-9.
200. Massoud, T. F.; Gambhir, S. S., Molecular imaging in living subjects: seeing fundamental biological processes in a new light. *Genes & Development* **2003**, 17 (5), 545-80.
201. Lee, C. H.; Dershaw, D. D.; Kopans, D.; Evans, P.; Monsees, B.; Monticciolo, D.; Brenner, R. J.; Bassett, L.; Berg, W.; Feig, S.; Hendrick, E.; Mendelson, E.; D'Orsi, C.; Sickles, E.; Burhenne, L. W., Breast Cancer Screening With Imaging: Recommendations From the Society of Breast Imaging and the ACR on the Use of Mammography, Breast MRI, Breast Ultrasound, and Other Technologies for the Detection of Clinically Occult Breast Cancer. *Journal of the American College of Radiology* **2010**, 7 (1), 18-27.
202. Heidenreich, A.; Bellmunt, J.; Bolla, M.; Joniau, S.; Mason, M.; Matveev, V.; Mottet, N.; Schmid, H. P.; van der Kwast, T.; Wiegel, T.; Zattoni, F.; European Association of, U., EAU

guidelines on prostate cancer. Part 1: screening, diagnosis, and treatment of clinically localised disease. *Eur Urol* **2011**, *59* (1), 61-71.

203. Patel, V.; Papineni, R. V. L.; Gupta, S.; Stoyanova, R.; Ahmed, M. M., A Realistic Utilization of Nanotechnology in Molecular Imaging and Targeted Radiotherapy of Solid Tumors. *Radiation Research* **2012**, *177* (4), 483-495.
204. Chen, H.; Paholak, H.; Ito, M.; Sansanaphongpricha, K.; Qian, W.; Che, Y.; Sun, D., 'Living' PEGylation on gold nanoparticles to optimize cancer cell uptake by controlling targeting ligand and charge densities. *Nanotechnology* **2013**, *24* (35), 355101.
205. Naccache, R.; Chevallier, P.; Lagueux, J.; Gossuin, Y.; Laurent, S.; Vander Elst, L.; Chilian, C.; Capobianco, J. A.; Fortin, M. A., High relaxivities and strong vascular signal enhancement for NaGdF4 nanoparticles designed for dual MR/optical imaging. *Advanced Healthcare Materials* **2013**, *2* (11), 1478-88.
206. Cormode, D. P.; Skajaa, T.; van Schooneveld, M. M.; Koole, R.; Jarzyna, P.; Lobatto, M. E.; Calcagno, C.; Barazza, A.; Gordon, R. E.; Zanzonico, P.; Fisher, E. A.; Fayad, Z. A.; Mulder, W. J. M., Nanocrystal Core High-Density Lipoproteins: A Multimodality Contrast Agent Platform. *Nano letters* **2008**, *8* (11), 3715-3723.
207. Ghann, W. E.; Aras, O.; Fleiter, T.; Daniel, M. C., Syntheses and characterization of lisinopril-coated gold nanoparticles as highly stable targeted CT contrast agents in cardiovascular diseases. *Langmuir* **2012**, *28* (28), 10398-408.
208. Monopoli, M. P.; Aberg, C.; Salvati, A.; Dawson, K. A., Biomolecular coronas provide the biological identity of nanosized materials. *Nature Nanotech* **2012**, *7* (12), 779-86.
209. Haiss, W.; Thanh, N. T. K.; Aveyard, J.; Fernig, D. G., Determination of Size and Concentration of Gold Nanoparticles from UV-Vis Spectra. *Anal. Chem.* **2007**, *79* (11), 4215-4221.
210. Zhang, G.; Yang, Z.; Lu, W.; Zhang, R.; Huang, Q.; Tian, M.; Li, L.; Liang, D.; Li, C., Influence of anchoring ligands and particle size on the colloidal stability and in vivo biodistribution of polyethylene glycol-coated gold nanoparticles in tumor-xenografted mice. *Biomaterials* **2009**, *30* (10), 1928-36.
211. Cole, L. E.; Vargo-Gogola, T.; Roeder, R. K., Contrast-enhanced X-ray detection of breast microcalcifications in a murine model using targeted gold nanoparticles. *ACS Nano* **2014**, *8* (7), 7486-96.
212. Kim, D.; Jeong, Y. Y.; Jon, S., A drug-loaded aptamer-gold nanoparticle bioconjugate for combined CT imaging and therapy of prostate cancer. *ACS Nano* **2010**, *4* (7), 3689-96.
213. Tsai, D. H.; DelRio, F. W.; MacCuspie, R. I.; Cho, T. J.; Zachariah, M. R.; Hackley, V. A., Competitive adsorption of thiolated polyethylene glycol and mercaptopropionic acid on gold nanoparticles measured by physical characterization methods. *Langmuir* **2010**, *26* (12), 10325-33.
214. Larson-Smith, K.; Pozzo, D. C., Competitive adsorption of thiolated poly(ethylene glycol) and alkane-thiols on gold nanoparticles and its effect on cluster formation. *Langmuir* **2012**, *28* (37), 13157-65.
215. Choi, C. H. J.; Zuckerman, J. E.; Webster, P.; Davis, M. E., Targeting kidney mesangium by nanoparticles of defined size. *Proceedings of the National Academy of Sciences* **2011**, *108* (16), 6656-6661.

216. Park, M.; Lee, N.; Choi, S. H.; An, K.; Yu, S.-H.; Kim, J. H.; Kwon, S.-H.; Kim, D.; Kim, H.; Baek, S.-I.; Ahn, T.-Y.; Park, O. K.; Son, J. S.; Sung, Y.-E.; Kim, Y.-W.; Wang, Z.; Pinna, N.; Hyeon, T., Large-Scale Synthesis of Ultrathin Manganese Oxide Nanoplates and Their Applications to T1 MRI Contrast Agents. *Chem. Mater.* **2011**, 23 (14), 3318-3324.
217. Baek, M. J.; Park, J. Y.; Xu, W.; Kattel, K.; Kim, H. G.; Lee, E. J.; Patel, A. K.; Lee, J. J.; Chang, Y.; Kim, T. J.; Bae, J. E.; Chae, K. S.; Lee, G. H., Water-soluble MnO nanocolloid for a molecular T1 MR imaging: a facile one-pot synthesis, in vivo T1 MR images, and account for relaxivities. *ACS Appl. Mater. Interfaces* **2010**, 2 (10), 2949-55.

ANNEXE

INTERNSHIP PERFORMED DURING THE THESIS

Technical Chemistry I, University of Duisburg-Essen, Prof. Barcikowski's research group,
Germany

February – May 2014

SCIENTIFIC PUBLICATIONS OBTAINED DURING THE THESIS

2) Simão T., Chevrier D. M., Jakobi J., Korinek A., Goupil G., Lau M., Garbarino S., Zhang P., Barcikowski S., Fortin M-A., Guay D. Gold-Manganese Oxide Nanoparticles produced by Pulsed Laser Ablation in Water. *Submitted to the Journal of Physical Chemistry C*

1) Simão T., Chevallier P., Lagueux J., Côté M-F., Rehbock C., Barcikowski S., Fortin M-A., Guay D. Laser-synthesized Ligand-Free Au Nanoparticles for Contrast Agent Applications in Computed Tomography and Magnetic Resonance Imaging. *Submitted to the Journal of Materials Chemistry C*

CONFERENCE PRESENTATIONS

Oral presentations

2) Simão T., Chevallier P., Barcikowski S., Fortin M-A., Guay D., "Ligand-Free Au Nanoparticles Functionalized with Mn Chelates for Computed Tomography and Magnetic Resonance Imaging", MRS Spring Meeting & Exhibit, San Francisco, California, USA, 5 - 10 April 2015

1) Simão T., Chevallier P., Barcikowski S., Fortin M-A., Guay D., "Ligand-Free Au Nanoparticles Functionalized with Mn Chelates for Computed Tomography and Magnetic Resonance Imaging", Colloque annuel du CQMF 2014, Shawinigan, QC, Canada, 6 - 7 November 2014

Poster presentations

- 4) Simão T., Chevallier P., Barcikowski S., Fortin M-A., Guay D., "Au-Mn Nanoparticles for Dual Computed Tomography and Magnetic Resonance Imaging", Colloque étudiant du CERMA 2014, Quebec, QC, Canada, 28 October 2014
- 3) Simão T., Chevallier P., Barcikowski S., Fortin M-A., Guay D., "Ligand-Free Au Nanoparticles Functionalized with Mn-Chelates for CT and MRI", 3rd Mobilization Forum of MEDTEQ, Quebec, QC, Canada, 21 October 2014
- 2) Simão T., Chevallier P., Barcikowski S., Fortin M-A., Guay D., "*Au-Mn Nanoparticles for Dual Computed Tomography and Magnetic Resonance Imaging*", Imaginez l'Imagerie – International Symposium, Sherbrook, QC, Canada, 25 – 26 September 2014
- 1) Simão T., Goupil G., Garbarino S., Fortin M-A., Guay D., "*Properties of Au-Mn Nanoparticles Synthesized by Pulsed Laser Ablation in Liquids*", MRS Fall Meeting & Exhibit, Boston, Massachusetts, USA, 1 - 6 December 2013